

WEO 2021

2nd Workshop on Engineering Optimization

7-8 October 2021

Warsaw, Poland

- supported by
- Visegrad Fund
- •



Book of Abstracts

Editors:

Bartłomiej Błachowski

Piotr Tazowski

INSTITUTE OF FUNDAMENTAL TECHNOLOGICAL RESEARCH
POLISH ACADEMY OF SCIENCES

2nd Workshop on Engineering Optimization – WEO 2021

Book of Abstracts

Editors:

Bartłomiej Błachowski

Piotr Tazowski

WARSZAWA 2021

© Copyright by Institute of Fundamental Technological Research, Polish Academy of Sciences
Warszawa 2021

ISBN 978-83-65550-23-1

The selection and presentation of material and the opinion expressed in this publication are the sole responsibility of the authors concerned.

No responsibility is assumed by the Publishers for any injury and/or damage to persons or property as a matter of products liability, negligence or otherwise, or from any use or operation of any method, products, instructions or ideas contained in the material herein.



Institute of Fundamental Technological Research PAN

02-106 Warszawa, ul. Pawińskiego 5B

www.ippt.pan.pl

Table of contents

Table of contents	6
Preface	8
Keynote speakers	9
Session 1: Monitoring and Condition assessment of engineering structures	12
P. Konecny, et al. - Experimental Investigation and Modelling of Concrete Exposed to Chlorides	13
M. Moravcik - Assessment of prestressing effect in existing concrete bridges	15
P. Olaszek - Innovative methods of measuring bridge displacements under static and dynamic loads	17
Session 2: Computer vision and its application in civil engineering	22
M. Stoński-Deep convolutional neural networks for image-based detection of concrete surface cracks	23
M. Źarski et al. - Advances in applicable deep-learning based defect detection	25
B. Wójcik et al.-Extracting crack characteristics from RGB-D images	29
L. Pospíšil et al. - Causality based image classification	31
Session 3: Dynamic system identification using Bayesian approach	36
Jia-Hua Yang - Bayesian Identification of Engineering Dynamic Systems Based on Vector Autoregressive Model	37
M. Ostrowski, et al. - Bayesian approach for efficient identification of highly uncertain structural parameters	39
Session 4: Systems for autonomous inspections of civil infrastructure	44
Á. Barsi, J. M. Lógó - Autonomous platforms in civil engineering practice	45
J. M. Lógó, Á. Barsi - Paradigm change of mapping in the advent of driverless transportation	46
J. Szklarski - Coverage Path Planning for a Fleet of Industrial Cleaning Robots	52
E. Zawidzka et al. - Arm-Z: a hyper-redundant modular inspection manipulator (for extreme environments)	53
Session 5: Recent advances in structural design and topology optimization	58
M. Bruggi, et al.- Simultaneous design of topology and printing direction of structural elements for Wire-and-Arc Additive Manufacturing (WAAM)	59
M. Movahedi Rad et al. - Optimal Elastic-Plastic Analysis of Reinforced Concrete Structures with Limited Residual Strain Energy Capacity	64

<u>H. Ismail, et al. - Multiscale Optimal Design of Grid Systems for High-rise Buildings</u>	66
<u>P. Zabojszcza et al. - Optimization of A Steel Structure Taking Into Account The Randomness Of Design Parameters</u>	70
<u>G. Dzierżanowski - Topology optimization of large-scale arch systems</u>	75
Session 6:Applications of optimization in various engineering areas	80
<u>D. Pelevin et al. - Mitigation of urban substation magnetic field by active loop</u>	81
<u>M.U. Khodjabekov - Stability of Steady State Motion of Rod Protected From Vibration</u>	83
<u>B. A. Lógó , B. Vásárhelyi - Charpy impact test to sedimentary rocks</u>	89
<u>List of participants</u>	97

Preface

This e-book contains abstracts of papers accepted for presentation at the 2nd Workshop on Engineering Optimization (WEO 2021). The workshop was held in Warsaw, Poland, on October 7-8, 2021. More details can be found on the conference website: <http://v4shm.ippt.pan.pl/events.html>

The Workshops on Engineering Optimization are a series of biennial international workshops, which have been organized by the Institute of Fundamental Technological Research of the Polish Academy of Sciences (IPPT PAN) since 2019. The purpose of this multidisciplinary event, devoted to recent advances in optimization applied to engineering problems, is to bring together scientists, engineers and PhD students working in structural, mechanical and electrical engineering as well as mathematicians and computer scientists. The workshop is also a good opportunity to exchange experiences in the field of widely understood optimization as well as to discuss the aspects of its computer implementation.

Due to the COVID-19 pandemic, this year's edition of the workshop was organized in a hybrid form and was dedicated to the exchange of experiences in the field of computer vision-based civil infrastructure inspection and monitoring with emphasis on automatic crack detection in concrete structures. The workshop hosted 6 invited lectures and 6 thematic sessions. 21 presentations by authors from 7 European and non-European countries (50% of them from outside Poland) were delivered.

Engineering optimization is in itself an area of active research, that also provides the foundation for numerous industrial applications that necessitate sophisticated computational models and methods. Naturally, the WEO workshop series encompasses these research directions as well. Industrial use of engineering optimization is clearly increasing and we foresee that this trend will continue in the future.

Bartłomiej Błachowski and Piotr Tazowski
The Organizing Committee
of the 2nd Workshop on Engineering Optimization (WEO 2021)

Keynote speakers

Árpád Barsi, *Budapest University of Technology and Economics, Hungary.*

Árpád Barsi obtained his BSc diploma in surveying engineering from the University of Forestry and Timber Industry (Székesfehérvár) and his MSc diploma in civil engineering from the Technical University Budapest (BME) in 1990 and 1994, respectively. He received a Ph.D. degree in Geodesy and Geoinformatics from BME in 1998. Dr. Barsi wrote his habilitation thesis in 2004 about "Application of neural networks in image analysis and Geoinformatics", then received a full professorship in 2011. He has been the head of the Department of Photogrammetry and Geoinformatics since 2004. His research interest covers high-resolution mapping, photogrammetry, computer vision, GIS, autonomous vehicles, and artificial intelligence. He organized several international workshops (e.g., ISPRS GIS-workshop 1995 Budapest, UNESCO GIS-workshop 1999 Zagreb, EuroSDR workshop 2004 Budapest). Professor Barsi led the Hungarian research group in several European Union-funded transportation research projects (FP6 "Safespot"; FP7 "Safetrip"; INTAS). Prof. Barsi serves as editor in 3 journals and reviewer in 8 journals, chair in 3 scientific committees, and member in 5 societies.

Matteo Bruggi, *Politecnico di Milano, Italy.*

Matteo Bruggi, PhD has been associate professor of Solid and Structural Mechanics at Politecnico di Milano, Italy, since 2018. He is currently a member of the group "Structural Design, Diagnostics and Rehabilitation" at the Department of Civil and Environmental Engineering. Author of more than 150 scientific communications, among which about 50 published in Scopus-indexed international journals, he is mainly involved in structural analysis and optimization, with special interest in topology optimization. In 2015, he received the "AIMETA Junior Prize" awarded from the Italian Association of Theoretical and Applied Mechanics. Since 2017, he has been a member of the Editorial Board of "Advances in Engineering Software" and since 2019 of "Computers & Structures". In 2021, he served as co-chairman of the Thematic Session on "Optimization for Solids and Fluids" at the 25th International Congress of Theoretical and Applied Mechanics (ICTAM 2020+1).

Petr Konečný, *VŠB Technical University of Ostrava, Czech Republic*

Petr Konečný is an associate professor at the Department of Structural Mechanics at VŠB – Technical University of Ostrava with almost 20 years of experience in the numerical and experimental evaluation of concrete durability, modeling of chloride ingress, probabilistic reliability analysis, etc. He is an editorial board member and reviewer of the journal *Periodica Polytechnica*; reviewer for the *Construction and Building Materials*, *Structural Concrete*, etc. Author or Co-author of 10 articles journals in WoS. He was awarded by with Fulbright scholarship for the research related to Ground Source Heat Pumps at Oklahoma State University; USA; he was a principal investigator of the research on the probabilistic modeling of the durability of RC structures by the Czech Science Foundation. Currently, he is at the internship at University of Warmia and Mazury in Olsztyn conducting a research in the field of construction of lunar habitats. He was a visiting professor at the Silesian University of Technology in Gliwice.

Martin Moravcik, PhD. *University of Zilina, Civil Engineering Faculty Head of Concrete Structures and Bridges Department*

Professor Martin Moravcik is a recognized expert in the design and evaluation of concrete structures and bridges at Civil Engineering Faculty, University of Zilina. He has been focusing mainly on design, computer modeling, diagnostics and reliability assessment of the concrete structures and bridges since 1993. For example he led the team that designed several types of new standardized prestressed precast concrete girders for the road bridge structures, such as MDP 38m and 42m - for the company Váhostav-Sk, Inc. and I and T- shape prestressed girders for the company Prefa Sučany, Inc. He is an author of more than 150 articles in scientific and professional journals and conference proceedings home and abroad. His published scientific monograph is focused to the design of prestressed concrete structures and bridges. He has participated as a co-author in the development of the Technical conditions for practice (for Slovak Road Administration), focusing to the load carrying capacity of existing bridge structures. He has participated in the implementation of European standards for the design of concrete bridges STN EN 1992-2 into the system of Slovak standards. He is also co-author of the National Slovak Annex of that standard. He is acting as a lecturer at professional conferences and seminars "Design of concrete structures according to Eurocodes" (2006-2019), carried out within the educational activities of the Slovak Chamber of Civil Engineers (SKSI).

Piotr Olaszek, *Associate Professor at Road and Bridge Research Institute, Warsaw, Poland*

1. Date and place of birth: May 5, 1964, Warszawa

2. Diplomas and scientific degrees

- 1988 – MSc in Mechanical Engineering; Specialization: Automatic Control Engineering and Metrology at the Precision Mechanics Department of the Warsaw Institute of Technology; thesis title: *Wizyjna analiza jakości ekranów kineskopów* (Image analysis of kinescope screen quality) .

- 1996 – PhD in Technical Sciences in the scope of machines construction and exploitation at the Precision Mechanics Department of the Warsaw University of Technology; thesis title: *Wizyjno-komputerowa metoda wyznaczania charakterystyk dynamicznych w trudnodostępnych punktach konstrukcji mostowych*. (Investigation of the dynamic characteristic in difficult of access points of bridge structures by a computer vision method). Professor Małgorzata Kujawińska was the supervisor. In 2016 - obtaining the degree of habilitated doctor of technical sciences in the discipline of construction, with specialization in bridge construction, at the Faculty of Civil Engineering of the Warsaw University of Technology. Title of the scientific achievement: Application of digital measurement methods to bridge research.

3. Professional and scientific interests

- Bridge load testing
- Development of the research methods
- Interdisciplinary approach to the bridge structures testing connecting the elements of metrology, automatic control engineering and structural mechanics.
- Bridge monitoring and dynamics
- Standardization of the testing methods

Jia-Hua Yang, Guangxi University, China

Dr Yang is currently Associate Professor at College of Civil Engineering and Architecture and Scientific Research Center of Engineering Mechanics, Guangxi University (China). He obtained BEng (2010) from Central South University (China) and PhD (2015) in civil engineering from City University of Hong Kong. Before joining Guangxi University he was Assistant Professor at Tongji University (China).

Dr Yang specializes in both fundamental and applied research in advanced Markov chain Monte Carlo (MCMC) methods, Bayesian inference, optimization, reliability and risk analysis, structural health monitoring, and system identification. He has developed efficient multi-level MCMC methods that can efficiently update models of complex engineering systems and quantify uncertainties. He is experienced in full-scale dynamic testing of structures and has developed a fast method for modal analysis using field test data based on vector autoregressive model. He recently focuses on Bayesian learning of high-dimensional dynamic systems using MCMC methods. He is a recipient of the EASEC Young Researcher/Engineer Award (2019), ACMSM Stan Shaw Best Paper Award (2018) and HKIE Commendation Merit Award of Structural Excellence Award (2019,2021). He is a committee member of the Dynamics Committee of Engineering Mechanics Institute, ASCE and Review Editor (Editorial Board Member) of two journals, *Frontiers in Built Environment: Structural Sensing* and *Frontiers in Built Environment: Earthquake Engineering*.

Session 1

Monitoring and condition assessment of engineering structures

Experimental Investigation and Modelling of Concrete Exposed to Chlorides

P. Konecny¹, M. Hornakova¹, P. Lehner¹

¹ VSB – Technical University of Ostrava, Faculty of Civil Engineering, L. Poděštné 1875, Ostrava-Poruba 708 00, Czech Republic

1. Introduction

The aim of the contribution is to summarize selected experimental methods and numerical tools available at VŠB-TUO with respect to prediction and monitoring the deterioration of the concrete bridges. The durability of concrete bridge components may be affected by many negative factors. Corrosion of reinforcing steel caused by chloride ingress and carbonation are the most significant type of distress. Therefore, by accurately predicting and monitoring the deterioration of the concrete, engineers can manage structural systems in higher quality in order to resist degradation caused by long-term environmental and structural loads.

In this regard, the combination of experimental investigation and numerical modeling is important. For example, the reliability analysis of the remaining service life of a structure can be estimated based on nonlinear modeling of concrete stress-strain state including crack formation and feasible models of corrosion initiation and propagation. The numerical assessment of concrete behavior might be conducted in the ATENA Science software [1] that includes both chloride ingress as well as non-linear fracture models. The ATENA software contains the mechanical models based on finite element analysis with the utilization of nonlinear constitutive law of concrete and smeared crack band approach.

Also, in-house Matlab-based codes can be used for 1D/2D Chloride ingress [2, 3] and corrosion propagation analysis [3] (Korozeeneck). The penetration of chlorides into bridge structures is typically modeled as a diffusion process where the computation is based on the Second Fick's Law. The diffusion coefficient is a governing parameter describing the resistance of chloride penetration into the concrete. Diffusion coefficient might be obtained by the approximation of chloride profile from destructive penetration tests [4] or using the more advanced electrochemical tests such as electrical resistivity [5]. The approach implemented in the open source Korozeeneck software estimates time of the corrosion propagation according to Vidal et al. [6]. The model [6] is complemented with the initiation time period and an estimation of the corrosion current density developed by Morris et al. [7] based on the concrete resistivity values.

Not only the above-mentioned methods of analysis and experimental investigation but also other procedures may lead to the common goal of efficiently administrating existing structures and preparing new ones.

Acknowledgements

This contribution was prepared as a part of the international project VF 22110360 funded by Visegrad fund.

References

- [1] **V. Cervenka, L. Jendele, J. Cervenka**, *ATENA Program Documentation – Part 1: Theory*. Prague (CZ): Cervenka Consulting, 2007.
- [2] **P. Konecny and P. Lehner**. (2017). *Effect of cracking and randomness of inputs on corrosion initiation of rein-forced concrete bridge decks exposed to chlorides*. *Frattura ed Integrità Strutturale*. 11(39), pp. 29-37. Available: 10.3221/IGF-ESIS.39.04
- [3] **J. Brozovsky, P. Konecny, P. Ghosh**. (2011). *Evaluation of Chloride Influence on the Cracking in Reinforced Concrete Using Korozeeneck Software*. *Transactions of the VŠB – Technical University of Ostrava No.1. Vol.XI, Civil Engineering Series paper #6*. Available: 10.2478/v10160-011-0006-y
- [4] **AASHTO TP95-11, Standard Method of Test for Surface Resistivity Indication of Concrete's Ability to Resist Chloride Ion Penetration**. Washington, DC, USA: American Association of State and Highway Transportation Officials, 2011.
- [5] **NT BUILD 443, Concrete, hardened: Accelerated chloride penetration**. Espoo, Finland: Nordtest, 1995.
- [6] **T. Vidal, A. Castel, and R. Francois**. (2004). *Analyzing Crack Width to Predict Corrosion in Reinforced Con-crete*. *Cement and Concrete Research*. Vol. 34, pp.165-174. Available: 10.1016/S0008-8846(03)00246-1
- [7] **W. Morris, A. Vico, M. Vanquez, and S.R. Sanchez**. (2002). *Corrosion of Reinforcing Steel Evaluated by Means of Concrete Resistivity Measurements*. *Corrosion Science*. Vol. 44, pp. 81-99. Available: 10.1016/S0010-938X(01)00033-6

Assessment of prestressing effect in existing concrete bridges

Martin Moravcik ¹

¹ *University of Zilina, Civil Engineering Faculty, martin.moravcik@uniza.sk,*

1. Introduction

The first generation of precast girders were post-tensioned and transformed into an orthotropic slab using transversal post-tensioning. Currently, still about third of existing precast bridges built with this concept we have been using in service. The consequences of a deficient conceptual design and an inadequate maintenance will be shown using practical examples of two precast bridges under emergency condition close to collapse state. Structural defects and possible brittle character of collapsing were found on some girders. Fortunately, early closure of those bridges has prevented the fatal consequences. Detailed structural analysis and in-situ investigation and testing have been performed on those structures. As the main factors of superstructure failure we can identify corrosion of the prestressing wires, very bad condition of anchors protection and absence of grouting. Abstract summarizes the findings from testing and analysis of those girders. The results can help to assess the usability of similar bridge structures in future.

2. Characteristic failures of bridges

In a recent period were declared state of emergency on two of precast prestressed concrete bridges crossing the river Orava on the international route I/59 closed the villages Podbiel and Nizna at north part of Slovakia. The emergency state was declared due to the serious failures on the bearing structure were detected. The first generation of prestressed bridges made of precast elements began to be applied more extensively in the former Czechoslovakia during the 1950s to 1960s. The actual technical condition of the observed bridges has been manifest as the cause of the initial "childhood diseases" of building technology. As the main source of the failure state of this type has been total insufficient protection of prestressing reinforcement and anchors. For example, tendons were found very poor grouted and anchors were detected with insufficient or none concrete sheathing, see Fig. 1a). All these facts had been the crucial influence to the large deformation rising or wide crack opening in the girders, Fig. 1b).

Detected structural failures had been depended to the actual prestressing level as we know. To define the actual prestressing force in existing structures is very difficult task. Generally there are available any kind of destructive or non-destructive method but still complicated to use. We had used analytical and experimental approach in the form of Structure Response Method. In this abstract, we would like to present the results of performed testing method of prestressing, based on the fully scaled loading test and numerical analyses of deteriorated structure. Some result can be seen on prestressed girder on the Bridge Podbiel, Fig. 2.

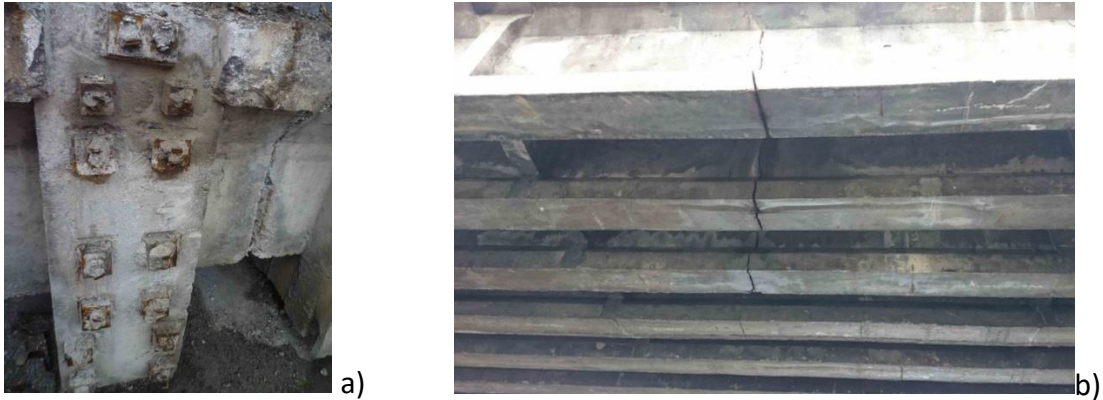


Figure 1 a). No sheathing on the anchors –Bridge Nizna, b). Crack in the girders - Bridge Podbiel.

3. Testing and analysis

One girder in relatively good technical condition was separated from orthotropic bridge deck (bridge Podbiel) and was full-scaled tested. There was obtained about 18 % reduction of assumed prestressing force in the girder.

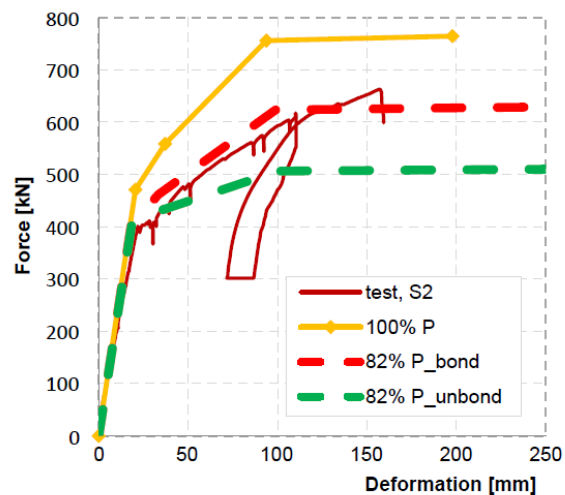


Figure 2. Bridge Podbiel - reduction of prestressing force in girder about 18%.

Acknowledgements

This research work was supported by the Slovak Grant Agency under contract No. 1/0045/19.

References

- [1] Moravcik, M., Bahleda, F., Bujnakova, P., Kralovanec, J.: *Structural Response Method Using to Actual Prestressing Level Assessment in Existing Bridges*, FIB Symposium Shanghai, China, Nov.22-24, 2020.
- [2] Häggstrom, J., Bagge, N., Nilimaa, J., Sas, G., Blanksvärd, T., Täljsten, B., Elfgrén, L.: *Testing Bridges to Failure – Experiences*, 39th IABSE Symposium, Vancouver, Canada. Sept. 21-23, 2017.

Innovative methods of measuring bridge displacements under static and dynamic loads

P. Olaszek ¹

¹ *Road and Bridge Research Institute, Poland,*

1. Introduction

Theoretical and experimental analysis of the displacements of bridge structures under static and dynamic load is important in long-term monitoring systems (SHM - structural health monitoring) or in short-term measurements (bridge load testing). The bridge displacement response is primarily sensitive to the stiffness of the bridge, whereas the acceleration response is affected by many other parameters so the bridge dynamic displacement is more suited than acceleration for updating the railway bridge stiffness [4]. Accurate measurements of deflections are also important in the validation of road bridge models [12].

The measurements of displacements in an automatic, unattended mode nearly always create considerable difficulties. Major difficulties are encountered especially in case of structures with restricted or impossible access to the area under them (bridges over busy roads, railway lines or rivers). In case of such located spans and additionally of great length problems appear both during static and dynamic measurements. Due to the specific nature of short-term bridge tests and long-term bridge monitoring, specially designed innovative systems are frequently used for displacement measuring. Making a reference to stable external or internal reference points is an important element of systems created for displacement measurement.

2. Computer vision method – external reference points

A special method for the investigation of the dynamic characteristic of bridges has been developed. It is based on the photogrammetric principle; however, the viewing system is equipped with an additional reference system, which decreases the sensitivity to vibrations and an analysis system which enables image analysis. The method is used for monitoring and real-time measurement of the displacement of chosen points at bridge structures [10]. The method presented is based on observation of bridge structure particular point using the CCD camera with telephoto-lens. The pattern, black cross on white background, is placed at the analyzed point and imaged by the optical system at the CCD matrix. Two alternative opto-mechanical systems are proposed: one- and two-channel system.

The first system (one-channel system) allows to observe one bridge point by a single camera. The camera is equipped with one telephoto lens of 1000 mm focal length. Many bridge tests have been carried out using this vision system and it has been observed that the reference system is one of the most important elements which dictates the measurement accuracy. The reference system has to provide the accurate displacement determination. There are two possibilities of reference system: location of a single point (point of camera position); location of two points - adding immovable points of tested structure which can be observed by the camera.

The second solution assumes additional monitoring of the reference (immovable) point which is usually situated at the nearest bridge support (Fig. 1). It requires introducing two-channel optical system which enables simultaneous imaging of measuring and reference points at the CCD matrix.

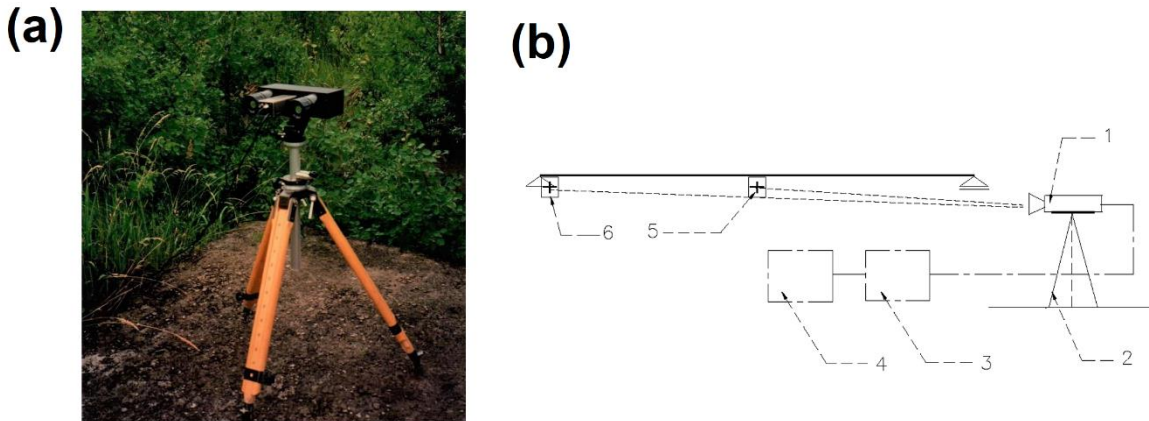


Figure 1. Additional reference point system; (a) photo of camera with two telephoto-lenses and stand; (b) vision system schema: 1 - camera and two telephoto-lenses, 2 - stand, 3 - computer and image digitizer, 4 - monitor, 5 - measuring pattern, 6 - reference pattern

tests was performed at the new highway bridge. During the dynamic test the deflections in midpoints (33 m span length) were measured. In the case of over-ground span the deflection was also measured by inductive sensors to test the vision method. The results of mechanical and vision methods were compared. After correction with the reference point the error of the vision method was equal to 0.1 mm (0.4 pixel). The maximum error without correction was equal to 1.6 mm (7.0 pixels).

The method was elaborated and presented above 20 years ago. It is still cited in many publications today with emphasis on the innovative method of vision-based dynamic measurement in two directions [1,5,6].

3. Static deflection monitoring system making use of inclinometers - internal reference points

Continuous multipoint deflection measurements (with sampling frequency of at least several times per minute) are difficult or practically impossible to be made in case of bridges with no possibility of equipment assembly under the examined spans). It is important to apply such measurement methods which give the possibility to measure bridge deflections without the necessity of using external reference points. Identification of this need has led to the development of a new measurement system, the main elements of which are inclinometers. The application of inclinometers to automatic monitoring of bridge structures under static and dynamic loading has often been presented in literature [2,3,7,9].

The new elaborated deflection monitoring system makes use of a network of inclinometers. Cubic spline curves which enhance the accuracy of the results are used in the calculation of deflection lines [11]. The designed system is able to monitor bridge deflections in one or two lines along the bridge. We can use one network (up to 20 inclinometers) to monitor one line along the bridge and two networks (up to 20 inclinometers) two monitor two lines along the bridge. The designed system was tested in monitoring of bridges during static load testing (Fig. 2).



Figure 2. Monitoring of the deflection during static bridge load testing; (a) view of the bridge; (b) inclinometers location at the bridge deck.

A series of comparative tests of displacement measurements with the use of inclinometers and the reference method (total station or inductive transducers) were carried out. The tests were carried out during static test loads on objects with different spans and thus different maximum values of the measured deflections. When using a set of 6 inclinometers, the discrepancies in the results ranged from 0.3 to 2.5% compared to the value measured by the reference method; with the measured maximum displacement values from 175.0 to 3.5 mm. All testing employ reading frequency of not less than 3 times per minute.

4. Dynamic deflection monitoring system making use of inclinometers and accelerometer - internal reference points

One of the most important elements of the developed solution is its innovative system of indirect measurement of displacements based on measurements using inclinometers and accelerometers. Many researchers present works on using accelerometers to measure both accelerations and displacements of bridges under dynamic loads. A disadvantage of this method is the necessity of double integration of an acceleration signal, which can lead to considerable errors in estimating the displacements. There are various methods suggested to correct those errors [8,16,17].

Whereas the method presented here is based on the integration of the signals from inclinometers and accelerometers. Inclinometers are installed in one line on a span and accelerometer at the point of displacement examination. The signals from the inclinometers are used to determine the so called quasi-static component of a displacement, and the signal from the accelerometer to determine a dynamic component [13,14]. A similar way of integrating the signals from an inclinometer and an accelerometer, used to determine lateral displacements of a railway bridge support is presented in [15].

The one-year tests of the system proved its usefulness for monitoring bridges in high-speed railway as well as its possibility to achieve high accuracy while determining displacements using an indirect method. The measurement errors determined using the indirect method in relation to a reference method did not exceed 0.84 mm (4.9%) for extreme values during separate locomotive EP09 and cars passages and did not exceed 0.54 mm (7.5%) for extreme values during Multiple-unit trains ED250 passages. The system presented herein was checked during one-year monitoring of the arch bridge located in high speed railway (Fig. 3).



Figure 3. Monitoring of the dynamic deflection under service load; (a) view of the bridge; (b) accelerometer and one of the three inclinometers and location at the bridge deck.

Acknowledgements

The presented works were done as part of the following projects: a) SPID – The mobile laboratory for the non-destructive pavement characteristics quantification; co-financed by the European Regional Development Fund under the Operational Program Innovative Economy; b) Applied Research Projects; co-financed by the National Centre for Research and Development, Poland in years 2015–2018

References

- [1] **J. Baqersad, P. Poozesh, C. Niezrecki, P. Avitabile**, *Photogrammetry and optical methods in structural dynamics – A review*, *Mechanical Systems and Signal Processing*. 86 (2017) 17–34.
- [2] **O. Burdet**, *Automatic deflection and temperature monitoring of a balanced cantilever concrete bridge*, in: 5th International Conference of Short and Medium Span Bridges, Calgary, Canada, 1998.
- [3] **O. Burdet, J.-L. Zanella**, *Automatic monitoring of the Riddes bridges using electronic inclinometers*, in: First International Conference on Bridge Maintenance, Safety and Management IABMAS, Barcelona, 2002.
- [4] **D. Feng, M.Q. Feng**, *Model Updating of Railway Bridge Using In Situ Dynamic Displacement Measurement under Trainloads*, *J. Bridge Eng.* 20 (2015) 04015019.
- [5] **D. Feng, M.Q. Feng**, *Computer vision for SHM of civil infrastructure: From dynamic response measurement to damage detection – A review*, *Engineering Structures*. 156 (2018) 105–117.
- [6] **Y. Fu, Y. Shang, W. Hu, B. Li, Q. Yu**, *Non-contact optical dynamic measurements at different ranges: a review*, *Acta Mech. Sin.* 37 (2021) 537–553.
- [7] **N.H. Gao, M. Zhao, S.Z. Li**, *Displacement Monitoring Method Based on Inclination Measurement*, *Advanced Materials Research*. 368 (2012) 2280–2285.
- [8] **M. Gindy, R. Vaccaro, H. Nassif, J. Velde**, *A State-Space Approach for Deriving Bridge Displacement from Acceleration*, *Computer-Aided Civil and Infrastructure Engineering*. 23 (2008) 281–290.
- [9] **X. Hou, X. Yang, Q. Huang**, *Using inclinometers to measure bridge deflection*, *Journal of Bridge Engineering*. 10 (2005) 564–569.

- [10] **P. Olaszek**, *Investigation of the dynamic characteristic of bridge structures using a computer vision method*, *Measurement*. 25 (1999) 227–236.
- [11] **P. Olaszek**, *Deflection monitoring system making use of inclinometers and cubic spline curves*, in: *Bridge Maintenance, Safety, Management and Life Extension*, CRC Press, 2014: pp. 2305–2312.
- [12] **P. Olaszek, M. Łagoda, J.R. Casas**, *Diagnostic load testing and assessment of existing bridges: examples of application*, *Structure and Infrastructure Engineering*. 10 (2014) 834–842.
- [13] **P. Olaszek, D. Sala, M. Kokot, M. Piątek**, *Railway bridge monitoring system using inertial sensors*, in: *Maintenance, Safety, Risk, Management and Life-Cycle Performance of Bridges*, Taylor & Francis Group, 2018.
- [14] **P. Olaszek, I. Wyczałek, D. Sala, M. Kokot, A. Świercz**, *Monitoring of the Static and Dynamic Displacements of Railway Bridges with the Use of Inertial Sensors*, *Sensors*. 20 (2020) 2767.
- [15] **A.I. Ozdagli, A.I., F. Moreu, J.A. Gomez, P. Garp, S. Vemuganti**, *Data Fusion of Accelerometers with Inclinometers for Reference-free High Fidelity Displacement Estimation*, in: *8th European Workshop On Structural Health Monitoring (EWSHM 2016)*, 5-8 July 2016, Spain, Bilbao, n.d.: pp. 1–9.
- [16] **J.-W. Park, S.-H. Sim, H.-J. Jung, B.F.S. Jr.**, *Development of a Wireless Displacement Measurement System Using Acceleration Responses*, *Sensors*. 13 (2013) 8377–8392.
- [17] **H. Sekiya, K. Kimura, C. Miki**, *Technique for Determining Bridge Displacement Response Using MEMS Accelerometers*, *Sensors (Basel)*. 16 (2016).

Session 2

Computer vision and its application in civil engineering

Deep convolutional neural networks for image-based detection of concrete surface cracks

M. Słoński

¹ Faculty of Civil Engineering, Cracow University of Technology, *marek.slonski@pk.edu.pl*

1. Introduction

Automatic image-based detection of surface defects such as concrete cracks is an important part of the vision-based structural health monitoring systems and condition assessment of civil infrastructure. Surface defects may indicate severe degradation processes being in progress in a structure. To this end, various image-based detection strategies of surface defects using computer vision and image processing methods were proposed. Currently, the most promising tools for fully automatic image-based defects detection are built with convolutional neural networks [1, 3, 5-7].

The main obstacle in the successful application of DCNNs for such problems is the lack of massive training datasets which are necessary to train large DCNNs from scratch. However, in the case of a small dataset it is still possible to build a reliable classifier and obtain the best results. It can be achieved by using a large ConvNet pretrained on a massive dataset from a similar domain [2].

In this work, we show the comparison of convolutional neural network architectures and training methods for detecting cracks in concrete pavements in the case of a small dataset. The comparison is based on the public benchmark dataset SDNET2018 [4].

2. Image-based detection of cracks

Image-based automatic detection of cracks can be formulated as a binary classification and solved by a classifier based on a neural network. The first step in building such a classifier is to collect images of structural parts containing cracks and without cracks. The second step is to build the classification model. Then we can apply the trained model to classify new images. In this work, we use deep convolutional neural networks for building an image-based classifier of concrete cracks. A schematic diagram illustrating this approach is shown in Fig. 1.

3. Experimental study

In this study, we compare four strategies for building a binary classifier for detecting cracks in images with a deep convolutional neural network (ConvNet):

- 1) a small ConvNet built from scratch,
- 2) a small ConvNet built from scratch with data augmentation,
- 3) a large pretrained ConvNet with data augmentation,
- 4) a large pretrained ConvNet with data augmentation and fine tuning.

In this work, we consider the case of a small dataset containing only a few thousands of images of pavements with crack and without crack and a balanced set of 5200 samples of images was prepared. The experiments were done using Keras on a Dell Inspiron 15 laptop computer with 64-bit operating system Windows 10, 32 GB RAM memory, Quad-Core Intel Core i7 processor and NVIDIA GeForce GTX 1060 Ti (4 GB) graphics processing unit (GPU).

Finally, the best ConvNet, with respect to validation accuracy, was checked using the testing set. The generalization accuracy for this ConvNet was close to 94%, which confirms that the best strategy for this problem was to apply the pretrained large network with fine-tuning.

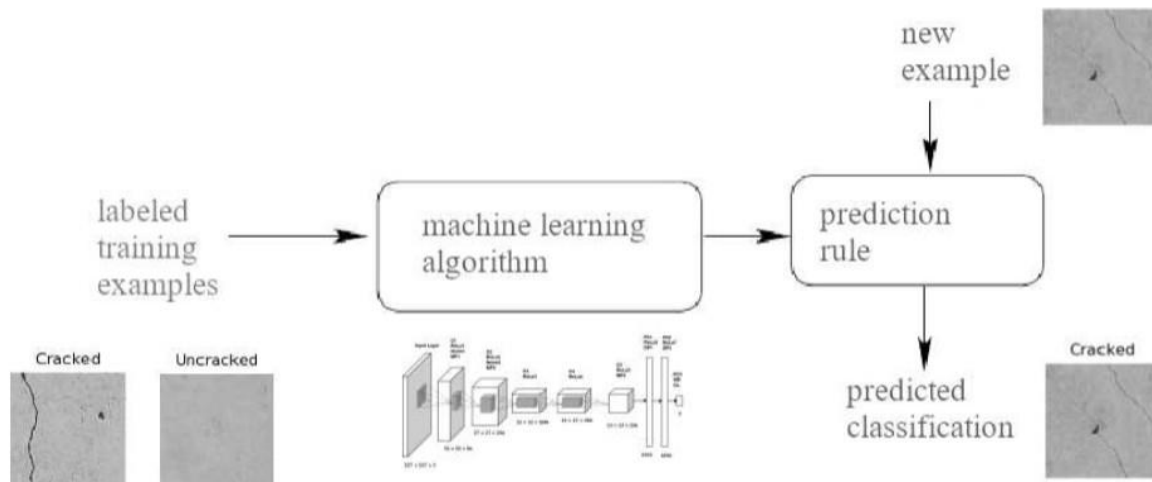


Figure 1. Diagram for image-based detection of concrete cracks using DCNN-based classifier.

References

- [1] Y.-J. Cha, W. Choi, O. Büyüköztürk. *Deep learning-based crack damage detection using convolutional neural networks*. Computer-Aided Civil and Infrastructure Engineering, 32(5): 361–378, 2017.
- [2] F. Chollet. *Deep Learning with Python*. Manning Publications Co., 2018.
- [3] S. Dorafshan, R.J. Thomas, M. Maguire. *Comparison of deep convolutional neural networks and edge detectors for image-based crack detection in concrete*. Construction and Building Materials, 186: 1031–1045, 2018.
- [4] S. Dorafshan, R.J. Thomas, M. Maguire. *SDNET2018: An annotated image dataset for non-contact concrete crack detection using deep convolutional neural networks*. Data in brief, 21: 1664–1668, 2018.
- [5] M. Słoński. *A comparison of deep convolutional neural networks for image-based detection of concrete surface cracks*. Comput. Assist. Methods Eng. Sci., 26, 105–112, 2019.
- [6] M. Słoński, K. Schabowicz, E. Krawczyk. *Detection of flaws in concrete using ultrasonic tomography and convolutional neural networks*. Materials, 13(7), 1557, 2020.
- [7] M. Słoński, M. Tekieli. *2D digital image correlation and region-based convolutional neural network in monitoring and evaluation of surface cracks in concrete structural elements*. Materials, 13(16), 3527, 2020.

Advances in applicable deep-learning based defect detection

M. Żarski ^{1,2,1}, B. Wójcik ^{1,2}, K. Książek ², M. Salamak ¹, J. A. Miszczak ²

¹ *Silesian University of Technology, Faculty of Civil Engineering, Akademicka 5, 44-100 Gliwice, Poland, mateusz.zarski@polsl.pl*

² *Institute of Theoretical and Applied Informatics, Polish Academy of Sciences, Bałtycka 5, 44-100 Gliwice, Poland.*

1. Introduction

Early detection of infrastructure defects like cracks of small width can lead to lowering the overall costs of infrastructure through the incorporation of preventive maintenance [1,2]. However, such defects are often omitted during manual inspections – in fact over 60% of small defects are never included in Infrastructure Inspectors reports [3–5], which causes invalid scores of the facilities, and thus invalid future infrastructure maintenance plans. While there already exists methods for automatic defect detection with the use of deep learning methods [6–8], it can be argued that they are not applicable in the reality of infrastructure maintenance. They require vast computing power for training and inference that excludes the use of edge or mobile devices, but still, even with vast resources are limited to low resolution images [9].

In this work we present you our path that led us to reaching practical applicability of deep learning algorithms for infrastructure defect detection and placed us in the fields' state-of-the-art territory. Throughout our studies we developed KrakN – an end-to-end, open source and scalable framework for transfer learned deep learning model development intended for minimizing the training time and allowing the use of a single backbone CNN for multiple defect classifiers. Then we were among the first who tackled the problem of pruning transfer learned CNN models with our Finicky Transfer Learning (FTL) method, which allowed us for pruning as much as 95% of CNNs' parameters while maintaining its initial accuracy. We also present our further plans for refining our work in order to push the field even further and match the accuracy of the computationally heaviest solutions while maintaining high applicability of our methods.

2. Defect detection with transfer learning

The main goal of our research was to enable the practical use of deep learning methods for infrastructure defect detection. In order to do so, we identified the basic problems that prevent the use of already existing methods in practice – the need of vast computing power for training the model, lack of scalability and versatility, and the need of expert knowledge in the field of deep learning to adapt the solution to specific needs.

The KrakN [10] framework created by us is the answer to these problems by offering end-to-end methods of deep learning model development suited for users without background in data science. Its principle of operation is shown in Figure 1. KrakN uses a single CNN as a backbone feature extractor for multiple defect

classifiers, and offers tools for semi-automatic development of datasets. The tests we have carried out have shown that KrakN is characterized by a greater ability to generalize knowledge than analogous solutions that do not use transfer learning, when target datasets differ from the training one, *e.g.* in the appearance of a concrete surface. It scored above 90% in accuracy of detecting cracks with width under 0,2mm.

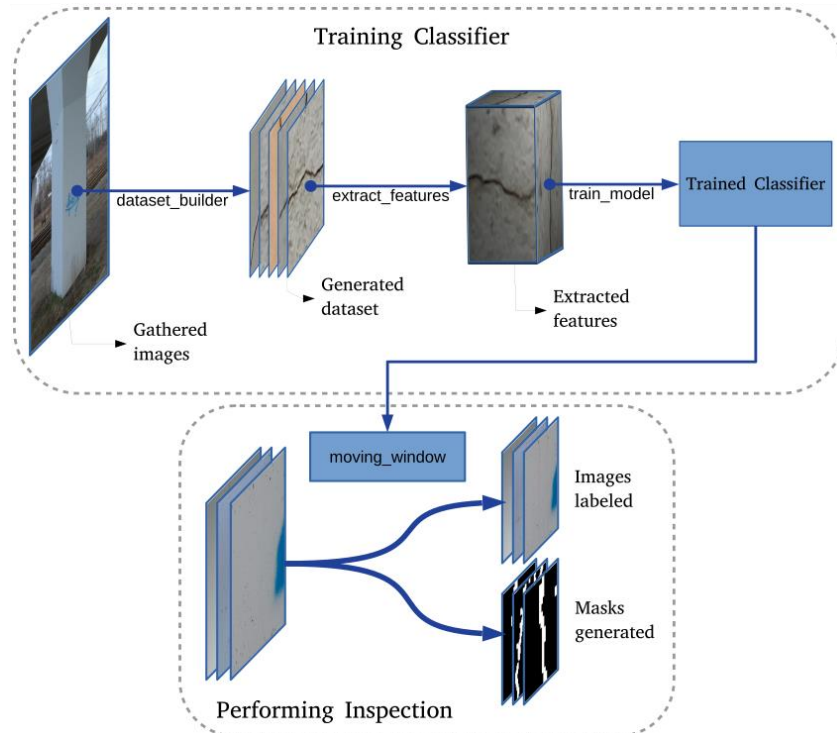


Figure 1. Workflow of KrakN framework

KrakN uses sliding window method for object detection in order to be able to detect defects regardless of the image size – it can process large format orthomosaics obtained with photogrammetric reconstruction unlike methods based on single shot detectors which are limited by the size of input image. It also comes as an open source solution and can be easily modified. An example of such a modification is the add-on module prepared by us, which allows for multi-classifier approach presented in earlier works [11], but was never made available publicly.

KrakN was also our initial step to further developing methods based on transfer learning and adapting them for use on edge devices.

3. Transfer learning with pruning

An extension of our methods using transfer learning is the Finicky Transfer Learning [12] – CNN structural pruning method that allows for limiting the demand for computing power by reducing the number of algorithm parameters.

It uses the Jaccard similarity coefficient (**IoU**) for assessing adaptation of subsequent CNN filters trained on the external data set to the new type of the searched object. It is assessed to what extent convolutional filters are able to extract features from multiple images, within the damage area. Then, without retraining the CNN, only its layers with highest mean IoU score are used as feature extractor for the new classifier.

The method of obtaining mean IOU score is described with equation 1, where X^{seg} is the set of all images with defect segmented out, $f_j^i(x_k)$ is image segmented with the j -th filter of the i -th network layer, x_k^s is image segmented manually, and m is the total number of images in dataset.

$$\overline{IoU}(X^{seg}, f_j^i) = \frac{1}{m} \sum_{k=1}^m \left(\frac{|x_k^s \cap f_j^i(x_k)|}{|x_k^s \cup f_j^i(x_k)|} \right) \quad (1)$$

With the use of Finicky Transfer Learning we were able to reduce the total number of CNN parameters by up to 95% while maintaining its initial accuracy. It enabled the effective use of single board edge devices like Raspberry Pi computers. The comparison of image processing time with CNN pruned with FTL method compared to unpruned network running inference on high-performance, 6 core CPU is shown in Figure 2.

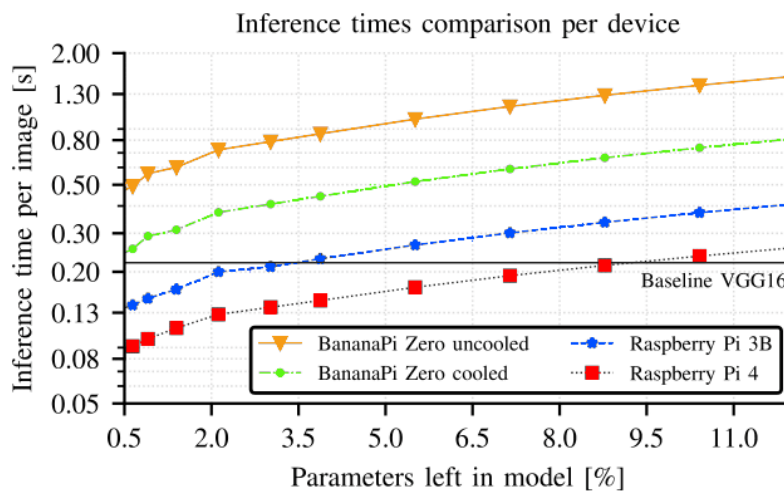


Figure 2. Comparison of pruned CNN inference times on edge devices

It can be seen that single board edge devices can run inference with CNN models pruned with FTL method with performance matching high-performance CPU. Moreover, when considering that FLT uses transfer learning, the classifier part of the CNN is also trained much faster than with the use of full, unpruned model.

4. Future goals

The experience we have gained while working on the KrakN framework and the FTL method has led us to start working on a method that uses structural CNN pruning during the training of the model. We believe that by using our pruning method during fine tuning of the model, we will be able to raise the final model accuracy metrics above the initial values of the full, unpruned CNN, while greatly reducing its number of parameters.

We are also considering modifying the pruned CNN with the utilization of various micro architectures. By doing so we'll be able to enrich the final feature tensor with features extracted by the initial layers of the model and thus increase the number of image characteristics for the classifier.

Acknowledgements

Work presented in this study was supported by the *European Union* through the *European Social Fund* as a part of a *Silesian University of Technology as a Centre of Modern Education based on research and innovation* project, number of grant agreement: **POWR.03.05.00 00.z098/17-00** (BW and MŻ).

References

- [1] **H. Singh**, *Repair and retrofitting of bridges – present and future*, in: Proc. 9th Int. Conf. Bridg. Maintenance, Saf. (IABMAS 2018), 2018: pp. 1209–1215.
- [2] **C.S. Shim, N.S. Dang, S. Lon, C.H. Jeon**, Development of a bridge maintenance system for prestressed concrete bridges using 3D digital twin model, Struct. Infrastruct. Eng. 15 (2019) 1319–1332. <https://doi.org/10.1080/15732479.2019.1620789>.
- [3] **B.A. Graybeal, B.M. Phares, D.D. Rolander, M. Moore, G. Washer**, Visual inspection of highway bridges, J. Nondestruct. Eval. 21 (2002) 67–83. <https://doi.org/10.1023/A:1022508121821>.
- [4] **B.M. Phares, B.A. Graybeal, D.D. Rolander, M.E. Moore, G.A. Washer**, Reliability and accuracy of routine inspection of highway bridges, Transp. Res. Rec. (2001) 82–92. <https://doi.org/10.3141/1749-13>.
- [5] **B.M. Phares, G.A. Washer, D.D. Rolander, B.A. Graybeal, M. Moore**, Routine Highway Bridge Inspection Condition Documentation Accuracy and Reliability, J. Bridg. Eng. 9 (2004) 403–413. [https://doi.org/10.1061/\(ASCE\)1084-0702\(2004\)9:4\(403\)](https://doi.org/10.1061/(ASCE)1084-0702(2004)9:4(403)).
- [6] **Y. Liu, J. Yao, X. Lu, R. Xie, L. Li**, DeepCrack: A deep hierarchical feature learning architecture for crack segmentation, Neurocomputing. 338 (2019) 139–153. <https://doi.org/10.1016/j.neucom.2019.01.036>.
- [7] **B. Kim, S. Cho**, Automated Vision-Based Detection of Cracks on Concrete Surfaces Using a Deep Learning Technique, Sensors. 18 (2018). <https://doi.org/10.3390/s18103452>.
- [8] **S. Li, X. Zhao, G. Zhou**, Automatic pixel-level multiple damage detection of concrete structure using fully convolutional network, Comput. Civ. Infrastruct. Eng. 34 (2019) 616–634. <https://doi.org/10.1111/mice.12433>.
- [9] **B. Wójcik, M. Żarski**, Assessment of state-of-the-art methods for bridge inspection: case study, Arch. Civ. Eng. 66 (2020) s. 343-362. <https://doi.org/10.24425/ace.2020.135225>.
- [10] **M. Żarski, B. Wójcik, J.A. Miszczak**, KrakN: Transfer Learning framework for thin crack detection in infrastructure maintenance, (2020) 1–23. <http://arxiv.org/abs/2004.12337>.
- [11] **P. Hüthwohl, R. Lu, I. Brilakis**, Multi-classifier for reinforced concrete bridge defects, Autom. Constr. 105 (2019) 102824. <https://doi.org/10.1016/j.autcon.2019.04.019>.
- [12] **M. Żarski, B. Wójcik, K. Książek, J.A. Miszczak**, Finicky Transfer Learning -- a method of pruning convolutional neural networks for cracks classification on edge devices, Comput. Civ. Infrastruct. Eng. (2021). <https://doi.org/10.1111/mice.12755>.

Extracting crack characteristics from RGB-D images

B. Wójcik¹, M. Żarski², M. Salamak³, J. A. Miszczak⁴

1Faculty of Civil Engineering, Silesian University of Technology, bartosz.wojcik@polsl.pl

1Institute of Theoretical and Applied Informatics, Polish Academy of Sciences, bwojcik@iitis.pl

2Faculty of Civil Engineering, Silesian University of Technology, mateusz.zarski@polsl.pl

2Institute of Theoretical and Applied Informatics, Polish Academy of Sciences, mzarSKI@iitis.pl

3Department of Mechanics and Bridges, Faculty of Civil Engineering, Silesian University of Technology, marek.salamak@polsl.pl

4Institute of Theoretical and Applied Informatics, Polish Academy of Sciences, jmiszczak@iitis.pl

1. Introduction

The images acquired by RGB-D camera (**Figure 1**) provide a unique opportunity for vision-based structural health monitoring (SHM). The addition of a fourth channel, the depth, that encodes 3D data enables not only defect detection but also extraction of its characteristics, like surface area or volume. In addition, the resulting three-dimensional damage representations can be easily used to enrich BIM models to as-is state. However, there are some limitations as these type of sensors were not built with precision in mind, rather real-time data acquisition. This results in noisy depth data and low-resolution RGB sensors.

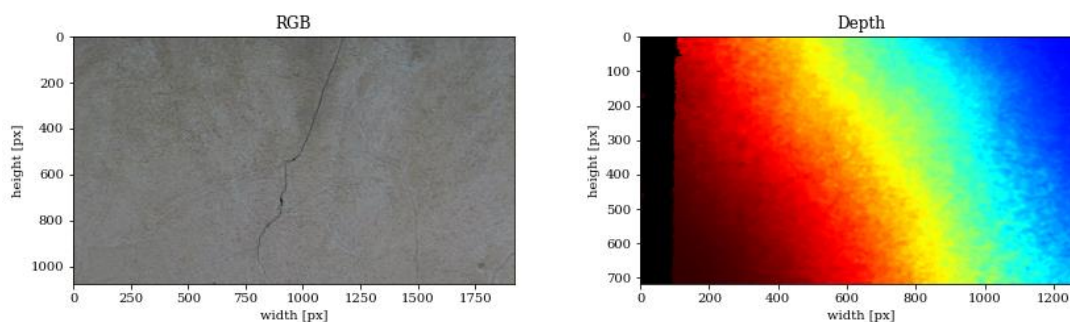


Figure 1. RGB-D image of a cracked concrete surface.

Nevertheless, these sensors found applications in SHM context. Authors of [1] presented a method that combines RGB-D data with deep learning to perform volumetric measurements of spalling, and a method for surface area measurements of defects (rust stains, efflorescence, contamination) was presented in [2]. However, the limitations mentioned above hinder application for crack assessment, as authors of [3] had to pair depth sensor with hi-resolution DSLR camera to enable crack width measurement.

On the other hand, creating high-resolution (HR) images out of low-resolution (LR) ones with deep learning is an active field of research. This type of task is called super-resolution (SR), and could enhance performance of low-cost RGB-D sensors (**Figure 2**).

This workshop proceeding presents results from initial experiment with super-resolution (SR) enhanced crack width measurement using low cost RGB-D sensor, namely Intel RealSense D435i.

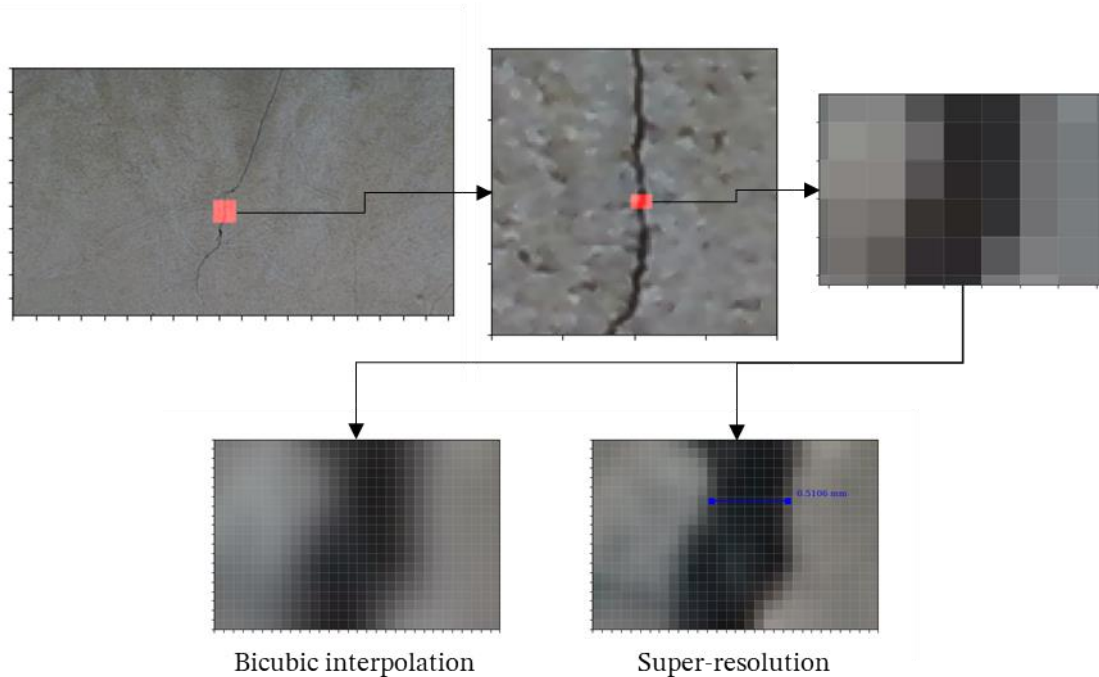


Figure 2. Comparison of two images upscaled with different methods, simple bicubic interpolation and super-resolution deep learning model [4].

Acknowledgements

Work presented in this study was supported by the *European Union* through the *European Social Fund* as a part of a *Silesian University of Technology as a Centre of Modern Education based on research and innovation* project, number of grant agreement: *POWR.03.05.00 00.z098/17-00* (B.W. and M.Ż.).

References

- [1] **G. H. Beckman, D. Polyzois, and Y. J. Cha**, (2018), *Deep learning-based automatic volumetric damage quantification using depth camera*, *Automation in Construction*, vol. 99, no. November 2018, pp. 114–124, doi: 10.1016/j.autcon.2018.12.006.
- [2] **B. Wójcik and M. Żarski**, (2021), *The measurements of surface defect area with an RGB-D camera for a BIM-backed bridge inspection*, *Bulletin of the Polish Academy of Sciences: Technical Sciences*, vol. 69, no. 3, pp. 1–9, doi: 10.24425/bpasts.2021.137123.
- [3] **H. Kim, S. Lee, E. Ahn, M. Shin, and S. H. Sim**, (2020), *Crack identification method for concrete structures considering angle of view using RGB-D camera-based sensor fusion*, *Structural Health Monitoring*, doi: 10.1177/1475921720934758.
- [4] **X. Wang, L. Xie, C. Dong, and Y. Shan**, (2021), *Real-ESRGAN: Training Real-World Blind Super-Resolution with Pure Synthetic Data*, [Online]. Available: <http://arxiv.org/abs/2107.10833>

Causality Based Image Classification

L. Pospíšil¹, V. Dornák^{1,2}, M. Čermák¹

¹ *Department of Mathematics, Faculty of Civil Engineering, VŠB-TU Ostrava, Czech Republic,*

² *Department of Applied Mathematics, FEECS, VSB-TU Ostrava, Czech Republic,*

Corresponding author: lukas.pospisil@vsb.cz

1. Introduction

The contribution shortly presents the novel approach for image classification and possible crack detection based on the Bayesian model and conditional probabilities. The approach has been firstly presented in the Master thesis [1] and nowadays is precisely examined in large-scale settings. In contrast with the most popular Neural Network approach, the considered old-school method is based on the description of points by numerical gradients of the neighborhood of the pixels. During the learning phase, each (labelled) image is processed by feature extraction method, e.g., histogram of oriented gradient (HOG, [2]), speeded up robust features (SURF, [3]), which produces the interest points, i.e., descriptors, which characterizes the given image. The number of descriptors for each image can be different, but the dimension of each descriptor is the same. The descriptors of all images are used for the computation of the so-called Bag of Visual Words (BoVW, [4]) - descriptors are clustered into groups, e.g., words. This stage is typically performed using the K-means algorithm. Using the BoVW, we count the number of descriptors of each cluster and construct the histogram of relative frequencies of descriptors words for every image. This histogram characterizes the image: it expresses the probability representation of visual words in a given image. The last step is to find the classification rule for the probability representation. In this case, one of the most popular algorithms is the Support Vector Machine (SVM).

In our opinion, the solution of the problem by stages in the pipeline introduces additional errors - we would like to rather solve problems simultaneously: we would like to find the optimal clustering of descriptors (BoVW) such that the supervised classification will be optimal. Motivated by [5], we combine the Scalable Probabilistic Approximation (SPA) optimization problem and direct Bayesian model (BM) with Kullback–Leibler divergence [6] using the aggregation of the corresponding multicriteria optimization problem.

This paper presents the basic ideas behind the combined methods and preliminary results.

2. Direct Bayesian model for determining the causality

To describe the causality between the affiliation frequencies of HOG (or SUFT) descriptors in the given image and the classification of the image, we consider a direct BM (also well-known as Law of total probability)

$$\pi_t^Y = \Lambda \pi_t^X, t = 1, \dots, T, \quad (1)$$

where π_t^X is a discrete probability vector of affiliation of pixel of index t into the BoVW and π_t^Y is a discrete probability vector of descriptor classification. The unknown left-stochastic matrix Λ consists of unknown conditional probabilities. To learn these probabilities from given training set, we adopt the regression with KL divergence, i.e., we minimize the sum of distances between two stochastic vectors derived from the given data

$$\Lambda^* = \operatorname{argmin} \sum_{t=1}^T \sum_{m=1}^M [\pi_t^Y]_m \log \left(\frac{[\pi_t^Y]_m}{[\Lambda \pi_t^X]_m} \right). \quad (2)$$

3. Scalable Probabilistic Approximation

Instead of using standard BoVW, we are considering the probabilistic extension of the approach represented by the adaptation of Scalable Probabilistic Approximation (SPA), which is only a recently presented approach for adaptive probability discretization [5]. The idea can be understood as a generalization of K-means clustering algorithm and it is based on the law of total probability and the concept of conditional expectation, which has been originally proposed to define the causality between two categorical processes. However, this approach can be combined with optimal clustering which introduces a general model for dealing with continuous processes.

The squared Euclidean measure is used to define the distance between D_t descriptors of each $t = 1, \dots, T$ image and it approximates the representation in BoVW. This distance is equivalent to NSE and RMSE [7]. The corresponding problem of optimal classification and clustered representation is given by

$$[S^*, \Gamma^*] = \operatorname{argmin} \sum_{k=1}^K \sum_{t=1}^T \sum_d^{D_d} \left\| x_{t,d} - \sum_{k=1}^K [\Gamma_{t,d}]_k [S]_{:,k} \right\|, \quad (3)$$

where S represents the stochastic BoVW (sBoVW) of size K and Γ is a stochastic affiliation of descriptors.

4. The aggregation and the solver

We combine optimization problems (1) and (2) into the problem, which solves both of the problems simultaneously

$$[S^*, \Gamma^*, \Lambda^*] = \operatorname{argmin} \sum_{k=1}^K \sum_{t=1}^T \sum_d^{D_d} \left\| x_{t,d} - \sum_{k=1}^K [\Gamma_{t,d}]_k [S]_{:,k} \right\| + \epsilon \sum_{t=1}^T \sum_{m=1}^M [\pi_t^Y]_m \log \left(\frac{[\pi_t^Y]_m}{[\Lambda \pi_t^X]_m} \right), \quad (4)$$

where $\pi_t^X = \frac{1}{D_t} \sum_{d=1}^{D_t} \Gamma_{t,d}$ are relative frequencies of words in given image and $\epsilon > 0$ is aggregation parameter.

Motivated by SPA algorithm and K-means, we solve the problem (4) using the subspace algorithm – we fix two variables and solve the problem in remaining one. It is easy to show that such an algorithm produces the non-increasing sequence of objective function and the method converges to local optimality point. To find the global solution, we run the algorithm with several initial approximations. This paper presents the basic ideas behind the combined methods and preliminary results.

5. Preliminary results

The Figure 1 presents our experiences with the solution of simple benchmark consisting of 20 rendered images of cube and 20 rendered images of the sphere. We used SURF algorithm to detect the key points and construct the optimal sBoVW with causality matrix to detect the significancy of points to image classes.



Figure 1. Image classification: The optimal BoVW on simple benchmark - blue significant points are significant for cubes, yellow points are for spheres.

Additionally, we test the presented approach on the crack detection problem. We compute the HOG of pixels in two images – one of them with the crack and the second one without crack. We provide the information about the presence of the crack in the image only in the form of whole image classification. However, the preliminary results shows the robustness of our method – the algorithm identifies the pixels significant for the image with crack – these pixels are actually the pixels which include the crack, see Figure 2.

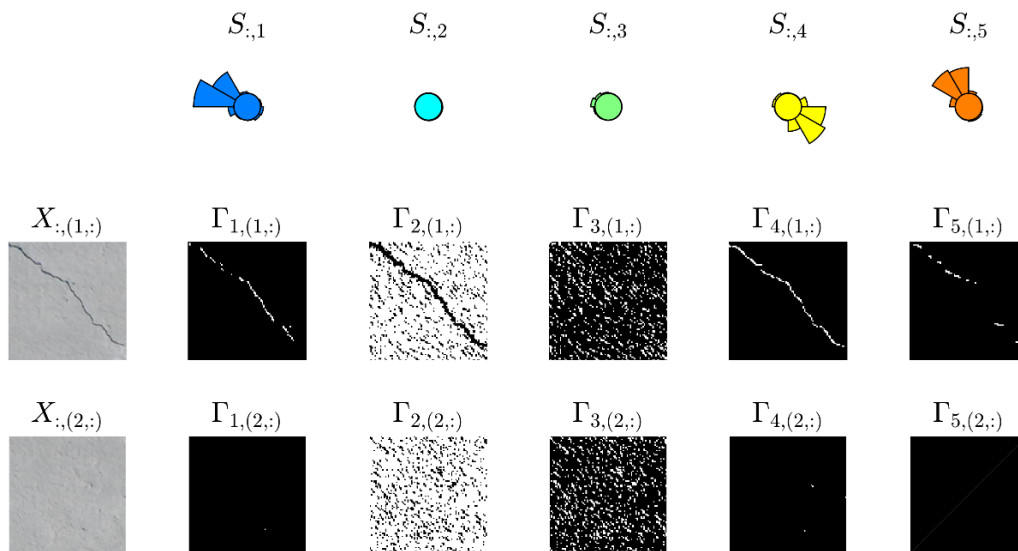


Figure 2. Training results: the upper part shows the centroids represented by average histograms of gradients, the middle and the last rows presents the data and the sBoVW affiliation functions (white=1, black=0).

Pixels without crack are not significant for the image with crack. In Figure 3, we present results on 8 validation images – on these images, the model has been not trained. Used images are adopted from the standard crack detection benchmark database [7].

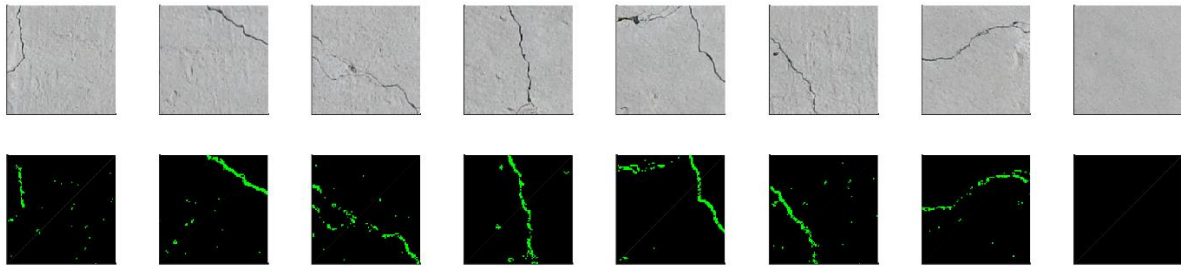


Figure 3. Validation: the application of learned model to new images; upper row shows the original images, lower row presents the solution $\Lambda^* \Gamma$, the green color corresponds to the probability of detecting crack, i.e., $[\Lambda^* \Gamma_{t,:}]_{1,:}$.

Acknowledgements

This contribution has been developed as a part of the research project GACR 21-14886S "Influence of Material Properties of High Strength Steels on Durability of Engineering Structures and Bridges" supported by the Czech Grant Agency and the financial support provided to VSB-Technical University of Ostrava by the Czech Ministry of Education, Youth and Sports from the budget for conceptual development of science, research and innovations for the 2021 year.

References

- [1] **V. Dorňák.** (2021). *Algorithms used for classifying visual signals using methods for extracting significant features*, Master thesis, VŠB-TU Ostrava, supervised by L. Pospíšil. Available online: <https://dspace.vsb.cz/handle/10084/143861?locale-attribute=en>.
- [2] **N. Dalal and B. Triggs.** (2005). *Histograms of oriented gradients for human detection*. IEEE Computer Society Conference on Computer Vision and Pattern Recognition (CVPR'05). 886–893.
- [3] **H. Bay, A. Ess, T. Tuytelaars, and L. Van Gool.** (2008). *Speeded-up robust features (SURF)*. Computer Vision and Image Understanding. 110, 3, 346-359.
- [4] **A. Suharjito and D. Santika.** (2017). *Content based image retrieval using bag of visual words and multiclass support vector machine*. ICIC Express Letters. 11, 10, 1479-1488.
- [5] **S. Gerber, L. Pospíšil, M. Navandar, and I. Horenko.** (2020). *Low-cost scalable discretization, prediction, and feature selection for complex systems*. Science Advances. 6, 5.
- [6] **S. Kullback and R. A. Leibler.** (1951). *On Information and Sufficiency*. Annals of Mathematical Statistics. 22, 1, 79–86.
- [7] **D. Dlouhá, V. Dubovský, and L. Pospíšil.** (2021). *Optimal Calibration of Evaporation Models against Penman–Monteith Equation*. Water. 13, 11.
- [8] **S. Dorafshan, R.J. Thomas, and M. Maguire.** (2018). *An annotated image dataset for non-contact concrete crack detection using deep convolutional neural networks*. Data in brief, 21, 1664–1668.

Session 3

Dynamic system identification using Bayesian approach

Bayesian Identification of Engineering Dynamic Systems Based on Vector Autoregressive Model

Jia-Hua Yang ¹

¹ College of Civil Engineering and Architecture, Guangxi University
Scientific Research Center of Engineering Mechanics, Guangxi University
Email: javayang@gxu.edu.cn

Abstract

Due to fast development of sensing technology, a huge amount of data is available every second. This offers a perfect opportunity to improve mathematical modeling based on measured data, but also poses a challenge at the same time, because extracting useful information from data for complex engineering dynamic systems is time consuming. This paper presents a newly developed Bayesian system identification method based on vector autoregressive (VAR) model [1],[2]. A dynamic system is first modeled by a VAR model. Because the information contained in data is always incomplete and there are uncertainties, the identification of the VAR model is formulated as a Bayesian learning problem where the plausible models and the associated uncertainties are learned by identifying the probability density function (PDF) of the VAR model parameters. Following Bayes' theorem, the posterior PDF of the VAR parameter matrices is derived. The most probable values and posterior covariance matrices of the uncertain VAR parameter matrices are then derived in close form for efficient calculation. It is shown that a VAR model is equivalent to the dynamic model of a vibrating structure, so natural frequencies, damping ratios and mode shapes can be obtained from a VAR model by solving the eigenvalue problem of a matrix constructed by VAR parameter matrices. Based on the first-order Taylor's series expansion, the posterior uncertainties of VAR parameters are propagated to modal parameters. Analytical formulas of the posterior uncertainties of modal parameters are derived for efficient calculation in practical applications.

This paper also develops a method for Selecting the most probable model class for a VAR model conditional on measured data, when it is used for system identification. One challenge of using a VAR model for system identification is to select a suitable order, which can be viewed as selecting a suitable model class for a VAR model. Following Bayes' theorem, the model class selection problem is rigorously solved by calculating the evidence of each competing model class and selecting the most probable model class with the largest evidence. The new formulation for evaluating the extremely high-dimensional integral involved in calculating the evidence of a model class is derived analytically based on the Laplace's method of asymptotic expansion. The most probable modal parameters of a structure can be obtained using the identified most probable VAR model class. The proposed method is validated using an experimental case.

The proposed method is applied for a tall office building and a factory building. The results show great potential of this method.

Acknowledgements

The author is funded by National Natural Science Foundation of China (Grant No. 51808400) and National Key Research and Development Program of China (Grant No. 2020YFC1512504). The generous support is gratefully acknowledged. Part of this work was done when the author was with Department of Disaster Mitigation for Structures, Tongji University, and the generous support is greatly appreciated. The author would like to thank Professor Paul Lam from City University of Hong Kong for providing the factory building data and valuable suggestions. The author would also like to thank Mr. Stephen Yiu for logistics help on the field test. The contributions of Dr. Stephen Alabi, Dr. Jun Hu, Dr. Qin Hu, Dr. Yan-Chun Ni, Mr. Stephen Yiu, and Dr. Feng-Liang Zhang to the field test are greatly appreciated.

References

- [1] **J.H. Yang, H.F. Lam.** (2019). *An innovative Bayesian system identification method using autoregressive model*. Mechanical Systems and Signal Processing. 1, 133, 106289.
- [2] **J.H. Yang, Q.Z. Kong, H.J. Liu., H.Y. Peng** (2021). *Efficient Bayesian model class selection of vector autoregressive models for system identification*. Structural Control and Health Monitoring. e2780

Bayesian approach for efficient identification of highly uncertain structural parameters

M. Ostrowski ¹, B. Błachowski ², G. Mikułowski ³, Ł. Jankowski ⁴

Institute of Fundamental Technological Research, Polish Academy of Sciences

¹ mostr@ippt.pan.pl, ² bblach@ippt.pan.pl, ³ gmikulow@ippt.pan.pl, ⁴ ljank@ippt.pan.pl

1. Introduction and motivation

This study is devoted to Bayesian approach for parametric identification of a structure equipped with semi-actively lockable joints. Such joints can operate in two different states: unlocked (working as a hinge) or locked (transmitting bending moment). They can be used to provide the effect of modal coupling that allows to precisely control of the mechanical energy flow between vibration modes [1]. The fact that locking/unlocking of the joint removes/adds one rotational degree of freedom (DOF) introduces additional difficulty related to the nonlinear nature of such a reconfigurable system.

Classical methods for modal updating based on mode sensitivity require comparison of modal parameters extracted from measurement data with those obtained numerically. Major disadvantage of this approach is a mode matching problem, because often not all modes are identified during measurement and their order can be inconsistent with the updated model [2, 3]. Moreover, due to mode switching effect numerically calculated modes can change during model updating process. Therefore in this study, a Bayesian approach-based probabilistic framework [4] is proposed that allows to overcome the above mentioned problems.

2. Structure under consideration

Steel structure shown in Figure 1a is equipped with six lockable joints. Beams and lockable joints are connected by screws. Such a connection is characterized by highly uncertain stiffness. Additionally, structural parameters of individual joint-beam connection exhibit significant discrepancies due to inaccuracy of assembly process. These manufacturing errors were clearly visible during measurements by unsymmetrical mode shapes (see: Fig. 3). Hence, each beam-joint is parametrized independently on each other to reproduce these imperfections in the updated model.

In the modal updating procedure only measurements of the structure with joints in locked state are taken into account. The reason is residual friction-driven moment of the joint in unlocked state because the friction parts are still in contact, but with lower value of the clamping force. It causes additional nonlinearities, hence it is more convenient to identify the system for the locked state of the joints. In this case friction force is sufficiently large to avoid slipping of the friction parts in the joint and their relative motion does not take place. Details about the lockable joints can be found in [1, 5].

Finite element (FE) model representing the structure and parametrization of the uncertain beam-joint connections is shown in Figure 1b. A class of FE models $(\mathbf{M}, \mathbf{K}(\boldsymbol{\theta})) \in \mathcal{C}$ is considered, where \mathbf{M} is constant mass matrix and $\mathbf{K}(\boldsymbol{\theta})$ is stiffness matrix defined as follows:

$$\mathbf{K}(\theta_1, \theta_2, \dots, \theta_{N_t}) = \mathbf{K}_0 + \sum_{t=1}^{N_t} \theta_t \mathbf{K}_t, \quad (1)$$

where \mathbf{K}_0 is stiffness-matrix component related to well-known part of the structure, i.e. to steel profiles, whereas constant matrix-components $\mathbf{K}_t = k_t \mathbf{L}_t^T \mathbf{L}_t$ scaled by the parameters θ_t describe sought stiffnesses of the beam-joint connections. Here this connection is represented by stiffness between two rotational DOFs k_t (see: Fig. 1b, zoomed joint) and \mathbf{L}_t is Boolean matrix responsible for placement of t -th connection. There are 16 parameters describing all beam-joint connections. Steel profiles are represented by FEs based on Euler-Bernoulli beam theory with cubic shape functions. Joints are represented by rigid bodies with defined masses and mass-inertia moments.

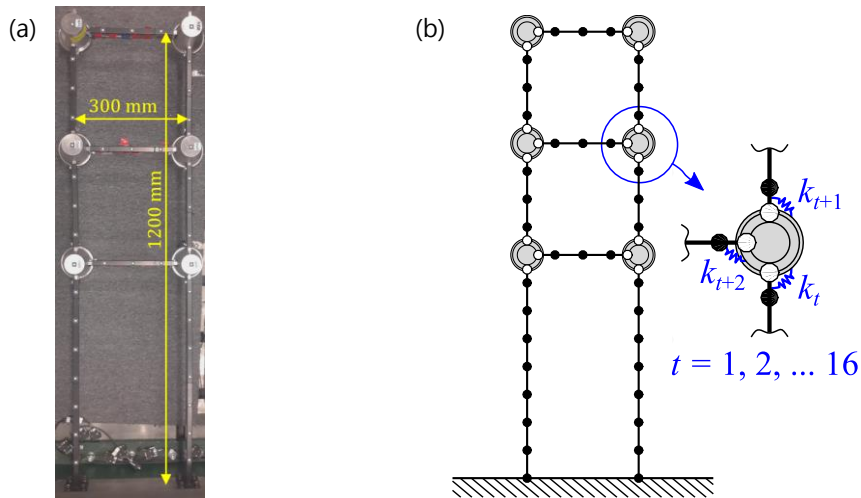


Figure 1. (a) laboratory structure equipped with six lockable joints, (b) mesh of FE model and parametrization of each beam-joint connection

3. Identification of the system parameters with Bayesian approach

In Bayesian approach the most probable values of $\boldsymbol{\theta} = [\theta_1 \ \theta_2 \ \dots \ \theta_{N_t}]^T$ are sought based on experimental data according to prior gaussian probability density function:

$$J(\boldsymbol{\lambda}, \boldsymbol{\phi}, \boldsymbol{\theta}) = -2 \ln p(\boldsymbol{\lambda}, \boldsymbol{\phi}, \boldsymbol{\theta} | \boldsymbol{\lambda}_{\text{exp}}, \boldsymbol{\phi}_{\text{exp}}) \quad (2)$$

where: $\boldsymbol{\lambda}_{\text{exp}} = [\omega_1^2 \ \omega_2^2 \ \dots \ \omega_{N_m}^2]^T$ is vector of squares of measured natural frequencies (rad^2/s^2), vector $\boldsymbol{\phi}_{\text{exp}} = [\boldsymbol{\phi}_{\text{exp}}^{(1)T} \ \boldsymbol{\phi}_{\text{exp}}^{(2)T} \ \dots \ \boldsymbol{\phi}_{\text{exp}}^{(N_m)T}]^T$ collects measured mode shapes. $\boldsymbol{\lambda}$, $\boldsymbol{\phi}$ and $\boldsymbol{\theta}$ that minimize function J are sought. Since both mathematical model as well as measured data are subjected to certain errors, vectors of random variables $\boldsymbol{\lambda}$ and $\boldsymbol{\phi}$ contain most probable system parameters, whereas $\boldsymbol{\theta}$ most probable parameter values of the FE model. In the Bayesian framework we do not postulate that numerically calculated modes are equal to measured ones so mode matching problem disappears. Iterative procedure of finding optimal values of $\boldsymbol{\lambda}$, $\boldsymbol{\phi}$ and $\boldsymbol{\theta}$ is described in [4].

In order to examine whether parameters are correctly defined the identifiability of the model parameters is checked. Parameters are identifiable at some search space if likelihood $L(\boldsymbol{\theta})$ function has only one maximum over such defined domain [6]. Function $L(\boldsymbol{\theta})$ is given by following equation:

$$\begin{aligned} L(\boldsymbol{\theta}) &= K K_\lambda \hat{p}(\mathcal{D}_\lambda | \boldsymbol{\theta}, \mathcal{C}) K_\phi \hat{p}(\mathcal{D}_\phi | \boldsymbol{\theta}, \mathcal{C}) \\ &= K L_\lambda(\boldsymbol{\theta}) L_\phi(\boldsymbol{\theta}), \end{aligned} \quad (3)$$

where $\hat{p}(\cdot)$ is prior gaussian probability density function, \mathcal{D}_λ is set of measurement data of natural frequencies, \mathcal{D}_ϕ is set of measurement data of mode shapes, $L_\lambda(\boldsymbol{\theta})$ is likelihood function corresponding with natural frequencies, whereas $L_\phi(\boldsymbol{\theta})$ for mode shapes, coefficients K , K_λ and K_ϕ are scale factors normalising likelihood functions to one at their maximums. From equation (3) it is evident that identifiability depends not only on chosen parametrization, i.e. class of models \mathcal{C} , but also available measurement data contained in \mathcal{D}_λ and \mathcal{D}_ϕ .

4. Results

First, identifiability of vector $\boldsymbol{\theta}$ has been checked. Likelihood function $L(\boldsymbol{\theta})$ has been verified with full-review method for large search space. Hence, tremendous computational effort related to identification of 16 parameters (see: Fig. 1b) has been replaced with reduced two-parameter set: $\tilde{\boldsymbol{\theta}} = [\tilde{\theta}_1 \quad \tilde{\theta}_2]^T$, where $\tilde{\theta}_1$ is related to all vertical beam-joint connections, whereas $\tilde{\theta}_2$ to all horizontal ones. Rotational stiffness $k_t = 10^4$ Nm/rad, $t = 1, 2, \dots, 16$, has been selected. The search space Θ with the following dimensions has been used: $(\tilde{\theta}_1, \tilde{\theta}_2) \in [10^{-1}, 10^2] \times [10^{-2}, 10^2]$.

Only one maximum of likelihood function $L(\tilde{\boldsymbol{\theta}})$ has been found in Θ , so parameters $\tilde{\theta}_1$ and $\tilde{\theta}_2$ are identifiable. Functions $L_\lambda(\tilde{\boldsymbol{\theta}})$, $L_\phi(\tilde{\boldsymbol{\theta}})$ and $L(\tilde{\boldsymbol{\theta}})$ in neighbourhood of optimal values of $\tilde{\boldsymbol{\theta}}$ are shown in Figure 2. Function $L(\tilde{\boldsymbol{\theta}})$ has greater gradients so it provides more precise information about parameters sought than $L_\lambda(\tilde{\boldsymbol{\theta}})$ and $L_\phi(\tilde{\boldsymbol{\theta}})$. It is consequence of greater amount of measurement data.

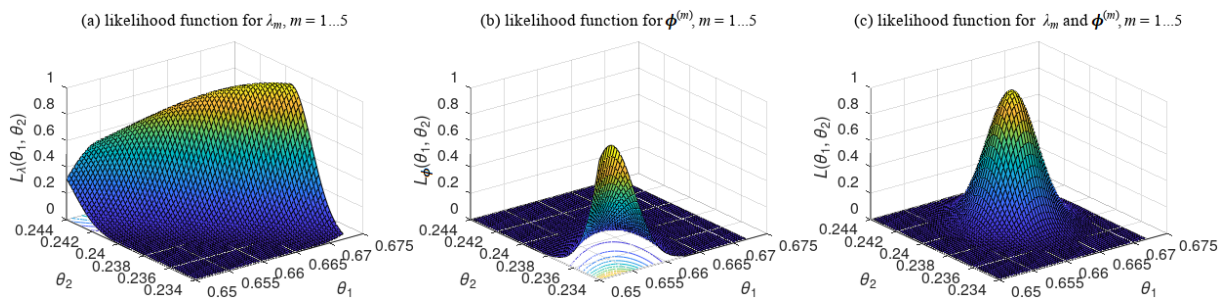


Figure 2. (a-c) likelihood function around neighborhood of optimal parameter values for various measurement data sets of first five modes

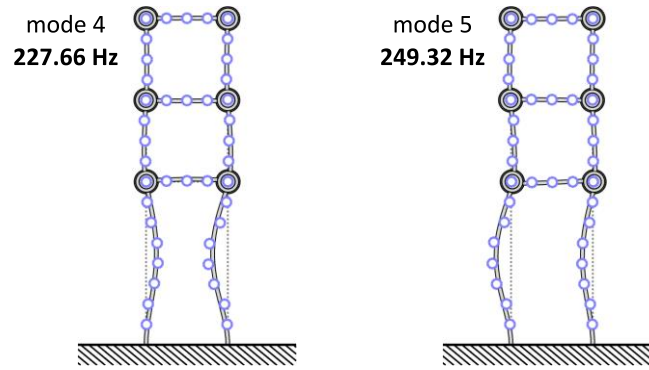


Figure 3. Comparison between mode shapes of updated FE model (gray structure) and measurement data (blue points), natural frequencies in the figure are taken from measurement

Table 1. Final values of: updating parameters, frequency relative error and MAC for updated model

legend:		θ_1	θ_2	θ_3	θ_4	θ_5	θ_6	θ_7	θ_8
		0.46	0.90	1.06	1.06	1.08	0.17	0.77	0.28
		θ_9	θ_{10}	θ_{11}	θ_{12}	θ_{13}	θ_{14}	θ_{15}	θ_{16}
		1.12	1.20	0.32	0.40	0.39	0.24	0.23	0.35

mode [-]	4	5
$\frac{f_m^{exp} - f_m(\theta)}{f_m^{exp}}$ [%]	-1.67	1.76
MAC [-]	0.89	0.91

Finally, comparison between selected examples of mode shapes identified experimentally and ones calculated numerically using Bayesian approach (eq. (2)) is shown in Figure 3. Initial parameter values for iterative updating procedure were chosen as appropriate parameters $\tilde{\theta}_t$, for which $L(\tilde{\theta})$ achieves maximum, magnified by 1.6. One can see that due to independently parametrized beam-joint connections numerically calculated mode shapes are very well fitted to asymmetric mode shapes identified experimentally. Final values of parameters θ , frequency errors and MAC values are listed in Table 1.

5. Conclusions

Bayesian approach for model updating allows to avoid the mode matching problem. Accurate estimation of the local parameters of the structure subjected to high uncertainties is possible. It includes the higher-order modes that are very sensitive to parametric modifications and can change their order during model updating.

References

[1] M. Ostrowski, B. Błachowski, B. Popławski, D. Pisarski, G. Mikułowski, Ł. Jankowski. (2021). *Semi-active modal control of structures with lockable joints: general methodology and applications*. Structural Control and Health Monitoring, vol. 28, Issue 5, p. e2710. Available: <https://doi.org/10.1002/stc.2710>.

[2] M. Friswell, J. E. Mottershead. *Finite Element Model Updating in Structural Dynamics*. Dordrecht: Springer, 1995. Available: <https://doi.org/10.1007/978-94-015-8508-8>.

- [3] **J. E. Mottershead, M. Link, M. I. Friswell.** (2011). *The sensitivity method in finite element model updating: A tutorial*. Mechanical Systems and Signal Processing, vol. 25, issue 7, pp. 2275-2296. Available: <https://doi.org/10.1016/j.ymssp.2010.10.012>.
- [4] **K.-V. Yuen, J. L. Beck, L. S. Katafygiotis.** (2006). *Efficient model updating and health monitoring methodology using incomplete modal data without mode matching*. Structural Control and Health Monitoring, vol. 13, issue 1, pp. 91-107. Available: <https://doi.org/10.1002/stc.144>.
- [5] **B. Popławski, G. Mikułowski, R. Wiszowaty, Ł. Jankowski.** (2021). *Mitigation of forced vibrations by semi-active control of local transfer of moments*. Mechanical Systems and Signal Processing, vol. 157, p. 107733. Available: <https://doi.org/10.1016/j.ymssp.2021.107733>.
- [6] **K.-V. Yuen.** *Bayesian Methods for Structural Dynamics and Civil Engineering*. Singapore: John Wiley & Sons (Asia), 2010. Available: <https://doi.org/10.1002/9780470824566>.

Session 4

Systems for autonomous inspections of civil infrastructure

Autonomous platforms in civil engineering practice

Á. Barsi ¹, J. M. Lógó ²

¹ Dept. Photogrammetry and Geoinformatics, Budapest University of Technology and Economics, barsi.arpad@emk.bme.hu

² Dept. Photogrammetry and Geoinformatics, Budapest University of Technology and Economics, logo.janos.mate@emk.bme.hu

Abstract

Autonomous platforms generally have the ability and the necessary technical instrumentation to perform environmental observation, process these data to extract information about the objects and their states, and have suitable control tools (algorithms and actuators) to decide in various situations and continuously govern the behavior of the platform. Speaking about vehicles, this definition is easy to interpret: a car equipped with cameras, LiDARs, radars, and similar sensors to monitor its neighborhood, which evaluates these observations and have corresponding data processing and decision making systems and controls the car's movement to reach the expected traveling goal with safety and effective fuel use. The described phases are based on sensory and algorithmic developments, where most experts agree that artificial intelligence must be embedded into the onboard automotive workflow. The smooth and reliable working requires enormous computing power both onboard and off-board as well as effective communication among other vehicles in motion and service providers. Civil engineers haven't been limited to transportation vehicles, but further mobile platforms can be understood within autonomous systems, like robots and similar machines. Autonomously moving and acting platforms must not be limited to road and railroad traffic but can play a role in water and air circumstances (transportation). More interestingly, surveying and inspecting platforms are also useful devices that help maintain pipe networks, complex steel and concrete structures (traverses, towers, bridges, and similar structures). These robots have proper moving (climbing, rolling, crawling, etc.) mechanisms and are equipped with data collection tools (measurement instruments, sampler units, cameras, etc.). Data are stored onboard and/or transferred immediately via an adequate communication channel. Civil engineers expect – of course – builder robots from the near future development; robots that participates in the construction workflow. One can order disaster mitigation devices (rescue robots after earthquakes or water floods) also into the civil engineering system category.

Acknowledgements

The authors are grateful for the financial support received from the joint grant of the Hungarian and the Polish Academy of Sciences and the Hungarian Ministry of Human Resources (ÚNKP-21-3-II-BME-26) as well as from the project "Development of regional network on autonomous systems for structural health monitoring" financed by the Visegrad Fund.

Paradigm change of mapping in the advent of driverless transportation

J. M. Lógó ¹, Á. Barsi ²

¹ Dept. Photogrammetry and Geoinformatics, Budapest University of Technology and Economics,
logo.janos.mate@emk.bme.hu

² Dept. Photogrammetry and Geoinformatics, Budapest University of Technology and Economics,
barasi.arpad@emk.bme.hu

1. Introduction

Since humanity started moving around, it has been looking for easier, faster, and more convenient transportation. In the continuous evolution of vehicles, the involvement of machines has been revolutionary. A similar revolution is the abandonment of the machine, which is autonomous or self-driving transportation.

The emergence of self-driving vehicles is the result of a long technical evolution [1]. Improvements have been made in three main areas: vehicle control, safety, and comfort. Initially, human-driven vehicles were gradually equipped with more and more helping solutions, so-called assistants [2]. The Driver Information System (DIS) provided information on the status of the vehicle and the environment. For example, a car equipped with a camera detects the speed limit indicated on traffic signs and signals this to the driver. The Tire Pressure Monitoring System (TPMS) constantly monitors the air pressure in the tires and alerts in case of deviation.

The next stage of development is Driver Assistance Systems (DAS). The main aim is to improve safety, initially by improving the braking system to deal with emergency situations. The Anti-lock Braking System (ABS) and Brake Assist (BA) improve wheel slip and thus vehicle controllability. An improved version of this is Autonomous Emergency Braking Assist (AEB). Cruise Control (CC) or tempomat is a speed-keeping assist that controls the vehicle moving at a preset speed. An advanced version can also detect the vehicle ahead and adjust the speed accordingly; this is Adaptive Cruise Control (ACC).

The Advanced Driver Assistance Systems (ADAS) is the next evolution stage. The Lane Departure Warning System (LDW), which monitors the road ahead with a camera, helps the driver to keep in lane with warnings, while the Lane Keeping Assist System (LKAS) corrects the driver by carefully steering the vehicle back into its lane. Blind Spot Monitor (BLIS) warns the driver of vehicles not visible in the rear-view mirror. Lane Change Assist (LCA) supports lane changes by monitoring blind spots and performing lane-change maneuvers. In a motorway environment, Highway Pilot is a system that can serve both speed maintenance and lane-change maneuvers.

Through the above assistants, we can see how solutions with progressively more and more functionality are helping the driver, ultimately taking over more and more activities from the driver. The Society of Automotive Engineers (SAE) International has developed a classification of vehicle maturity levels based on these factors, defining six different levels. These levels are [3]:

Level	Name	Steering/ acceleration/ deceleration	Environment monitoring	Fallback	System capability
Human driver monitors the driving environment					
0	No automation	H	H	H	–
1	Driver Assistance	H/S	H	H	some driving modes
2	Partial Automation	S	H	H	some driving modes
Automated driving system monitors the driving environment					
3	Conditional Automation	S	S	H	some driving modes
4	High Automation	S	S	S	many driving modes
5	Full Automation	S	S	S	all driving modes

Table 1. Automation level defined by SAE International [3]
(H – human driver, S – system)

The above table shows that full self-driving is only achieved at the top level (Level 5); for this goal, a number of intermediate levels have to be reached, i.e., the conditions have to be met (this also indicates that it is a time-consuming process, despite all promises made in advertisements!)

Autonomy means in the automotive context that the vehicle is capable to

- gain information about the environment,
- work for an extended period without human intervention,
- move throughout its operating environment without human assistance,
- avoid situations that are harmful to people, property.

The same set of conditions can be applied to robots, so a self-driving vehicle can also be considered a robot. For example, a cab with this capability is often called robotaxi.

To understand the needs of autonomous vehicles, it is worth taking a look at how they work. Figure 1 summarizes the essential components for the operational model [4]. According to the scheme, the state of the environment can be sensed by the different sensors and its objects can be detected. In addition to the information extracted, the decision mechanism can also receive input from the vehicle's communication unit and the map. The control of the vehicle is based on the decision through various interventions. The map is therefore a significant source of data for the decision process in addition to its own perception and communication.

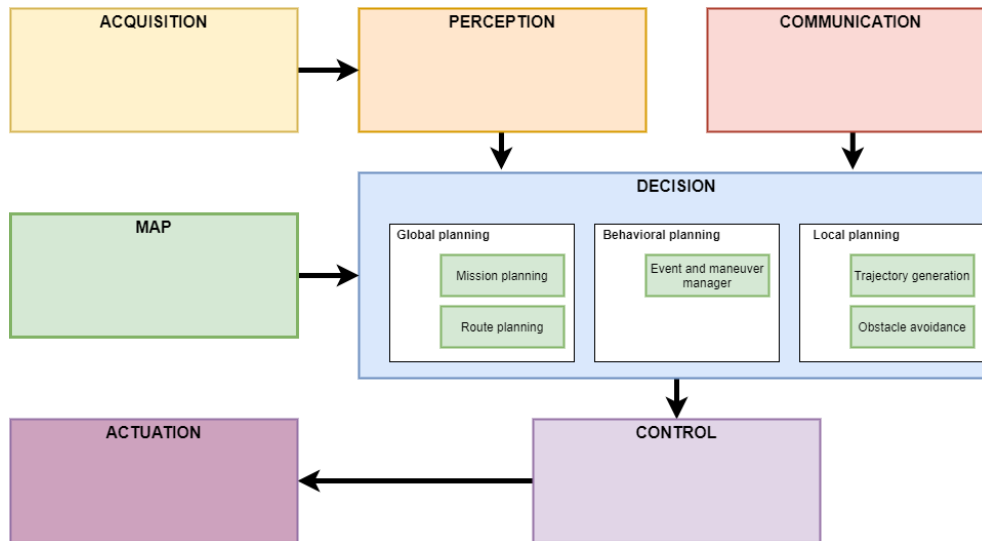


Figure 1. Functional component blocks in a vehicle (after Sz. Aradi)

2. Changes in maps

Maps have always played a central role in transportation [5]. In the beginning, paper maps, atlases, and later navigation solutions offered a variety of options to help drivers find their proper way. The availability of satellite positioning (GPS) has dramatically improved the navigation toolbox. However, self-driving vehicles require much more detail and orders of magnitude more accuracy than a human driver.

Let's briefly review the evolution of maps. There are two major parts of the process: the change in form and the change in content. In terms of map formats, the most significant improvement has been due to the digitalization of analog (paper) maps. In addition, another milestone was the replacement of the CAD-like storage model by databases.

In terms of the content, the map was initially a two-dimensional representation, which gradually became three-dimensional. There is a big difference in the content when we move from the road-level representation to the lane-level. In the latter case, a complete description of the road infrastructure is provided with all traffic lane data. A further noteworthy change is the ever-improving description of the environment: the keyed (pictographic) representation of the main environmental elements (e.g., some buildings, churches, gas stations, etc.) has been transformed into an accurate spatial geometric description of all built and natural objects: object models and three-dimensional point clouds are used. However, the map is not yet complete: the introduction of dynamic content is the most significant development. The modern map (which is now a database!) includes increasingly dynamic elements such as road closures and construction works, weather elements, the current status of traffic lights, and even the road users themselves. The EU-funded SAFESPOT project has provided the technological basis for such an approach [6].

3. Mapping technologies

The technology commonly used to produce maps relies on a method of field geodesy. When measuring, the surveyor visits all the points to be measured, determines their geometric position, and records them as

map points. It has the advantage of measuring only the minimum number of points needed but has the disadvantage of being extremely expensive and slow.

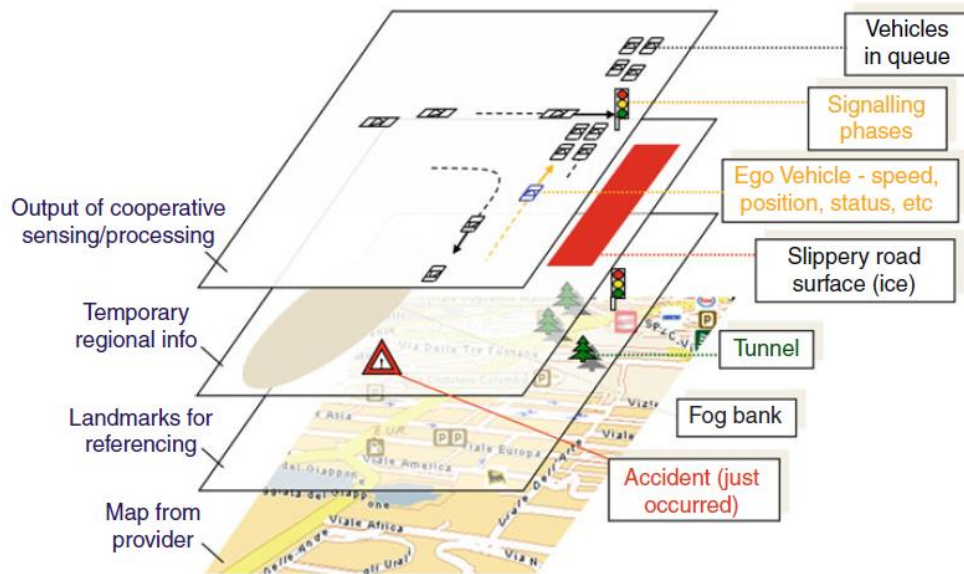


Figure 2. The extended layer structure of Local Dynamic Map (LDM) as proposed by SAFESPOT [6]

Terrestrial laser scanning (TLS) captures millions of points per second, making it a much faster, more efficient method. Part of the work is done in the field, while the other, larger part is executed in the office (unlike geodesy, where the bulk of the work happens in the field). TLS, therefore, has the advantage of increased measurement performance, while the disadvantage is that it requires expertise and powerful hardware support for data processing.

Aerial photographs are taken from aircraft, which can be evaluated to produce maps of larger areas with homogeneous accuracy. This method – called photogrammetry – also has the advantage of being cost-effective but has the disadvantage of being highly dependent on weather conditions, requiring a high level of expertise, and being quite expensive for the whole project.

Images can also be purchased from remote sensing imagery providers. Satellite images can be used for mapping over an even larger area than aerial imagery. Still, they require particular attention to cloud cover and are much less detailed than aerial solutions. Expertise is an indispensable requirement for this technology.

Drones (unmanned aerial vehicles – UAVs) are all the rage these days, also suit great for mapping tasks. Easy-to-obtain devices make it easy to collect pictures of the earth's surface and process them in various applications. The advantage of the UAV method is that it is easy to use and quick to set up, but the disadvantage is the small survey area and the variable accuracy of the resulting product.

Mobile mapping is the best solution in terms of detail, geometric accuracy, and processing methodology. In this methodology, the measuring instruments are mounted on a mobile platform, such as a van, together with a positioning unit, and a detailed survey of the roads and their surroundings is carried out. Mobile mapping primarily uses cameras and laser scanners to acquire data. The technology can be used to survey a large network of roads in a cost-effective way, but the equipment itself is expensive to purchase. The

evaluation of the results is the main part of the work, which is also done in an office environment. From a quality point of view, this method seems the best one in supporting self-driving. A typical mobile mapping system is shown in the following figure.



Figure 3. A Leica Pegasus Two mobile mapping system mounted on top of a car

4. Conclusion

Future road transportation has been dreamed with driverless, i.e., self-driving vehicles. These cars, trucks, and buses are equipped with environmental sensor systems (cameras, laser scanners, radars, and similar devices). The captured data must be processed in an acceptable time frame, where the onboard computers and the corresponding communication platforms have extreme importance. The behavior of these vehicles depends then highly on the extracted information about the moving and non-moving objects in the vicinity. The decision-making procedure here considers the influencing environment. Still, it guides the vehicle to the desired goal, keeping in mind the safety (ego and the environment) and the effectiveness (concerning fuel, time, costs, etc.).

The above efforts are realized by complex vehicular systems, which also contain the capability to handle map information. Maps of these vehicles store significantly more information; road and lane focus, but other infrastructure objects also: buildings, bridges, tunnels, trees and vegetation, water bodies, railways, traffic signs, and signals – the list can be continued for a long time. Self-driving vehicle maps must therefore be compiled in a different way; unfortunately, the well-known technologies have to be replaced with more

appropriate ones. Modern technologies like artificial intelligence, big data analyses, effective computing algorithms should be encapsulated into the map-making workflow. Up-to-date maps have fresh and valid content, which requires a suitable update mechanism. Vehicle control can accept only methodologies that are constantly reliable, so all the necessary methods undergo a serious quality check and validation test series. The map content is – at the very end – not only geometrically but topologically correct and consistent, while the attributes are also verified. Static map disappears, and a dynamic map database penetrates the automotive location description progress.

Acknowledgements

The authors are grateful for the financial support received from the joint grant of the Hungarian and the Polish Academy of Sciences and the Hungarian Ministry of Human Resources (ÚNKP-21-3-II-BME-26) as well as from the project “Development of regional network on autonomous systems for structural health monitoring” financed by the Visegrad Fund.

References

- [1] **Á. Barsi** et al., *Az önvezetés térképi támogatása*, *Geodézia és Kartográfia*, vol. 72, no. 2, pp. 10–15, 2020, doi: 10.30921/GK.72.2020.2.2.
- [2] **H. Winner** et al. Eds., *HandbuchFahrerassistenzsysteme*, 3. Springer Fachmedien Wiesbaden, 2015.
- [3] **J3016B**: *Taxonomy and Definitions for Terms Related to Driving Automation Systems for On-Road Motor Vehicles - SAE International*. https://www.sae.org/standards/content/j3016_201806/ (accessed Jul. 21, 2020).
- [4] **R. Matthaei and M. Maurer**, *Autonomous driving - A top-down-approach*, *At-Automatisierungstechnik*, vol. 63, no. 3, pp. 155–167, 2015, doi: 10.1515/auto-2014-1136.
- [5] **N. Krausz** et al. *Az autós térképtől az önvezetésig: a járműnavigáció története*, *Geodézia És Kartográfia*, vol. LXXI, no. 1, pp. 14–18, 2019, doi: 10.30921/GK.71.2019.1.1.
- [6] **A. Eskandarian**, *Handbook of intelligent vehicles*, vol. 1–2. Springer London, 2012.

Coverage Path Planning for a Fleet of Industrial Cleaning Robots

J. Szklarski¹

¹ *Institute of Fundamental Technological Research, Warsaw, Poland, jszklar@ippt.pan.pl*

1. Introduction

One of the fundamental applications of autonomous robotic platforms is to perform coverage tasks: area inspection, surveillance, creating image mosaics, structural monitoring, mowing, harvesting, planting, mapping, searching, painting, controlling CNC machines, and more. Such problems require that a robot (or – generally – a tool) at some time will visit a certain region of the environment, eventually visiting, or observing, the entire region of interest. Additionally, any obstacles should be avoided. Moreover, other optimization criteria can be incorporated in the process (e.g., minimizing time or energy). In order to do so, a Coverage Path Planning (CPP) algorithm must be employed [1,2]. Generally, it is a difficult problem, especially if realistic, noisy motion models or measurement errors are taken into account (even the classical “lawnmower problem” in its simplest form is NP-hard). A group of cooperating robots can realize the coverage in a faster and more robust way than a single unit. However, the underlying CPP should be designed appropriately.

2. Multi-robot CPP

In order to solve CPP, robots must: 1) move through all the points in the target area covering it completely; 2) preferably without an overlapping path; 3) robots must avoid all obstacles; 4) simple motion trajectories; an optimal (in some way) path is desired. Depending on formulation, the CPP is related to the covering salesman problem (a variant of the traveling salesman), the lawnmower problem, the art gallery problem and the watchman route problem – all NP-hard.

CPP algorithms can be divided in various classes, depending on: operating environment (2D, 3D, building, outdoor); algorithm processing (online, offline, centralized, distributed); model-based, non-model-based (no prior knowledge of the structure or environment); map representation (grid based with various possible shapes, triangular, square, hexagon, diamond; cell decomposition; geometric path generation); optimization goal (time, number of robots, energy, maximize monitoring area, multiobjective, etc.).

We propose a practical solution of a CPP for a group of robots whose task is to clean large scale storage facilities (the cleaning radius is much smaller than a warehouse). The algorithm is based on a decomposition of a 2D environment map into a set of polygons. The input to the algorithm is a 2D grid map representing a static environment, i.e. permanent obstacles (walls, elements of infrastructure, etc.) in a factory or a storage facility. Due to a large scale and required resolution, algorithms based on occupancy grid maps are not suitable. Therefore, in the first step the map is decomposed into a set of polygons. Two methods of decomposition can be applied: trapezoidal and boustrophedon. The latter is a generalization of the trapezoidal decomposition, but has more efficient coverage paths consisting of simple back and forth motions. Regarding optimality, the total time of cleaning is to be minimized.

The polygons are represented as a Reeb graph, where nodes have associated time-cost of cleaning and edges represent a single cell to be covered. The graph is further divided so that the workload is evenly

distributed among the robots. Finally, a boustrophedon back and forth movement is generated in a way which minimizes total time to cover a given area [3].

3. Summary

Fig. 1 depicts a cleaning robot in an underground garage, together with a 2D grid map obtained by means of laser scanning. In addition to testing on real world maps, we have performed a statistically significant number of simulations for realistic virtual maps which show that the cleaning time of the proposed method scales as $t \propto N^{-0.964}$, N being the number of robots ($N_{\max}=5$) and, of course, $t \propto N^{-1}$ being the perfect scaling. The real world application is currently being tested by our industrial partner.



Figure 1. The cleaning robot with a 2D static map of a garage to be cleaned.

Acknowledgements

The authors acknowledge the financial support of National Centre for Research and Development, project POIR.01.01.01-00-0206/17 “Designing an autonomous platform which operates in an industrial production environment.”

References

- [1] Galceran E., Carreras E., *A survey on coverage path planning for robotics*, Robotics and Autonomous Systems, Vol. 61, Issue 12, 2013.
- [2] Almadhoun, R., Taha, T., Seneviratne, L. et al. *A survey on multi-robot coverage path planning for model reconstruction and mapping*. SN Applied Sciences 1, 847, 2019.
- [3] Bähmann R. et al., *Revisiting Boustrophedon Coverage Path Planning as a Generalized Traveling Salesman Problem*. In: Ishigami G., Yoshida K. (eds) Field and Service Robotics. Springer Proceedings in Advanced Robotics, vol 16. Springer, Singapore, 2021.

ARM-Z: A hyper-redundant modular inspection manipulator (for extreme environments)

E. Zawidzka¹, W. Kiński², J. Szklarski¹, M. Zawidzki¹

¹ *Institute of Fundamental Technological Research, Polish Academy of Sciences,*

² *Industrial Research Institute for Automation and Measurements PIAP*

Abstract

There are several conditions where autonomous inspection robots (due to roughness of the environment), drones (due to high impact sensitivity and inability to operate in vacuum) or classic inspection manipulators (due to reaching problems) can not be used, or their use is not the most effective.

We propose Arm-Z hyper redundant manipulator coupled with camera head for inspection device in extreme environments such as underwater, or outer space. The advantages of the proposed approach are: the length of manipulator can be adjusted, all modules are congruent the control is insensitive to external conditions. The disadvantages are: the control of Arm-Z is difficult and the maximal length of Arm-Z depends on the given conditions. E.g. application in water or non-gravity environments drastically alleviates the problem of Arm-Z length limitations. This paper discusses the aforementioned issues and presents the preliminary prototype.

1. Introduction

Arm-Z manipulator belongs to a class of hyper-redundant snake-like manipulators. Research on snake robots has been conducted for several decades, especially focusing on mobility. In irregular environments - mountains, trees, water, deserts - bio-inspired snake-like robots in some cases may perform better than the conventional wheeled, tracked and legged forms of robots. Snake locomotion has been studied empirically already in 1940s [1]. 50 years later, the first mathematical model has been developed and snake-like locomotors and manipulators have been proposed in [2]. Today there are many efficient mathematical models of such manipulators and their real-world applications.

Apart from locomotion, snake robots are also present in the field of robotic manipulators (which, using bio-inspired vocabulary, resemble an elephant trunk). The motivation for designing such robots comes from the fact that they can be used in complex environments where using other types of manipulators is impossible. This includes, e.g., medical application with minimally invasive surgery, extreme environment applications: firefighting, urban rescue, disaster relief, and inspection & exploration. Additionally, for example in water, snake-like locomotion in some cases may be more energy efficient than any other approach. It should also be noted that snake-like manipulators often have a relatively large number of degrees of freedom which makes them robust against single module failures. This contrasts with the classic robotic arms with low number of DOFs which are widely used in the industry. For a recent review of snake-like robots, see [3]. Figure 1 locates Arm-Z in the research area.

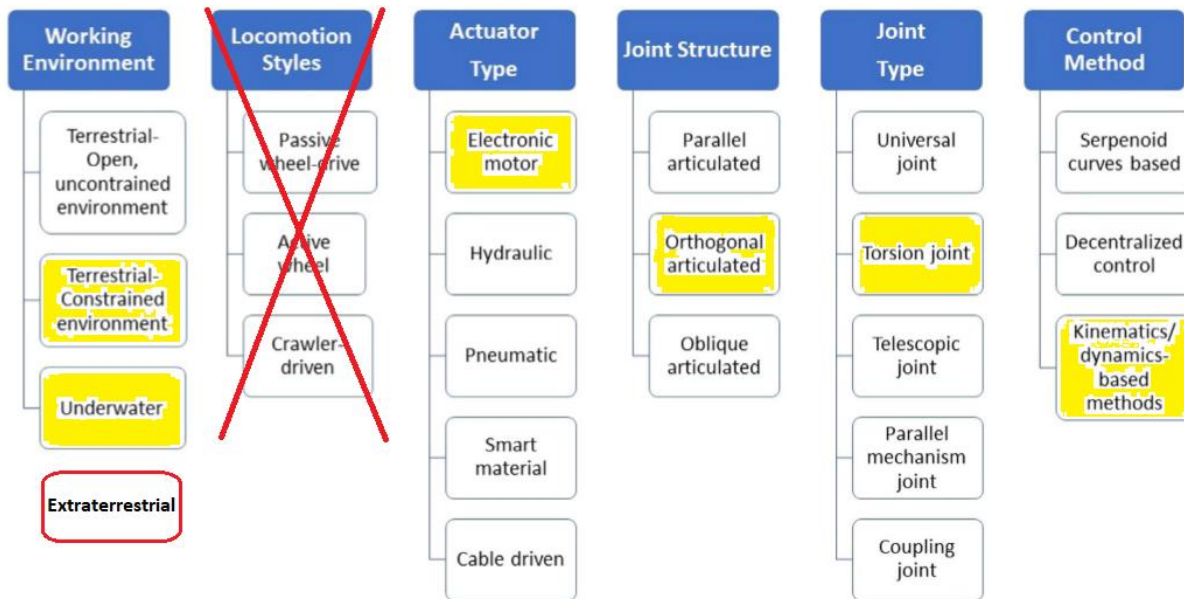


Figure 1. Classification methods of snake robots (figure after [3]). *Arm-Z* belongs to the class of: constrained, various environments, no locomotion, electric motor, orthogonal, torsion joints, kinematic based control manipulators.

Snake hyper-redundant manipulators may be roughly classified into two categories: rigid-backbone robots and continuum-backbone robots. The flexibility of rigid-backbone robots is determined by the number and size of joints. The continuum-backbone robots are made of elastic materials like springs, elastic rods etc. The discussed manipulator is an example of the former.

2. Inspection with snake-like robots

Life extension and maintenance of infrastructure requires routine inspections. Confined and hazardous environments exist in many industries, and new robots are designed to perform inspection and fixing in such places. Remote Access Non-Destructive Evaluation (RANDE) is a testing and analysis technique to evaluate the properties of a component, structure or system for defects without causing damage in spaces with difficult access. For example, the US Air Force air-frames are maintained using the Aircraft Structural Integrity Program (ASIP), where inspection can be done inside wings with snake-like manipulators [4], similar solutions are used by Airbus [5].

The proposed manipulator may be used for purposes of RANDE by equipping it with a proper head. For example, visual inspection tasks would require a camera mounted on a stabilizing gimbal with 2 or 3 DOF.

In order to overcome problems regarding the mechanical stiffness and integrity of the manipulator, applications should be limited to the cases where the number of modules is small (up to 10), or tensions between modules can be reduced. In the latter case, this can be achieved by supporting the or some parts of the infrastructure in which it operates (floor, ground, etc) or operating in an environment like water or cosmic space. Another wide field of applications where stiffness is not a problem, even for a long manipulator, is the field of pipe inspection.

Acknowledgements

This research is a part of the project titled *Arm-Z: an extremely modular hyperredundant low-cost manipulator – development of control methods and efficiency analysis* and funded by OPUS 17 research grant No. 2019/33/B/ST8/02791 supported by the National Science Center, Poland.

References

- [1] **J. Gray**, (1946). *The mechanism of locomotion in snakes*. Journal of experimental biology, 23(2), 101-120.
- [2] **S. Hirose**, (1993). *Biologically inspired robots. Snake-Like Locomotors and Manipulators*, Oxford University Press, Oxford.
- [3] **J. Liu, Y. Tong, J. Liu**, (2021) *Review of snake robots in constrained environments*, Robotics and Autonomous Systems, Volume 141, 103785, ISSN 0921-8890, <https://doi.org/10.1016/j.robot.2021.103785>.
- [4] **M.M. Derriso, C.D. McCurry, C.M. Schubert Kabban**, *A novel approach for implementing structural health monitoring systems for aerospace structures*, Editor(s): Fuh-Gwo Yuan, Structural Health Monitoring (SHM) in Aerospace Structures, Woodhead Publishing, 2016, Pages 33-56, <https://doi.org/10.1016/B978-0-08-100148-6.00002-0>.
- [5] **R. Buckingham et al.**, 2007. *Snake-arm robots: a new approach to aircraft assembly* (No. 2007-01-3870). SAE Technical Paper.

Session 5

**Recent advances in structural design
and topology optimization**

Simultaneous design of topology and printing direction of structural elements for Wire-and-Arc Additive Manufacturing (WAAM)

M. Bruggi ¹, V. Laghi ², M. Palermo ², T. Trombetti ²

¹ *Department of Civil and Environmental Engineering, Politecnico di Milano, 20133 Milano, Italy, matteo.bruggi@polimi.it*

² *Department of Civil, Chemical, Environmental and Materials Engineering, University of Bologna, 40136 Bologna, Italy, vittoria.laghi2@unibo.it, michele.palermo7@unibo.it, tomaso.trombetti@unibo.it*

1. Introduction

Wire-and-Arc Additive Manufacturing (WAAM) is a metal 3D printing technique that allows creating innovative structural shapes [1]. As shown by few experimental investigations, the layer-by-layer manufacturing is responsible for remarkable anisotropy in the elastic response of the WAAM-produced material, see e.g. [2,3]. Topology optimization by distribution of isotropic material is a design tool that is extensively used to sketch lightweight structural components [4]. In this contribution, a suitable topology optimization technique is implemented to generate lightweight structures taking into full account the peculiar anisotropy of the WAAM alloy.

An orthotropic material model is reviewed, as derived from the data of an experimental investigation that was recently performed on printed alloys made with 308LSi stainless steel wire feed. Hence, a displacement-constrained minimum weight optimization procedure is implemented that exploits, as design variables, not only the density field of an orthotropic material phase, but also the orientation of the symmetry axes of such material with respect to a reference frame (i.e., the printing orientation used to manufacture the whole structural element).

The lightweight design of a cantilever beam is attacked to find optimal WAAM solutions that are compared to those achieved by performing topology optimization with isotropic stainless steel. The proposed numerical simulations assess that the printing direction remarkably affects the stiffness of the optimal layouts as well as its topology. Ongoing developments are also introduced to endow the proposed multi-constrained formulation with other structural requirements in the form of additional enforcements.

2. The optimization problem

A material characterization may be performed starting from suitable experimental tests performed on the printed WAAM plates [2,5,6]. The material symmetries of the plates created through the WAAM technique, see Figure 1, suggest the adoption of an orthotropic plane stress model. In the referenced figure, symmetry axes of the material are denoted as \hat{x}_1 and \hat{x}_2 . The former lies along the printing direction, also labelled as the longitudinal direction L, whereas the latter is the transversal direction T.

By testing a dog-bone specimen along L, the relevant Young's modulus E_L and Poisson's ratio ν_{LT} may be derived, whereas E_T and ν_{TL} need for testing along the transversal direction T. Experimental evidence confirms that the following relation holds:

$$E_L \cdot \nu_{TL} = E_T \cdot \nu_{LT}. \quad (1)$$

Hence, by gathering the two-dimensional strain and stress components in vectors (Voigt's notation), the compliance matrix of a WAAM alloy may be written as:

$$\begin{Bmatrix} \varepsilon_L \\ \varepsilon_T \\ \gamma_{LT} \end{Bmatrix} = \begin{bmatrix} 1/E_L & -\nu_{TL}/E_T & 0 \\ -\nu_{LT}/E_L & 1/E_T & 0 \\ 0 & 0 & 1/G_{LT} \end{bmatrix} \begin{Bmatrix} \sigma_L \\ \sigma_T \\ \tau_{LT} \end{Bmatrix}, \quad (2)$$

where:

$$1/G_{LT} = 4/E_D - (1 - \nu_{LT})/E_L - (1 - \nu_{TL})/E_T, \quad (3)$$

being E_D the apparent value of the Young's modulus measured along the diagonal direction D, see [7]. This direction bisects the angle between the longitudinal direction and the transversal one. The average values from the experimental tests read: $E_L = 136\text{MPa}$, $E_T = 106\text{MPa}$, $\nu_{LT} = 0.47$, $\nu_{TL} = 0.37$, whereas the shear modulus $G_{LT} = 151\text{MPa}$. For the conventional Grade 304L isotropic steel, one has $E = 200\text{MPa}$, $\nu = 0.3$.

The design of two-dimensional structural elements for WAAM is herein formulated as a displacement-constrained minimum weight problem by distribution of orthotropic material [8]. A finite element discretization of a given design domain is needed, adopting four-node displacement-based elements and a set of element-wise discrete design variables. In the i -th of the N elements of the mesh, $0 < \rho_i \leq 1$ is the minimization unknown that governs the "density" of the orthotropic material. Additionally, the variable $0 < \theta \leq 180^\circ$, see Figure 1, governs the orientation of the printed layers. It is herein assumed that the printing direction does not change during the fabrication process, that means this variable takes the same value throughout the design domain. It is remarked that θ controls the (anticlockwise) rotation of the axis x_1 of the general reference system with respect to the axis \hat{x}_1 of the material reference system. Assuming that the design domain is framed within the general reference system, the printed direction with respect to the axis x_1 is that given by a (anticlockwise) rotation of this axis as per Figure 1.

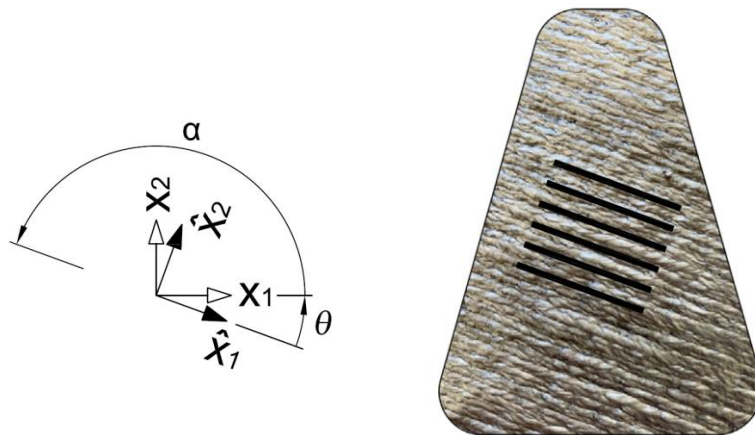


Figure 1. Orientation of the printed layers for an object framed in the general reference system with axes x_1 and x_2 . \hat{x}_1 and \hat{x}_2 are the symmetry axes of the alloy, i.e., the longitudinal direction (L) and the transversal direction (T), respectively.

The conventional Solid Isotropic Material with Penalization (SIMP) [9] is modified to handle the orthotropic allow as follows:

$$\mathbf{C}^{-1}(\rho_i, \theta) = \rho_i^p \mathbf{T}_\sigma(\theta) \widehat{\mathbf{C}}_{w,0}^{-1} \mathbf{T}_\sigma^T(\theta), \quad (4)$$

where $\mathbf{C}(\rho_i, \theta)$ is the compliance matrix of the i -th element in the general reference system, $\widehat{\mathbf{C}}_{w,0}$ is that given in Eqn. (2), \mathbf{T}_σ is a suitable transformation matrix and $p=3$ is a penalization parameter for intermediate values of the density, see [8].

A problem for the simultaneous design of the topology and the printing direction of the WAAM alloy can be stated as:

$$\left\{ \begin{array}{l} \min_{0 < \rho_i \leq 1, 0 < \theta \leq 180^\circ} W = \sum_{i=1}^N \rho_i V_{0,i} \\ \text{subject to } \left(\sum_{i=1}^N \rho_i^p \mathbf{K}_{0,i}(\theta) \right) \mathbf{U} = \mathbf{F} \\ u_a \leq u_{lim} \end{array} \right. \quad (5)$$

In the above statement W is the objective function, i.e., the weight of the overall structure, which depends on the volume of each finite element scaled by the relevant “density” minimization unknown. The first constraint prescribes the discrete equilibrium of the structural element. The global stiffness matrix is found by assembling the element contributions that include the constitutive law given in Eqn. (4). The load vector \mathbf{F} allows computing the nodal displacement vector \mathbf{U} under the effect of a given load. In this contribution an example based on a single point force (vertical load) is considered. The deflection at the load application point u_a is the controlled displacement, whereas u_{lim} is the value of the maximum allowed displacement in that location. The problem is solved using sequential convex programming [10]. The adjoint method is used to compute the sensitivity of the objective function w.r.t. to the minimization unknowns; a standard linear filter is used for the densities to avoid numerical instabilities [9].

3. Design example

A rectangular domain is considered, having width 80cm and height 40cm, as shown in Figure 2. The thickness of the printed lamina is 4mm. The specimen is subjected to a vertical force $F=8.33\text{kN}$ (per mm of thickness of the WAAM-printed plate), which is located at the midpoint of the right side. The left side is fully clamped. The allowed displacement u_{lim} is equal to 4mm.

Figure 3 reports the two mirrored solutions that have been found depending on the initial guess used to start the optimization.

In both cases, the weight at convergence is around 40% (ratio of the black region to the rectangular design domain), against the value 36% that is needed in case of the conventional Grade 304L isotropic steel. A lack of symmetry affects the results involving the WAAM alloy. Indeed, the orientation of the printed material is such that the elastic modulus along any pair of symmetric directions with respect to x_1 (or x_2) takes values that can be very different from each other, see Figure 4.

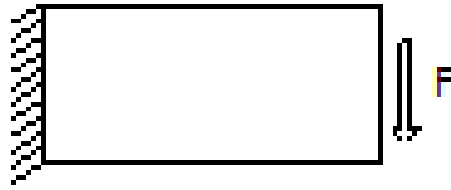


Figure 2. A cantilever beam.

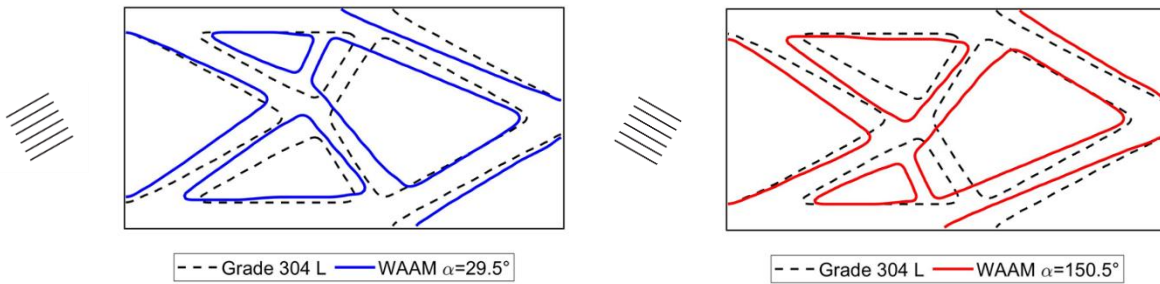


Figure 3. Simultaneous design of the topology and the printing direction for WAAM: optimal results (continuous lines) compared to conventional design with isotropic assumption (dotted line).

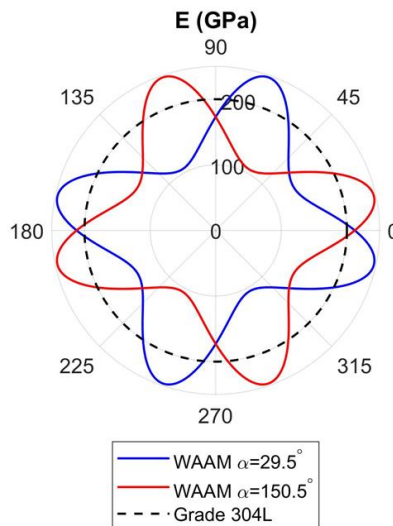


Figure 4. Polar plot of the Young’s modulus of WAAM-produced stainless steel for the two optimal printing directions. The angular coordinate identifies the direction along which the modulus is given with respect to x_1 . The value for Grade 304 stainless steel is reported for comparison.

4. Conclusions

A tool to design structural elements for Wire-and-Arc Additive Manufacturing has been preliminary discussed. At first, an orthotropic material model has been adopted to process data from experimental

tests, thus deriving the compliance tensor of the WAAM alloy in its symmetry axes (the building direction and the transversal one). Hence, a displacement-constrained formulation for the simultaneous design of the topology and of the build direction, which is assumed to remain the same during the whole printing process of the part, has been implemented. The building direction has been embedded in the formulation as an additional degree of freedom with respect to the field of the material density used in standard formulations of topology optimization. A preliminary numerical example has been shown to assess the proposed approach. Optimal layouts have been found in conjunction with non-trivial build directions. The achieved layouts exhibit peculiar features with respect to the conventional result achieved in case of isotropic steel.

Concerning the ongoing developments, the current research is mainly directed towards the handling of three-dimensional models and to the extension of the proposed multi-constrained formulation to meet structural requirements that concern not only serviceability (displacement-based enforcements), but also strength (stress-based enforcements), see e.g. [11].

References

- [1] **C. Buchanan, L. Gardner**, *Metal 3D printing in construction: A review of methods, research, applications, opportunities and challenges*, *Engineering Structures*, **180**, 2019.
- [2] **V. Laghi, M. Palermo, G. Gasparini, G. V.A. Girelli, T. Trombetti**, *Experimental results for structural design of wire-and-arc additive manufactured stainless steel members*, *Journal of Constructional Steel Research*, **167**, 2020.
- [3] **C. V. Haden, G. Zeng, F. M. Carter, C. Ruhl, B. A. Krick, D. G. Harlow**, *Wire and arc additive manufactured steel: Tensile and wear properties*. *Additive Manufacturing*, **16**, 115-123, 2017.
- [4] **M. P. Bendsøe, N. Kikuchi**, *Generating optimal topologies in structural design using a homogenization method*. *Computer Methods in Applied Mechanics and Engineering*, **71**(2), 197-224, 1988.
- [5] **V. Laghi, M. Palermo, G. Gasparini, M. Veljkovic, T. Trombetti**, *Assessment of design mechanical parameters and partial safety factors for wire-and-arc additive manufactured stainless steel*, *Engineering Structures*, **225**, 2020.
- [6] **V. Laghi, M. Palermo, G. Gasparini, G. Ceschini, T. Trombetti**, *Tensile properties and microstructural features of 304L austenitic stainless steel produced by wire-and-arc additive manufacturing*, *International Journal of Advanced Manufacturing Technology*, **106**(9-10), 3693-3705, 2020.
- [7] **V. Laghi, L. Tonelli, M. Palermo, M. Bruggi, R. Sola, T. Trombetti**, *Experimentally-validated orthotropic elastic model for wire-and-arc additively manufactured stainless steel*, *Additive Manufacturing*, **42**, 2021.
- [8] **M. Bruggi, V. Laghi, V., T. Trombetti**, *Simultaneous design of the topology and the build orientation of wire-and-arc additively manufactured structural elements*, *Computers and Structures*, **242**, 2021.
- [9] **M. P. Bendsøe, O. Sigmund**, *Topology Optimization: Theory, Methods and Applications*, Springer, 2003.
- [10] **K. Svanberg**, *The method of moving asymptotes-a new method for structural optimization*, *International Journal for Numerical Methods in Engineering*, **24**(2), 359-373, 1987.
- [11] **B. Blachowski, P. Tuzowski, J. Lógó**, *Yield limited optimal topology design of elastoplastic structures*, *Structural and Multidisciplinary Optimization*, **61**(5), 1953-1976, 2020.

Optimal Elastic-Plastic Analysis of Reinforced Concrete Structures with Limited Residual Strain Energy Capacity

M. Movahedi Rad ¹, S. Khaleel Ibrahim ², J. Lógó ³

¹ Department of Structural and Geotechnical Engineering, Széchenyi István University, H-9026 Győr, Hungary, majidmr@sze.hu

² Department of Structural and Geotechnical Engineering, Széchenyi István University, H-9026 Győr, Hungary, sarahibrahim8391@gmail.com

³ Department of Structural Mechanics, Department of Highway and Railway Engineering, Budapest University of Technology and Economics, H-1111, Budapest, Hungary, logo.janos@emk.bme.hu

1. Introduction

One of the most successful applications of the variational formulation in the incremental plasticity theory is the theory of limit analysis. The basic ideas of the principles of limit analysis were first recognized and applied to the steel beams by Kazinczy [1]. The fundamental problem of limit analysis is to determine the plastic limit load multiplier and the stresses, strain rates and velocities at the plastic limit state of the body. However, at the application of the plastic analysis and design methods the control of the plastic behaviour of the structures is an important requirement. Since the limit analysis provides no information about the magnitude of the plastic deformations and residual displacements accumulated before the adaptation of the structure, therefore for their determination several bounding theorems and approximate methods have been proposed. Among others Kaliszky and Lógó [2] suggested that the complementary strain energy of the residual forces could be considered an overall measure of the plastic performance of structures and the plastic deformations should be controlled by introducing a bound for magnitude of this energy.

In this research, optimal elastic-plastic analysis and design methods of reinforced concrete (RC) structures are presented using limited plastic deformation. First, a concrete plastic damage (CPD) constitutive model is developed and applied to calibrate a numerical model. Then, different objective functions were considered to optimize the volume of the steel used to reinforce the structures and plastic loading. The plastic deformations are controlled by using constraints on the complementary strain energy of the residual internal forces of the steel bars. Applying different optimization problems showed that the complementary strain energy of the residual forces has a significant effect and can be considered as a constraint on the plastic behavior of the RC structures.

2. Methods

Let us assume that the steel bar elements has been defined by the concept of elastic-plastic analysis and design methods. Therefore by applying load P_0 plastic forces Q^p will appear in the structure. When the load is reduced under unloading elastic deformations occur and then the elastic internal forces $-Q^e$ will take place in the structure. Accordingly after unloading the residual internal forces remain in the structure.

$$Q^r = Q^p - Q^e \quad (1)$$

Where

$$Q^e = F^{-1}GK^{-1}P_0 \quad (2)$$

here K is the stiffness matrix; F is the flexibility matrix and G denotes the geometrical matrix. Therefore the complementary strain energy for positive-definite function, can be determined from the residual forces.

$$C_r = \frac{1}{2} \sum_{i=1}^n \frac{1}{S_i} \int_0^{l_i} (Q_i^p(s) - Q_i^e(s))^2 ds \geq 0 \quad (3)$$

here $Q_i^p(s)$ and $Q_i^e(s)$ are the functions of plastic and elastic internal forces; S_i expresses tensile stiffnesses for truss elements respectively.

A proper computational method proposed that the complementary strain energy of the internal residual forces could be defined as a general measure of the plastic performance of the structures and the residual deformations are constrained by introducing a limit for the value of this energy:

$$\frac{1}{2} \sum_{i=1}^n \frac{1}{S_i} \int_0^{l_i} (Q_i^p(s) - Q_i^e(s))^2 ds - C_{r0} \leq 0 \quad (4)$$

where C_{r0} is an allowable strain energy value for C_r .

For steel bar elements the complementary strain energy of the residual forces can be considered as follow:

$$C_p = \frac{1}{2E} \sum_{k=1}^n \frac{l_k}{A_k} (S_k^r)^2 \quad (3)$$

Here A_k is the cross-section area the bar elements l_k , ($k = 1, 2, \dots, n$) denotes the length of the bars, S_k^r : the residual normal force of the bar members, E : the Young's modulus.

3. Conclusion

In this study elastic-plastic analysis of RC structures with limited plastic displacements introduced. For this goal plastic limit theorem is developed and applied to the structures. Additionally to control the plastic behavior of the structure the complementary strain energy of the residual forces are constrained. A concrete plastic damage (CPD) constitutive model is applied to calibrate a numerical model, then different nonlinear optimization problems were carried out concerning the reinforcement steel volume ratio and plastic loading. The numerical results shows that the bound of the complementary strain energy of the residual forces can influence significantly the magnitude of the limit load multiplier.

References

- [1] **G. Kazinczy.** (1914). *Experiments with Clamped Beams*. *Betonszemle* 2, No. 4,5,6 , 68-71, 83-87, 101-104.
- [2] **S. Kaliszky, J. Lógó.** (1997). *Optimal Plastic Limit and Shakedown Design of Bar Structures with Constraints on Plastic Deformation*, *Engineering Structures*, 19 (1), pp. 19-27.

Multiscale Optimal Design of Grid Systems for High-rise Buildings

Hussein Ismail^{1,2}, Matteo Bruggi² and János Lógó¹

¹ Dept. of Structural Mechanics, Budapest University of Technology and Economics, Hungary,

* Corresponding author: logo@ep-mech.me.bme.hu

² Dept. of Civil and Environmental Engineering, Politecnico di Milano, Milano, Italy,

Introduction

Topology optimization is an appropriate tool to design bracing systems for high-rise buildings [1]. Diagrids and hexagrids are truss structures that employ inclined members instead of vertical columns to carry both vertical and lateral loading. As it is well-known, perimetral grids are an effective way to deal with horizontal forces in tall buildings. Diagrids consist of members that diagonally intersect to generate triangular shapes; hexagrids were inspired by honeycombs, where hexagonal patterns constitute the resisting bulk. Mechanical properties of such kind of grids were extensively investigated and critically review both in the scientific and technical literature [2]. Their optimization is generally performed by using size optimization [1] or homogenization in conjunction with a cantilever beam model of the high-rise building [3].

This paper addresses the optimal design of grid systems in high-rise buildings by means of topology optimization and multiscale analysis of periodic solids. Instead of adopting a multiscale beam model, a 3D box-shaped finite element mesh is used as a discrete design domain to seek for optimal grids whose panels can be regarded as lattice structures. Among the others, [4] computes analytical expressions for the constitutive tensors that describe the elastic behavior of triangular and hexagonal lattices at the macroscopic level (the high-rise building). Such expressions depend on the prescribed reference dimension, cross-section, and material used at the mesoscopic level (the cell).

Optimization Problem

Along the lines of [5] and [6], a multi-material topology optimization problem is used that employs continuous variables to distribute a discrete set of lattices.

Two types of micro-structure are considered for lattices. One can see in Figure 1(left) an isotropic triangular lattice of a diagrid while in Figure 1(right) the isotropic hexagonal lattice of a hexagrid is presented. The triangular and honeycomb lattices have a six-fold rotational symmetry, so that isotropic constitutive relations are found by means of the multiscale procedure. The constitutive matrices at the macro-scale are:

$$C_d = \frac{3E}{4\sqrt{3}L^3} \begin{bmatrix} 3(AL^2 + 4I) & AL^2 - 12I & 0 \\ AL^2 - 12I & 3(AL^2 + 4I) & 0 \\ 0 & 0 & AL^2 + 12I \end{bmatrix} \quad (1)$$

and

$$C_h = \frac{EA}{2\sqrt{3}L(AL^2 + 12I)} \begin{bmatrix} AL^2 + 36I & AL^2 - 12I & 0 \\ AL^2 - 12I & AL^2 + 36I & 0 \\ 0 & 0 & 24I \end{bmatrix} \quad (2)$$

for each type of lattice. Here C_d is the constitutive matrix for diagrids while C_h represents the hexagrid.

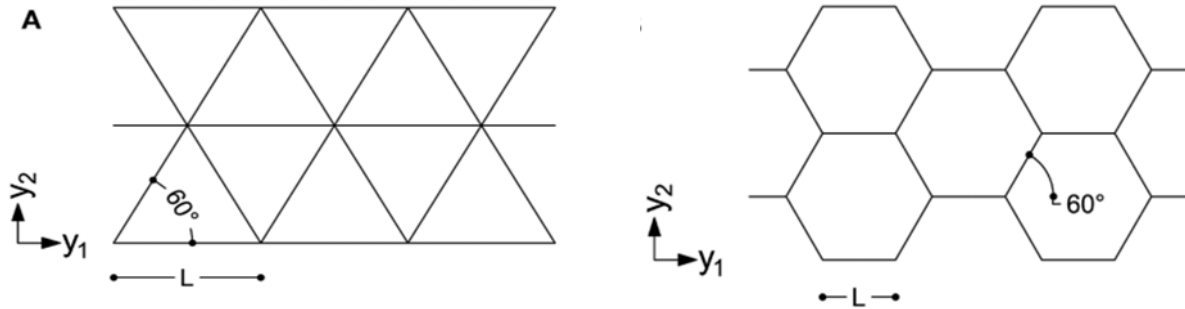


Figure 1. An isotropic triangular lattice of a diagrid (left), and the isotropic hexagonal lattice of a hexagrid (right).

Each phase stands for a candidate lattice that has given features in terms of constituent elements and geometrical properties. Diagrids and hexagrids with given reference length L are assumed to be made of elements whose cross-section should be selected within a prescribed set, meaning that the available area A and moment of inertia I have discrete values. A continuous interpolation of the macroscopic stiffness matrix is adopted following an original extension of the SIMP ([5, 6]).

$$C = \rho_0^p \left((1 - \rho_1^p) C_1 + \sum_{i=2}^{m-1} (1 - \rho_i^p) C_i \prod_{j=1}^{i-1} \rho_j^p + C_m \prod_{j=2}^m \rho_{j-1}^p \right) \quad (3)$$

Here in the next, there is no void phase. It is assumed that the whole building envelope is endowed with a structural grid having varying cross-section and shape. A basic lattice that adopts the smallest among the candidate cross-sections provides a minimum stiffness all over the design domain. The goal of the optimization is distributing local increments of the macroscopic stiffness matrix to meet design requirements.

$$C = C_0 + \rho_1^p \left((1 - \rho_2^p) (C_1 - C_0) + \sum_{i=2}^{m-1} (1 - \rho_{i+1}^p) (C_i - C_0) \prod_{j=1}^{i-1} \rho_{j+1}^p + (C_m - C_0) \prod_{j=2}^m \rho_j^p \right) \quad (4)$$

The above equation handles $m+1$ cross-sections. C_0 is the macroscopic stiffness matrix: (the weakest among the available ones). C_i refers to the i -th cross-section other than the basic one.

Having the aim of using few different sections in the grid the design is straightforward. Here for sake of simplicity, the assumption $m = 3$ will be used to perform numerical simulations. Writing out the expression in Eq. (4) to handle four cross-sections one has:

$$C = C_0 + \rho_1^p \left((1 - \rho_2^p) (C_1 - C_0) + \rho_2^p (1 - \rho_3^p) (C_2 - C_0) + \rho_2^p \rho_3^p (C_3 - C_0) \right) \quad (5)$$

Eq.5 is very efficient in penalizing the weights of the stiffness increments, i.e., the optimal values of the continuous variables ρ , towards the bounds 0 and 1.

The stated problem searches for the distribution of cross-sections and shapes that minimizes the weight of the grid under enforcements on the stiffness of the building for lateral loads (displacement constraints at the top of the building).

$$\left\{ \begin{array}{l} \min_{0 \leq x_{p,1}, \dots, x_{e,m} \leq 1} \mathcal{W} = \sum_{e=1}^{nel} W_e \quad (a) \\ s. t. \left(\sum_{e=1}^{nel} K_e(x_{e,1}, \dots, x_{e,m}) \right) U_1 = F_1 \quad (b) \\ \left(\sum_{e=1}^{nel} K_e(x_{e,1}, \dots, x_{e,m}) \right) U_2 = F_2 \quad (c) \\ u_1 \leq u_{lim} \quad (d) \\ u_2 \leq u_{lim} \quad (e) \end{array} \right. \quad (6)$$

Considering a problem with four candidate cross-sections, the weight of the bars that fall within the e- the finite element reads:

$$W_e = W_{e,0} + x_{e,1}[(1 - x_{e,2})(W_{e,1} - W_{e,0}) + x_{e,2}(1 - x_{e,3})(W_{e,2} - W_{e,0}) + x_{e,2}x_{e,3}(W_{e,2} - W_{e,0})] \quad (7)$$

In order to improve manufacturability of the achieved layouts, patches are introduced to force the distribution of the same lattice at a given height or within a minimum contiguous area. This also helps in reducing the number of optimization variables used in the optimization.

Numerical Example

A tall building with square plan (side 48 m) is considered. The height of the building is 207.85 m; a uniform distribution of the horizontal load is assumed along the height of the building with intensity 96 kN/m, acting along the two axes of the plan.

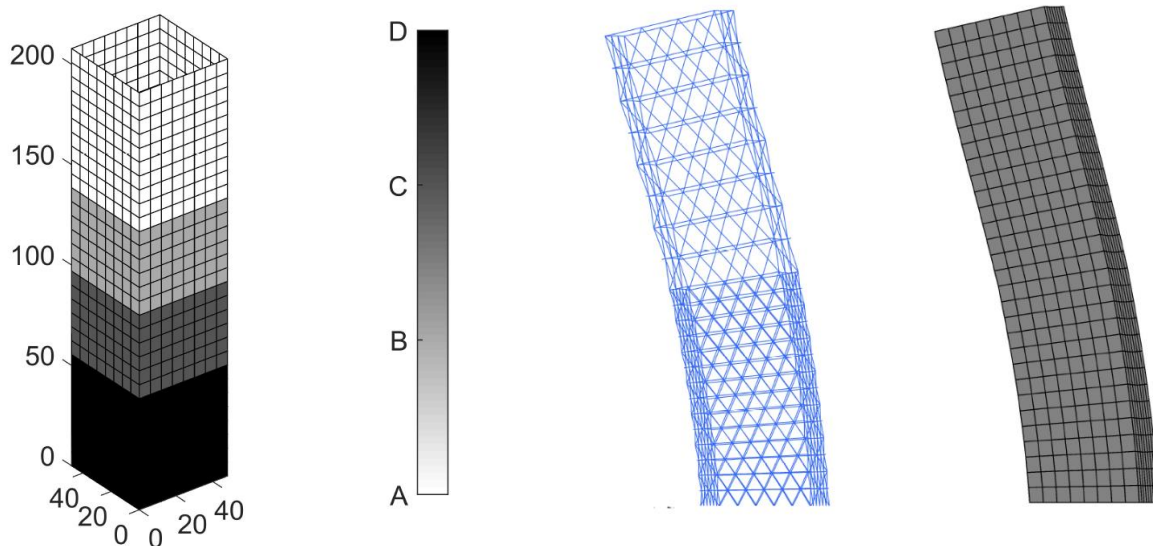


Figure 2. A diagrid with varying cross-sections and varying reference dimensions for a tall building with square plan: optimal solution (left); magnified deformed shapes: beam model vs multiscale method (right).

The proposed approach can be used to distribute different skin layouts within the same structural envelope. Two diagrids with reference length $L = 16\text{m}$ and $L = 8\text{m}$ are considered, defining four candidate equivalent stiffness tensors. The diagrid with reference length $L = 16\text{m}$ is made of tubes with circular hollow

cross-sections with diameter 558 mm and thickness 12.5mm or 16mm, named diagrid type A and B, respectively; the diagrid with reference length $L = 8\text{m}$ consists of tubes having the same cross-section type and equal external diameter but thickness 16mm or 20mm, labelled type C and D respectively. The optimal distribution of lattice structures is sketched in Figure 2. A comparison in terms of (magnified) deformed shapes is presented as well, comparing a beam model and the multiscale one. It is pointed out that the horizontal displacements computed at the top of the grids are in very good agreement. With respect to the achieved optimal solution, the provided stiffness decreases along the height of the building, as expected.

Conclusion

The conceptual design of grid systems in high-rise buildings has been addressed by combining optimization and multiscale analysis of lattice structures. Macroscopic properties of grids with given cross-section have been retrieved from the literature. Hence, a multi-material optimization problem has been formulated to find the distribution of a prescribed discrete set of candidate cross-sections and shapes such that the structural weight of the grid is minimized under constraints on the lateral displacements of the building. Numerical results have been presented to assess the proposed approach. Current directions of research include testing on more complex geometry of the envelope according to [7].

Acknowledgements

This study was supported by the NKFI (grant K 138615) and the joint grant of the Hungarian Academy of Sciences and the Polish Academy of Sciences.

References

- [1] **Lauren L. Stromberg, Alessandro Beghini, William F. Baker, Glaucio H. Paulino**, (2012). *Topology optimization for braced frames: Combining continuum and beam/column elements*, Engineering Structures, 37, 106-124. <https://doi.org/10.1016/j.engstruct.2011.12.034>.
- [2] **Moon, K., Connor, J. J., and Fernandez, J. E.**, (2007). *Diagrid structural systems for tall buildings: Characteristics and methodology for preliminary design*. Struct Des. Tall Spec. Build. 16, 205–230. doi: 10.1002/tal.311
- [3] **Montuori, G. M., Mele, E., Brandonisio, G., and De Luca, A.**, (2014). *Geometrical patterns for diagrid buildings: exploring alternative design strategies from the structural point of view*. Eng. Struct. 71, 112–127. doi: 10.1016/j.engstruct.2014.04.017
- [4] **Vigliotti, A., and Pasini, D.**, (2012), *Linear multiscale analysis and finite element validation of stretching and bending dominated lattice materials*. Mech. Mater. 46, 57–68. doi: 10.1016/j.mechmat.2011.11.009
- [5] **Gibiansky, L. V., and Sigmund, O.**, (2000), *Multiphase composites with extremal bulk modulus*. J. Mech. Phys. Solids 48, 461–498. doi: 10.1016/S0022-5096(99)00043-5
- [6] **Stegmann, J., and Lund, E.**, (2005), *Discrete material optimization of general composite shell structures*. Int. J. Numer. Methods Eng. 62, 2009–2027. doi: 10.1002/nme.1259
- [7] **M. Bruggi**, (2020). *Conceptual design of diagrids and hexagrids by distribution of lattice structures*. Frontiers in Built Environment. 6. doi:10.3389/fbuil.2020.00080

Optimization of A Steel Structure Taking Into Account The Randomness Of Design Parameters

P. Zabojszcza ¹, U. Radoń ², P. Tazowski ³

¹ *Kielce University of Technology, Faculty of Civil Engineering and Architecture, Kielce , Poland*

² *Kielce University of Technology, Faculty of Civil Engineering and Architecture, Kielce , Poland*

³ *Institute of Fundamental Technological Research Polish Academy of Sciences, Department of Information and Computational Science, Warsaw, Poland*

1. Introduction

The subject of the considerations are shallow lattice structures susceptible to global loss of stability by node snap through (Marcinowski [1], Waszczyszyn i in. [2], Thompson, Hunt [3]). In structures of this type, large displacement gradients may appear, therefore, when designing these covering, geometrically nonlinear relationships should be used. In the era of the more and more common trend of optimal design, an extremely important problem is to take into account the impact of the random nature of the parameters describing the structure. This work is an attempt to draw attention to this important aspect of the optimal dimensioning of bar structures using the formalism of the so-called robust optimization.

The problem of optimal design of ever larger and more complex structures forces engineers to minimize the cost of execution and the weight of the structure. Optimization methods are therefore becoming an indispensable tool in rational design. Thanks to them, it is possible to properly select material properties or dimensions of the structure, which is often a very labor-intensive task.

2. Optimization

It is worth noting that optimal structures are very sensitive to the random dispersion of model parameters and external interactions. Solutions that fulfill their function for nominal values may turn out to be unacceptable after taking into account the randomness of the parameters. Therefore, it seems natural to extend the formulation of deterministic optimization, which takes into account the random dispersion of parameter values. This formulation offers robust optimization. This term refers to the widely understood methodology of designing both structures, devices and production processes, in which, while maintaining the high functionality of the designed systems, the aim is to find a solution that is as resistant to changes in its parameters as possible. The solution obtained in the process of robust optimization is definitely less sensitive to the parameters of the model that are difficult to control or external influences. The advantages of this method include the fact that it leads to a solution that maintains quality and functionality in a wide range of working conditions. (Stocki [4], Gondzio et al. [5]). In rational design, it is necessary to strive to ensure the highest possible level of resistance of the structure to changes in the designed variables. Robust optimization can also be effectively used in the design of building structures. The methods known as 'robust' optimization are not, however, a frequent choice of designers in this field. Effective use of the random nature of parameters requires the improvement of the methods of stochastic analysis and work on engineering software enabling its application.

3. Single layer steel dome analysis

The example shows the analysis of a shallow single-layer steel structure, modeled with truss elements on pinned support. A force of $P = 5\text{ kN}$ was applied to the structure in each node. The bars were designed from S235 steel with the yield point $f_y = 235\text{ MPa}$, Young's modulus $E = 210\text{ GPa}$ and Poisson's ratio $\nu = 0.3$. The geometry and deformation of the considered structure is shown in Figure 1.

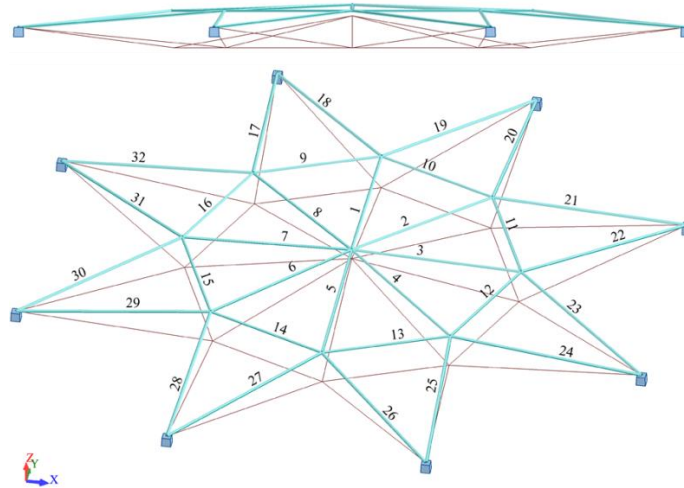


Figure 1. Geometry and deformation of the structure

On the basis of the static and strength analysis, the following cross-sections were assumed for individual groups of bars: RO54x3.6 for the Meridian_1 (bars 1 to 8), RO60.3x6.3 for Meridian_2 (bars 17 to 32) and RO 51x6.3 for the Ring (bars 9 to 16). The maximum effort of bars in the distinguished groups was verified, which amounted to 66%, 72% and 71%, respectively. The maximum vertical displacement was recorded at nodes 2 to 9 and was 13.62mm, while the limit value of vertical displacement according to Eurocode3 [6] is 46.67mm.

Then the structure was subjected to linear buckling analysis. The value of the critical load multiplier was $\alpha_{cr} = 1.714$. Such a low value indicates the need to perform calculations that take into account geometric non-linearity.

The geometrically nonlinear analysis showed that the critical load multiplier was $\mu_{cr} = 1.184$, while the limit displacement was 18.41mm. The effort of the bars was verified when the structure was loaded with the force $P = 5.92\text{ kN}$, which was 71% for the Meridian_1, 90% for the Meridian_2 and 96% for the Ring. The maximum stresses in the bars did not exceed 62 MPa.

Reliability analysis.

The structure reliability was analyzed using the FORM method (Engelstad, Reddy [7]) when the structure was loaded with the force $P = 0.98 \cdot 5\text{ kN} = 4.90\text{ kN}$. The cross-sectional area of successive groups of bars A_i was assumed as random variables. The description of random variables is presented in Table 1. Variables are not correlated. The mass of the modeled structure is $M = 813.51\text{ kg}$. For the above case, the value of the coefficient of variation was set at 5%.

Table 1. Description of random variables

Random Variables Xi	Mean Values [cm ²]	Standard deviations [cm ²]	Coefficient of variation [%]
A1	5.7	0.285	5
A2	10.7	0.535	5
A3	8.85	0.443	5

On the basis of the analyzes, the maximum value of the node displacement was limited at $w_{\max} = 1.6$ cm. For such a limit value, the limit function takes the form:

$$f_s = 1 - \frac{w(\mathbf{x})}{w_{\max}} = 1 - \frac{w(\mathbf{x})}{1.600} \quad (1)$$

where: $w(\mathbf{x})$ - displacement in a given calculation step, w_{\max} - assumed maximum displacement.

The determined value of the reliability index was $\beta = 2.011$, while the failure probability was $p_f = 0.022$. The determined values of the elasticity index in relation to the mean value are as follows: for the random variable A1: 0.047, for random variable A2: 0.683 and for random variable A3: 0.729.

There is a significant difference in the values of the elasticity index in relation to the mean value of variable A1 in relation to the elasticity indexes of the other variables. Therefore, it is worth verifying the influence of variable A1 on the reliability of the structure by re-performing the reliability analysis, taking it into account as a deterministic value. If only two random variables (A2 and A3) were taken into account, the value of the reliability index was $\beta = 1.996$, while the failure probability was $p_f = 0.023$. The difference in the value of the reliability index is 0.015. On this basis, for further calculations, we can accept two design random variables: A2 and A3.

Deterministic optimization

In the second part, we are looking for the optimal dimensions of the cross-sections of individual groups of bars: for the Meridian_2: A2 and for the Ring: A3 using the deterministic optimization algorithm (Błachowski et al. [8]).

The objective function will be the mass of the structure:

$$f_C = \text{minimum} \left(\rho \cdot \left(\sum_{j=17}^{32} L_j \cdot A2 + \sum_{k=9}^{16} L_k \cdot A3 \right) \right) = \text{min}(\text{Mass}) \quad (2)$$

where: L_j - length of the j -th rod from the Meridian_2 group, L_k - length of the k -th rod from the Ring group.

Simple constraints are described in Table 2. They represent the upper and lower limits of the searched design variables.

Table 2. Description of simple constraints

Design variable	Lower boundary [cm]	Upper boundary [cm]
A1	9.844	11.556
A2	8.142	9.558

For the case under consideration, 8% tolerance of the cross-sectional area was assumed.

The inequality constraint was formulated as the condition of not exceeding the permissible vertical displacement of the node, for $w_{\max} = 1.6$ cm:

$$g(\mathbf{x}) = w(\mathbf{x}) - w_{\max} = w(\mathbf{x}) - 1.600 < 0 \quad (3) \quad \begin{array}{l} \text{The} \\ \text{deter} \end{array}$$

ministic optimization was carried out using the simplex method of Nelder Mead with the maximum number of iterations $N = 1000$ and the convergence parameter $\varepsilon = 1.0 \text{ E-}08$.

The obtained dimensions of the cross-section are: $A_1=9.845\text{cm}^2$, $A_2=8.331\text{cm}^2$. The limit function value for this case was 761.706 kg. The probability of failure and the reliability index were also verified, which in this case was respectively: $p_f = 0.5$, while $\beta = 0.0$.

Robust optimization

In the case of robust optimization, random and design variables (μ_{A_2} , μ_{A_3}), the objective function and constraints were defined. The objective function is, as in the case of deterministic optimization, the mass of the structure, but assuming that it takes into account the weighting factor γ that determines the significance of each of the criteria (mean value and standard deviation). The value of the coefficient of variation was set at 5%.

For the case under consideration, the task of robust optimization takes the form:

1. Find the values of the variables: μ_{A_2} , μ_{A_3}
2. Minimizing: $f_C = \frac{1-\gamma}{\eta^*} [\text{Mass}] + \frac{\gamma}{\sigma^*} \sigma[\text{Mass}]$
3. With constraints:

$$E[w(\mathbf{x}) - 1.600] - \tilde{\beta} \cdot \sigma[w(\mathbf{x}) - 1.600] \geq 0$$

$$9.844 \leq \mu_{A_2} \leq 11.556$$

$$8.142 \leq \mu_{A_3} \leq 9.558$$

where: $\gamma \in [0, 1]$ - determines the meaning of each of the criteria, η^* , σ^* - normalizing constants, $w(\mathbf{x}) - 1.600$ - limitation of the permissible vertical displacement.

In order to confirm the correctness of the performed calculations, two methods of building the response surface were used: kriging (Simpson et al. [8]) and the second-order method (Box, Wilson [9]). The following parameters were assumed: $\gamma=0.5$, $\tilde{\beta}=2.0$.

Response surfaces are built using the kriging and second order method, while the experiments are generated according to the plan of optimal Latin hypercubes (Liefvendahl, Stocki [10]). After the robust optimization, the obtained values of the design variables and a mass of the structure are summarized in Table 3.

Table 3. The values of the random variables and a mass of the structure obtained in the robust optimization

	Kriging	Second order method
A2	9.926 cm ²	9.924 cm ²
A3	9.558 cm ²	9.558 cm ²
Mass	786.401 kg	786.309 kg

As a result of robust optimization, an increase in the values of the cross-sectional areas of individual bar groups and the weight of the structure was obtained. However, this results in a significant improvement in

the safety of the structure, which is indicated by the values of the reliability index and the probability of failure, which in this case are respectively: for kriging: $\beta = 2.038$ and $p_f = 0.021$, for second order method: $\beta = 2.036$ and $p_f = 0.021$.

Summary

The results of both analyzes show a clear influence of the selection of the optimization method on the obtained values. The result of robust optimization is a structure resistant to random variable deviations. In analysis, it can be observed that the structure optimized by the robust method is lighter than the original structure by more than 27 kg, while the reliability index indicates its reinforcement.

References

- [1] **J. Marcinowski**, *Stateczność konstrukcji sprężystych: struktury prętowe, łuki, powłoki*, Dolnośląskie Wydawnictwo Edukacyjne, 2017,
- [2] **Z. Waszczyszyn, Cz. Cichoń, M. Radwańska**, *Stability of Structures by Finite Element Methods*, Elsevier, 1994,
- [3] **J.M.T. Thompson, G.W. Hunt**, *A general theory of elastic stability*, Wiley and Sons, 1973,
- [4] **R. Stocki**, *Analiza niezawodności i optymalizacja odpornościowa złożonych konstrukcji i procesów technologicznych*, IPPT PAN, Warszawa, 2010,
- [5] **J. Gondzio, P. Munari, A. Moreno, J. De La Vega, D. Alem, R. Morabito**, (2018), *The robust vehicle routing problem with time windows: compact formulation and branch-price-and-cut method*, Technical Report 002/2018, Operations Research Group, Production Engineering Department, Federal University of São Carlos, Brazil,
- [6] **PN-EN 1993-1-1. Eurocode 3**: Design of steel structures. Part 1-1: General rules and rules for buildings.
- [7] **S.P. Engelstad, J.N. Reddy**, (1993), *Probabilistic nonlinear finite element analysis of composite structures*, AIAA Journal, Vol. 31, Issue 2, pp. 1362-1369,
- [8] **B. Błachowski, P. Tuzowski, J. Logo**, (2020), *Yield limited optimal topology design of elastoplastic structures*, Structural and Multidisciplinary Optimization, Vol. 61, p. 1953–1976,
- [9] **T.W. Simpson, T.M. Mauery, J.J. Korte, F. Mistree**, *Kriging metamodels for global approximation in simulation-based multidisciplinary design optimization*, AIAA Journal, 39(12): pp. 2233–2241, 2001,
- [10] **G.E.P. Box, K.B. Wilson**, (1951), *On the Experimental Attainment of Optimum Conditions (with discussion)*, Journal of the Royal Statistical Society Series B 13, str. 1–45,
- [11] **M. Liefvendahl, R. Stocki**, (2006), *A study on algorithms for optimization of Latin hypercubes*, Journal of Statistical Planning and Inference, 136(9): pp. 3231–3247,

Topology optimization of large-scale arch systems

G. Dzierżanowski

Warsaw University of Technology, Faculty of Civil Engineering, gd@il.pw.edu.pl

1. Introduction

The topology optimization problem for arch systems (archgrids) was first put forward by G.I.N. Rozvany and W. Prager in [6] and further studied in e.g. [7, 8, 9]. The Authors discussed the optimality conditions for a structure composed of plane arches, pinned at the boundary Γ of a given plane region Ω , and transmitting to that boundary a load of given intensity $q(x, y)$, where $(x, y) \in \Omega$. Such an arch system is best visualized as a ribbed vault (arch-like roof) spanning Ω . The optimization problem is to create a structure whose weight is minimum possible, while assuming that: *i*) stresses in the entire system are only compressional; *ii*) axes of all arches belong to the same surface $f = f(x, y)$, referred to as the archgrid elevation function; *iii*) each single axis belongs to a plane perpendicular to region Ω . Arches in the vault form of a dense grid of curved bars carrying the load independently of one another. Therefore, the mechanics of a Rozvany-Prager archgrid is that of a gridwork shell and not a shell continuum.

Optimality conditions for Rozvany-Prager arch systems are compatible with those for Michell frames but with univalent – in our case compressional – stresses. Consequently, we say that optimal arch system is at the verge of a plastic failure, with each single arch uniformly compressed to the limit value, say $\sigma_c > 0$. This, in turn, involves an implicit requirement that members of optimally designed archgrid are bending- and shear-free. In other words, external load is carried by arches subjected to axial stress resultants only. Despite obvious similarities between the two theories, accommodating the Rozvany-Prager approach in computational algorithms for Michell structures is not straightforward. Loosely speaking, the main difficulty is in redefining the optimality conditions from point-wise (Michell) to arch-wise (Rozvany-Prager).

2. Computational procedure for archgrid optimization

Modern approach to archgrid optimization problem, see [2, 3, 4, 5], involves mathematical techniques of calculus of variations, thus paving way for numerical procedures in the continuous and discrete settings. In this note, we follow the latter. Numerics of the discrete approach to Rozvany-Prager archgrids is considered from the perspective based on Second-Order Cone Programming (SOCP), see [1] for theoretical introduction to this method. Procedures used for solving the examples are coded in MATLAB combined with MOSEK optimization toolbox for SOCP routines. Computational algorithm used in this outlook proves to be very efficient in terms of CPU-time. It allows for analyzing the structures with a very large ($\sim 10^6$) number of arches. Results obtained for such extremely populated archgrids clearly exceed the rational needs of civil engineering industry, but they may well serve to hint the research aimed at benchmark solutions to optimization problems. Numerical simulations for this note were performed on a laptop computer equipped with the Intel Core i7-4600U CPU @ 2.10 GHz (2 processors), 8 GB RAM, 64-bit Windows 10 Pro, MathWorks MATLAB R2021a and MOSEK optimization toolbox version 9.2.

It turns out, that the minimum volume, V_{min} , of a vault is proportional to $\sup \langle q; f \rangle$, with “sup” operation taken over all functions $f = f(x, y)$ satisfying the kinematic constraints imposed in the theory of

Rozvany and Prager. Technically, these constraints are: *i) $f = 0$ at Γ , and *ii) $s_K = \nabla f \cdot \mathbf{e}_K$ ($K = 1, \dots, k$). Here \mathbf{e}_K stands for the direction of the axis x_K orienting the K -th arch with respect to the coordinate system $(x, y) \in \Omega$, see Fig. 1, and k denotes the total number of arches in the archgrid. More precisely, the K -th arch is considered optimal if the Euclidean norm of the slope function s_K satisfies**

$$\|s_K\|_2 = \sqrt{L_K}, \quad \|s_K\|_2 = \left(\int_0^{L_K} (s_K(x_K))^2 dx_K \right)^{\frac{1}{2}}, \tag{1}$$

where L_K is the length of the K -th arch chord. The requirement in (1) is known in the literature as the *Rozvany-Prager mean squared slope condition*.

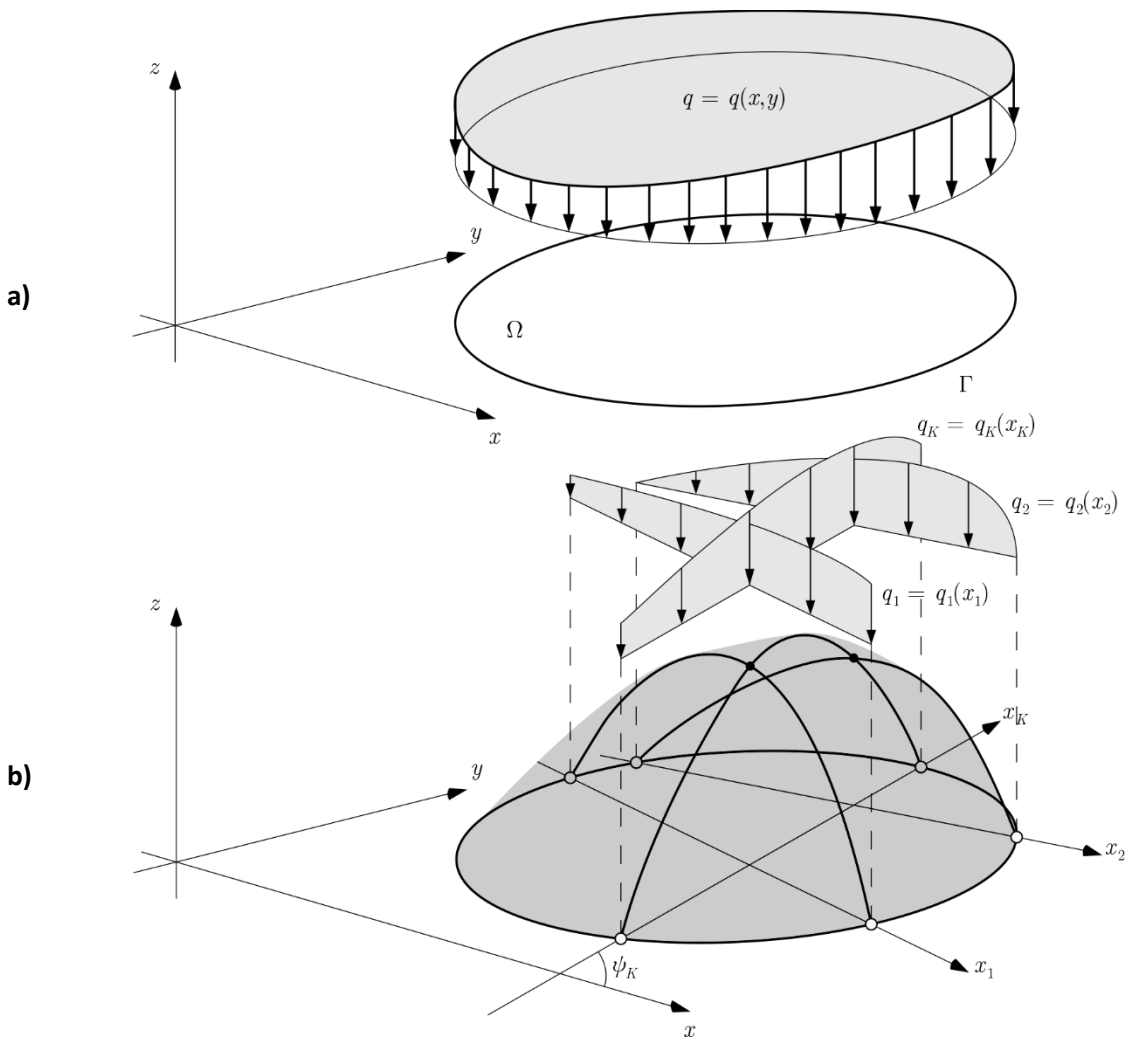


Figure 1. **a)** load $q = q(x, y)$ over domain Ω with boundary Γ ; **b)** archgrid elevation function $f = f(x, y)$ shown in transparent grey, single arch elevation functions are shown as thick black lines, q_K represents arch load acting on the K -th arch.

In the finite-dimensional context, we choose a mesh of n nodes in Ω at which the elevation of surface f is sampled, and we write $\mathbf{f} \in \mathbb{R}^n$ for the vector of elevations and $\mathbf{q} \in \mathbb{R}^n$ for the load vector. Slope functions s_K are replaced by vectors $\mathbf{s}_K = \mathbf{B}_K \mathbf{f}$, with matrices \mathbf{B}_K ($K = 1, \dots, k$) taking the place of the gradient and

projection operations in *ii)* above. This allows for categorizing the Rozvany-Prager minimum volume problem in terms of Second-Order Cone Programming, see [4],

$$\begin{array}{l}
 \text{(P)} \quad \left. \begin{array}{l} \text{where:} \\ \mathcal{F} = \left\{ \mathbf{f} \mid \begin{array}{l} \mathbf{f} \in \mathbb{R}^n \text{ and } f_N = 0 \text{ if } N\text{-th node is placed at } \Gamma ; \\ (\sqrt{L_K}, \mathbf{B}_K \mathbf{f}) \in \mathcal{C} . \end{array} \right\} \end{array} \right\} \\
 V_{min} = \frac{2}{\sigma_C} \max \{ \mathbf{q}^T \mathbf{f} \mid \mathbf{f} \in \mathcal{F} \},
 \end{array}$$

Here, \mathcal{C} stands for the second-order (quadratic) cone, i.e.

$$\mathcal{C} = \{ (a, \mathbf{b}) \mid a \geq \|\mathbf{b}\|_2 \}, \tag{2}$$

where a is a positive scalar and $\|\mathbf{b}\|_2$ now stands for the Euclidean norm of vector \mathbf{b} . Optimization problem dual to (P) is typically introduced by the use of Lagrange multiplier technique, see [1]. Determining the values of dual variables is standard in MOSEK; we do not elaborate on this topic here for the reason of space. Let us only mention that having the dual variables, say $(\mathbf{T}_1, \dots, \mathbf{T}_k)$, one may calculate the vectors $(\mathbf{A}_1, \dots, \mathbf{A}_k)$ comprising the values of a step-function representing the varying cross-section area of each arch.

3. Example

In the example, we consider the $\Omega = [0,2L] \times [0,2L]$ and the load case $q = \text{const.}$ acting above entire Ω , see Fig. 2. Results obtained with help of the SOCP approach are compared with the conclusions from the study in [3], where the minimum volume problem was solved in the continuous setting; see Tab. 1 for the collected results. More precisely, the elevation function f has been approximated in terms of the Fourier (trigonometric) and Legendre (polynomial) series in the orthogonal coordinates. For this reason, the comparison of results is limited to the orthogonal layout of arches.

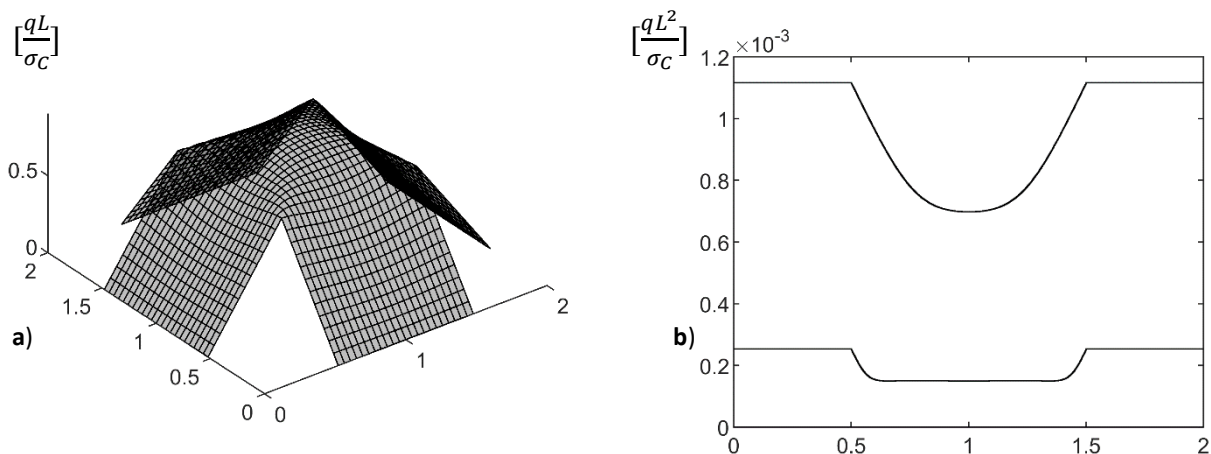


Figure 2. a) Optimal archgrid elevation function f ; b) optimal cross-section area functions for arches at $x = 0.6L$ (bottom line), and $x = L$ (top line).

Table 1. Square domain Ω with $q = \text{const.}$ above the entire domain. Comparison of results obtained for different numerical approaches.

number of arches along x and y	discrete approach with SOCP, [this note]		continuous approach with Fourier approximation, [3]		continuous approach with Legendre approximation, [3]	
	CPU time	optimal volume	CPU time	optimal volume	CPU time	optimal volume
45	0.5 sec.	$3.677 \frac{qL^3}{\sigma_0}$	131 sec.	$3.681 \frac{qL^3}{\sigma_0}$	167 sec.	$3.681 \frac{qL^3}{\sigma_0}$
100	1.7 sec.	$3.680 \frac{qL^3}{\sigma_0}$	4784 sec.	$3.681 \frac{qL^3}{\sigma_0}$	9063 sec.	$3.681 \frac{qL^3}{\sigma_0}$
1000	216 sec.	$3.681 \frac{qL^3}{\sigma_0}$	out of memory	-	out of memory	-

References

- [1] S. Boyd, L. Vandenberghe, *Convex optimization*, Cambridge, UK: Cambridge University Press, 2004.
- [2] R. Czubacki, T. Lewiński, (2020, Sep.) *Optimal archgrids: a variational setting*. Structural and Multidisciplinary Optimization, 62, 1371–1393. Available: <https://doi.org/10.1007/s00158-020-02562-y>
- [3] G. Dzierżanowski, R. Czubacki, (2021, Jan.) *Optimal archgrids spanning rectangular domains*. Computers and Structures, 242, article 106371, Available: <https://doi.org/10.1016/j.compstruc.2020.106371>
- [4] G. Dzierżanowski, K. Hetmański, (submitted). *Optimal design of archgrids: the second-order cone programming perspective*, Archives of Civil Engineering.
- [5] T. Lewiński, T. Sokół, C. Graczykowski, *Michell structures*, Cham, Switzerland: Springer Nature, 2019.
- [6] G.I.N. Rozvany, W. Prager, (1979, Jun.) *A new class of structural optimization problems: optimal archgrids*. Computer Methods in Applied Mechanics and Engineering, 19, 127-150. Available: [https://doi.org/10.1016/0045-7825\(79\)90038-0](https://doi.org/10.1016/0045-7825(79)90038-0)
- [7] G.I.N. Rozvany, C.-M. Wang, (1983, Jan.) *On plane Prager-structures – I*. International Journal of Mechanical Sciences, 25, 519-527. Available: [https://doi.org/10.1016/0020-7403\(83\)90044-9](https://doi.org/10.1016/0020-7403(83)90044-9)
- [8] G.I.N. Rozvany, C.-M. Wang, M. Dow, (1982, Jul.) *Prager-structures: archgrids and cable networks of optimal layout*. Computer Methods in Applied Mechanics and Engineering, 31, 91-113. Available: [https://doi.org/10.1016/0045-7825\(82\)90049-4](https://doi.org/10.1016/0045-7825(82)90049-4)
- [9] C.-M. Wang, G. I. N. Rozvany, (1983, Jan.) *On plane Prager-structures – II. Non-parallel loads and allowances for selfweight*. International Journal of Mechanical Sciences, 25, 529-541. Available: [https://doi.org/10.1016/0020-7403\(83\)90045-0](https://doi.org/10.1016/0020-7403(83)90045-0)

Session 6

**Applications of optimization
in various engineering areas**

Mitigation of urban substation magnetic field by active loop

D. Pelevin¹, K. Kundius², O. Sokol³, V. Grinchenko³

¹ State Institution "Institute of Technical Problems of Magnetism of the National Academy of Sciences of Ukraine",
pelevindmitro@ukr.net

² State Institution "Institute of Technical Problems of Magnetism of the National Academy of Sciences of Ukraine",
ekrinnadi@gmail.com

³ State Institution "Institute of Technical Problems of Magnetism of the National Academy of Sciences of Ukraine",
vsgrinchenko@gmail.com

1. Introduction

Urban transformer substations can be found in special rooms inside civil structures and residential buildings. These substations create a magnetic field in the surrounding space, as well in the living space. So some measures to mitigate the urban substation magnetic field in neighboring living space are to be taken. One of the ways is to use active shielding methods that provide the highest efficiency of magnetic field mitigation [1]. For this the active loops powered by a regulated current source are installed. The idea of the active shielding is to use these loops to create the magnetic field opposite to the urban substation magnetic field. The main problem related to the complex form of bus-bars in the substation. This leads to the inhomogeneity of the substation magnetic field. So the highest efficiency of the magnetic field mitigation is achieved only at some points, but not in all living space. To increase the shielding efficiency, it is proposed in [1] to aspire to the homogeneity of the mitigated magnetic field in the living space. This could be achieved by choosing optimal geometry of the active loop, its arrangement relative to the source of the magnetic field and the living space, and the current in the loop. The technique for optimization of active loops for magnetic field mitigation of urban substations is developed by the authors in [2]. In this paper, a numerical simulation is carried out using the MATLAB software package and the results of an experimental research conducted with a substation model are represented.

2. Computer simulation

Here we consider a substation with a rated power of 100 kVA and 10/0.4 kV transformer (Fig. 1a). The living room is located on top of the substation. To guarantee the magnetic field mitigation in the entire living room, it is enough to mitigate it within the control plane D distant from the floor room by 0.5 m [2]. Fig. 1b shows the distribution of the substation magnetic field when the current in low-voltage bus-bars is 100 A. The maximum value of RMS of the magnetic flux density in plane D is about $0.8 \div 0.9 \mu\text{T}$. We use the optimization technique from [2] to determine the parameters of the active loop. So the active loop having 5.2 ampere-turns is located 1.05 m away from the substation bus-bar. Fig. 1c shows the mitigated magnetic field distribution. The magnetic flux density is reduced to $0.1 \mu\text{T}$ and lower. And the shielding efficiency is 8 units and more.

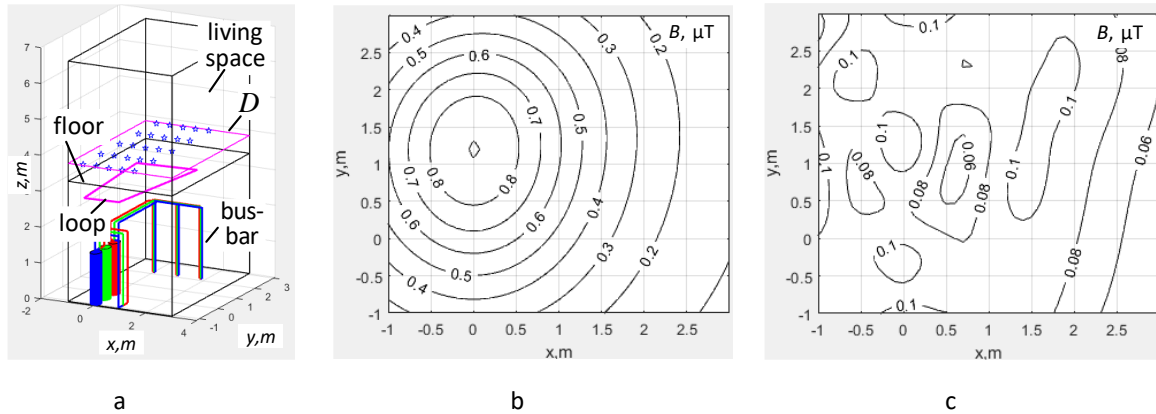


Figure 1. Computer simulation results

3. Experimental research

The substation model shown in Fig. 2a is made in a one-to-one scale. Fig. 2b shows the measured magnetic field of the substation in the plane D. Here the current in low-voltage bus-bars of the substation is 53 A. And the maximum value of RMS of the magnetic flux density is $0.64 \mu\text{T}$. We use the active loop having 10 turns. Its total resistance is 4 Ohm. The current in the active loop is 0.24 A. Energy consumption is less than 0.01 kW.

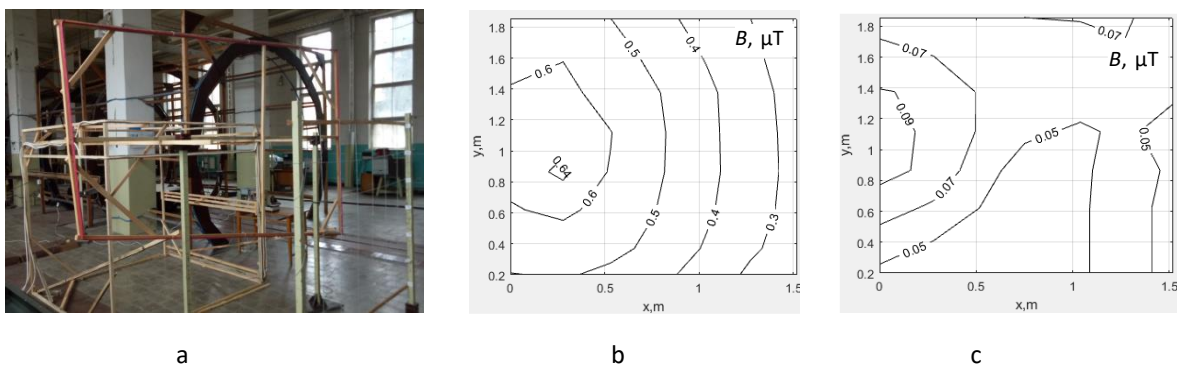


Figure 2. Results of experimental researches

Fig. 2c shows that the usage of the active loop mitigates the magnetic field to $0.09 \mu\text{T}$. The mitigated magnetic field is not uniform, but its fluctuations are comparably low. Wherein, the shielding efficiency is more than 7 units.

References

- [1] del Pino Lopez J.C., Giaccone L., Canova A., Cruz Romero P. (2014). *Ga-based active loop optimization for magnetic field mitigation of MV/LV substations*. IEEE Latin America Transactions, vol. 12, no. 6, pp. 1055-1061. doi: 10.1109/tla.2014.6894000.
- [2] Rozov V.Yu., Kundius K.D., Pelevin D.Ye. (2020). *Active shielding of external magnetic field of built-in transformer substations*. Electrical engineering & electromechanics, no.3, pp. 24-30. doi: 10.20998/2074-272X.2020.3.04.

Stability of Steady State Motion of Rod Protected From Vibration

M.U. Khodjabekov

Samarkand State Architectural and Civil Engineering Institute, 70 Lolazor str., 140147, Samarkand, Uzbekistan;
e-mail: uzedu@inbox.ru

1. Introduction

One of the urgent problems in modern equipment and technologies is the reducing of harmful vibrations in the elements of machines, mechanisms, devices and consequently, ensuring long-term efficient operation. In order to solve these problems, it is effective to use different types of dynamic absorbers.

In the work [1] studied the stability of stationary motion of a dynamic system with elastic dissipative characteristics of the hysteresis type on the basis of characteristic equations. In the work [2] considered the effect of a dynamic absorber on the unstable motion of an aircraft wing. The parameters of the Bouc-Wen model and the aerodynamic torque parameters were determined experimentally. The differential equations of motion of mechanical systems have been obtained using the averaging method in the work [3]. A methodology for finding stationary solutions was developed, and the stability of stationary motions was investigated using Lyapunov's first approximation method. Solutions to practical problems encountered in engineering have been obtained, numerically analyzed, and recommendations have been made. In the work [4] studied the dynamics and stability of nonlinear free and forced vibrations of discrete and continuous systems. The systems under consideration were mathematically modeled and analyzed using Lagrange equations. On the basis of the disturbed motion equations, the characteristic equations were determined, and the stable and unstable fields of motion were determined. The work [5] devoted to the problem of asymptotic and exponential stability of motions of autonomous and non-autonomous systems, and the equations of disturbed motion are defined. Stability of the motion of nonlinear systems was studied in relation to the change in system parameters based on the disturbed motion equations in [6]. The work [7] devoted the parametric stability of motion of mechanical systems. Lyapunov's exponent was investigated and stability conditions were studied on the basis of numerical analysis. The work [8] considered the problem of the stability of systems whose materials have elastic dissipative characteristics of the hysteresis type. Lyapunov's method was used to explore the stability of the motion. The reliability of the obtained results is shown and the practical problems are solved.

For discrete systems, liquid section dynamic absorbers as an object of vibration protection have been studied in the work [9].

2. Materials and Methods

The nonlinear vibrations of a distributed parametric elastic rod under the influence of kinematic excitations in conjunction with liquid section dynamic absorber is mathematically modeled using the bond graph methodology and obtained the expression of the transfer function to study the dynamics in the work [10].

Methodology for exploring the stability was developed in [11]. In this work we will analysis stability of steady state motion of the system. To make the matter understandable we write details as follows from [11]:

The differential equations of motion of the system protected from vibrations under consideration are expressed as follows [10]:

$$A_*\ddot{Q} + B\dot{Q} + CQ = F, \quad (1)$$

where

$$\ddot{Q} = \begin{bmatrix} \ddot{q}_i \\ \ddot{q}_3 \\ \ddot{q}_4 \end{bmatrix}; \dot{Q} = \begin{bmatrix} \dot{q}_i \\ \dot{q}_3 \\ \dot{q}_4 \end{bmatrix}; Q = \begin{bmatrix} q_i \\ q_3 \\ q_4 \end{bmatrix}; A_* = \begin{bmatrix} m_i & 0 & 0 \\ (m_{13} + m_{2*})u_m(x_1) & m_{13} + m_{2*} & m_{2*} + m_v \\ (m_{2*} - m_v)u_m(x_1) & m_{2*} - m_v & m_{2*} + m_{4*} \end{bmatrix};$$

$$B = \begin{bmatrix} 0 & -u_m(x_1)b_F & 0 \\ 0 & b_F & 0 \\ 0 & 0 & b_S \end{bmatrix}; C = \begin{bmatrix} c_i & -u_m(x_1)c_{1*} & 0 \\ 0 & c_{1*} & 0 \\ 0 & 0 & 2c_{2*} \end{bmatrix}; F = \begin{bmatrix} u_m(0)F_L + u_m(L)F_R \\ 0 \\ 0 \end{bmatrix};$$

m_{1*} and q_3 are mass and displacement of the outer body of the dynamic absorber surrounding the liquid, respectively; m_{2*} and q_4 are mass and displacement of solid of the dynamic absorber, respectively; m_{3*} is mass of liquid; m_{4*} is mass of liquid attached to the body with mass m_{2*} ; b_F is the coefficient of resistance of the damper; c_{1*} and c_{2*} are stiffness; $F_L(t)$ and $F_R(t)$ are external forces; m_i and q_i are i -accumulated modal masses and displacements of the rod, respectively; $m_{13} = m_1 + m_3$; m_v is the mass of liquid squeezed by the body with mass m_{2*} ; $u_m(0)$, $u_m(L)$ and $u_m(x_1)$ are the values of the vibration forms of the rod at the points $x = 0$, $x = L$ and at the point where the dynamic absorber is set $x = x_1$; b_S is the viscosity coefficient of the liquid; $c_i = c_{1i} + jc_{2i}$ [11];

$$c_{1i} = \left[\int_0^L \rho A (1 - C_0 \eta_1) u_m^2 dx - \frac{3EI}{\omega_{*m}^2} \eta_1 \sum_{i^*=1}^n C_{i^*} q_{ma}^{i^*} \frac{h^{i^*}}{2^{i^*} (i^* + 3)} \int_0^L u_m \frac{\partial^2}{\partial x^2} \left(\frac{\partial^2 u_m}{\partial x^2} \left| \frac{\partial^2 u_m}{\partial x^2} \right|^{i^*} \right) dx \right] \omega_{*m}^2;$$

$$c_{2i} = \left[\int_0^L \rho A C_0 \eta_2 u_m^2 dx + \frac{3EI}{\omega_{*m}^2} \eta_2 \sum_{i^*=1}^n C_{i^*} q_{ma}^{i^*} \frac{h^{i^*}}{2^{i^*} (i^* + 3)} \int_0^L u_m \frac{\partial^2}{\partial x^2} \left(\frac{\partial^2 u_m}{\partial x^2} \left| \frac{\partial^2 u_m}{\partial x^2} \right|^{i^*} \right) dx \right] \omega_{*m}^2;$$

q_{ma} are amplitudes of rod vibrations; $\eta_1, \eta_2 = \text{sign}(\omega) \eta_{22}$ are constant coefficients depending on the dissipative properties of the rod material, determined from the hysteresis loop; ω is frequency; $j^2 = -1$; C_0, C_1, \dots, C_n are coefficients determined experimentally of the hysteresis loop, depending on the damping properties of the rod material [11]; E, I are Young's modulus and moment of inertia of the rod, respectively; A, L are the cross-section area and length of the rod, respectively; ρ, ω_{*m} are the density of the rod material and natural frequencies, respectively.

The system of differential equations (1) has been reduced to a system of linear differential equations using the method of harmonic linearization. Therefore, we look for its solutions as follows:

$$q_i = q_{ma}(t) \cos(\omega t + \beta_i(t)); q_3 = q_{3*}(t) \cos(\omega t + \beta_{3*}(t)); q_4 = q_{4*}(t) \cos(\omega t + \beta_{4*}(t)), \quad (2)$$

where $q_{3*}(t) = q_{3*}, q_{4*}(t) = q_{4*}, \beta_{3*}(t) = \beta_{3*}, \beta_{4*}(t) = \beta_{4*}$ are amplitudes and initial phases of the variables q_3 and q_4 , respectively, and they are functions of slow variables; $\beta_i(t)$ are the initial phases of the slow variable functions of variables q_i .

According to the method of slow variable amplitudes, the amplitudes and initial phases of the solution system (2) satisfy the conditions imposed on the slow variable functions [12]. The first and second order derivatives of the solutions sought (2) are calculated taking into account the conditions for slowly varying functions, and put in the system of differential equations (1). The result is a system of first-order differential equations.

We can get an expression of the basic acceleration for kinematic excitations

$$W_0 = \varepsilon p_0 \cos \omega t, \quad (3)$$

where εp_0 is the amplitude of the base acceleration; ε is a small parameter.

3. Results and Discussion

Let the external forces F_L and F_R acting on the left and right ends of the rod through the base give the system acceleration W_0 .

In that case

$$F_L = F_R = m_i \varepsilon p_0 \cos \omega t. \quad (4)$$

We put the solutions (2), their derivatives, and the expression (3) into a system of differential equations of motion (1). As a result, in order to fulfill the equations formed after some simplifications, we get the following system of equations, provided that the coefficients in front of the corresponding trigonometric functions on both sides of these equations are equal:

$$\begin{aligned} \dot{q}_{ma} &= -(m_i \omega)^{-1} (-u_i(x_1) b_F q_{3*} \omega \cos \varphi_1 - u_i(x_1) c_{1*} q_{3*} \sin \varphi_1 + c_{2i} q_{ma} + m_i u_* \varepsilon p_0 \sin \beta_i); \\ \dot{\beta}_i &= -(m_i q_{ma} \omega)^{-1} (-u_i(x_1) b_F q_{3*} \omega \sin \varphi_1 + u_i(x_1) c_{1*} q_{3*} \cos \varphi_1 - c_{1i} q_{ma} + \omega^2 m_i q_{ma} \\ &\quad + m_i u_* \varepsilon p_0 \cos \beta_i); \\ \dot{q}_{3*} &= -(m_i \omega \Delta)^{-1} (-\Delta (-u_i^2(x_1) b_F q_{3*} \omega - u_i(x_1) q_{ma} (c_{1i} \sin \varphi_1 - c_{2i} \cos \varphi_1) + m_i u_i(x_1) u_* \varepsilon p_0 \sin \beta_3) - \\ &\quad M_2 q_{4*} m_i (\omega b_S \cos \varphi_2 + 2c_{2*} \sin \varphi_2) + M_4 q_{3*} m_i b_F \omega); \end{aligned} \quad (5)$$

$$\begin{aligned} \dot{\beta}_{3*} &= -(m_i \omega q_{3*} \Delta)^{-1} (\Delta (u_i(x_1) q_{ma} (c_{1i} \cos \varphi_1 + c_{2i} \sin \varphi_1) + (\omega^2 m_i + u_i^2(x_1) c_{1i}) q_{3*} \\ &\quad - m_i u_i(x_1) u_* \varepsilon p_0 \cos \beta_3) - M_2 q_{4*} m_i (\omega b_S \sin \varphi_2 - 2c_{2*} \cos \varphi_2) - M_4 q_{3*} m_i c_{1*}); \end{aligned}$$

$$\dot{q}_{4*} = (\omega \Delta)^{-1} (M_3 q_{3*} b_F \omega \cos \varphi_2 - M_3 q_{3*} c_{1*} \sin \varphi_2 - M_1 q_{4*} b_S \omega);$$

$$\dot{\beta}_{4*} = -(q_{4*} \omega \Delta)^{-1} (M_3 q_{3*} b_F \omega \sin \varphi_2 + M_3 q_{3*} c_{1*} \cos \varphi_2 + \Delta q_{4*} \omega^2 - 2M_1 q_{4*} c_{2*}),$$

where $u_* = u_i(0) + u_i(L)$; $\varphi_1 = \beta_{3*} - \beta_i$; $\varphi_2 = \beta_{4*} - \beta_{3*}$; $M_1 = m_{13} + m_{2*}$; $M_2 = m_{2*} + m_v$; $M_3 = m_{2*} - m_v$; $M_4 = m_{2*} + m_{4*}$; $\Delta = M_1 M_4 - M_2 M_3$.

The resulting system of equations (5) allows determining the sought stationary motion of the system under consideration. This is done on the basis of the values $\dot{q}_{ma} = 0$, $\dot{\beta}_i = 0$, $\dot{q}_{3*} = 0$, $\dot{\beta}_{3*} = 0$, $\dot{q}_{4*} = 0$, $\dot{\beta}_{4*} = 0$ can be determined from this system of differential equations (5) as follows:

$$q_{ma0} = |u_*| \varepsilon p_0 \sqrt{\frac{\Omega_1^2 + \Omega_2^2}{\Theta_1^2 + \Theta_2^2}}; q_{3*0} = |u_*| \varepsilon p_0 \sqrt{\frac{\Omega_3^2 + \Omega_4^2}{\Theta_1^2 + \Theta_2^2}}; q_{4*0} = |u_*| \varepsilon p_0 \sqrt{\frac{\Omega_5^2 + \Omega_6^2}{\Theta_1^2 + \Theta_2^2}}, \quad (6)$$

where $\Omega_1 = m_i (c_{1*} - M_1 \omega^2) (2c_{2*} - M_4 \omega^2) - m_i b_F b_S \omega^2 - m_i M_2 M_3 \omega^4$;

$\Omega_2 = ((c_{1*} - M_1 \omega^2) b_S + (2c_{2*} - M_4 \omega^2) b_F) m_i \omega$;

$\Omega_3 = 2c_{2*} M_1 m_i u_i(x_1) \omega^2 - \Delta m_i u_i(x_1) \omega^4$; $\Omega_4 = b_S M_1 m_i u_i(x_1) \omega^3$;

$\Omega_5 = c_{1*} M_3 m_i u_i(x_1) \omega^2$; $\Omega_6 = b_F M_3 m_i u_i(x_1) \omega^3$;

$\Theta_1 = -\Delta m_i \omega^6 + \left((2c_{2*} M_1 + c_{1*} M_4) m_i + (m_i + u_i^2(x_1) M_1) b_F b_S + \Delta (c_{1i} + c_{1*} u_i^2(x_1)) \right) \omega^4 +$
 $(b_S M_1 + b_F M_4) c_{2i} \omega^3 - (2c_{1*} c_{2*} (m_i + u_i^2(x_1) M_1) + (2c_{2*} M_1 + c_{1*} M_4 + b_F b_S) c_{1i}) \omega^2 - (b_S c_{1*} +$
 $2c_{2*} b_F) c_{2i} \omega + 2c_{1*} c_{2*} c_{1i}$;

$\Theta_2 = (\Delta b_F u_i^2(x_1) + (b_S M_1 + b_F M_4) m_i) \omega^5 + \Delta c_{2i} \omega^4 - \left((b_S M_1 + b_F M_4) c_{1i} + (m_i + u_i^2(x_1) M_1) (b_S c_{1*} +$
 $2c_{2*} b_F) \right) \omega^3 - (2c_{2*} M_1 + c_{1*} M_4 + b_F b_S) c_{2i} \omega^2 + (b_S c_{1*} + 2c_{2*} b_F) c_{1i} \omega + 2c_{1*} c_{2*} c_{2i}$.

In order to explore the stability of the obtained stationary motion, we get the solutions of the system of differential equations (5) close to the stationary state as follows:

$$q_{ma}(t) = q_{ma0} + \delta q_{ma}(t); \beta_i(t) = \beta_{i0} + \delta \beta_i(t); q_{3^*}(t) = q_{3^*0} + \delta q_{3^*}(t); \quad (7)$$

$\beta_{3^*}(t) = \beta_{3^*0} + \delta \beta_{3^*}(t); q_{4^*}(t) = q_{4^*0} + \delta q_{4^*}(t); \beta_{4^*}(t) = \beta_{4^*0} + \delta \beta_{4^*}(t);$
 where $\delta q_{ma}(t), \delta q_{3^*}(t), \delta q_{4^*}(t), \delta \beta_i(t), \delta \beta_{3^*}(t), \delta \beta_{4^*}(t)$ accept small values.

We put the solutions (7) in the system of differential equations (5) and extend the row the right sides of the resulting system of equations around the stationary solution relative to the variables $\delta q_{ma}(t), \delta q_{3^*}(t), \delta q_{4^*}(t), \delta \beta_i(t), \delta \beta_{3^*}(t), \delta \beta_{4^*}(t)$, and bounded by first-order terms since these variables are small. As a result

$$\begin{aligned} \varepsilon \delta \dot{q}_{ma} &= \varepsilon \left[f_1 + \frac{\partial f_1}{\partial q_{ma}} \delta q_{ma} + \frac{\partial f_1}{\partial \beta_i} \delta \beta_i + \frac{\partial f_1}{\partial q_{3^*}} \delta q_{3^*} + \frac{\partial f_1}{\partial \beta_{3^*}} \delta \beta_{3^*} \right]; \\ \varepsilon \delta \dot{\beta}_i &= \varepsilon \left[f_2 + \frac{\partial f_2}{\partial q_{ma}} \delta q_{ma} + \frac{\partial f_2}{\partial \beta_i} \delta \beta_i + \frac{\partial f_2}{\partial q_{3^*}} \delta q_{3^*} + \frac{\partial f_2}{\partial \beta_{3^*}} \delta \beta_{3^*} \right]; \\ \varepsilon \delta \dot{q}_{3^*} &= \varepsilon \left[f_3 + \frac{\partial f_3}{\partial q_{ma}} \delta q_{ma} + \frac{\partial f_3}{\partial \beta_i} \delta \beta_i + \frac{\partial f_3}{\partial q_{3^*}} \delta q_{3^*} + \frac{\partial f_3}{\partial \beta_{3^*}} \delta \beta_{3^*} + \frac{\partial f_3}{\partial q_{4^*}} \delta q_{4^*} + \frac{\partial f_3}{\partial \beta_{4^*}} \delta \beta_{4^*} \right]; \\ \varepsilon \delta \dot{\beta}_{3^*} &= \varepsilon \left[f_4 + \frac{\partial f_4}{\partial q_{ma}} \delta q_{ma} + \frac{\partial f_4}{\partial \beta_i} \delta \beta_i + \frac{\partial f_4}{\partial q_{3^*}} \delta q_{3^*} + \frac{\partial f_4}{\partial \beta_{3^*}} \delta \beta_{3^*} + \frac{\partial f_4}{\partial q_{4^*}} \delta q_{4^*} + \frac{\partial f_4}{\partial \beta_{4^*}} \delta \beta_{4^*} \right]; \\ \varepsilon \delta \dot{q}_{4^*} &= \varepsilon \left[f_5 + \frac{\partial f_5}{\partial q_{3^*}} \delta q_{3^*} + \frac{\partial f_5}{\partial \beta_{3^*}} \delta \beta_{3^*} + \frac{\partial f_5}{\partial q_{4^*}} \delta q_{4^*} + \frac{\partial f_5}{\partial \beta_{4^*}} \delta \beta_{4^*} \right]; \\ \varepsilon \delta \dot{\beta}_{4^*} &= \varepsilon \left[f_6 + \frac{\partial f_6}{\partial q_{3^*}} \delta q_{3^*} + \frac{\partial f_6}{\partial \beta_{3^*}} \delta \beta_{3^*} + \frac{\partial f_6}{\partial q_{4^*}} \delta q_{4^*} + \frac{\partial f_6}{\partial \beta_{4^*}} \delta \beta_{4^*} \right], \end{aligned} \quad (8)$$

where f_k are functions on the right side of the system of differential equations (5), respectively ($k = 1, \dots, 6$).

$$\begin{aligned} \frac{\partial f_1}{\partial q_{ma}} &= \alpha_1 (c_{2i} q_{ma})'_{q_{ma}}; \frac{\partial f_1}{\partial \beta_i} = \alpha_1 (c_{1i} - m_i \omega^2) q_{ma}; \frac{\partial f_1}{\partial q_{3^*}} = \alpha_1 (\omega b_F \cos \varphi_1 + c_{1^*} \sin \varphi_1) u_i(x_1); \\ \frac{\partial f_1}{\partial \beta_{3^*}} &= \alpha_1 (-\omega b_F \sin \varphi_1 + c_{1^*} \cos \varphi_1) u_i(x_1) q_{3^*}; \alpha_1 = -(m_i \omega)^{-1}; \frac{\partial f_2}{\partial q_{ma}} = \alpha_2 (m_i \omega^2 - (c_{1i} q_{ma})'_{q_{ma}}); \\ \frac{\partial f_2}{\partial \beta_i} &= \alpha_2 c_{2i} q_{ma}; \frac{\partial f_2}{\partial q_{3^*}} = \alpha_2 (\omega b_F \sin \varphi_1 - c_{1^*} \cos \varphi_1) u_i(x_1); \\ \frac{\partial f_2}{\partial \beta_{3^*}} &= \alpha_2 (\omega b_F \cos \varphi_1 + c_{1^*} \sin \varphi_1) u_i(x_1) q_{3^*}; \alpha_2 = -(m_i \omega q_{ma})^{-1}; \\ \frac{\partial f_3}{\partial q_{ma}} &= (m_i \omega \Delta)^{-1} \Delta u_i(x_1) ((c_{2i} q_{ma})'_{q_{ma}} \cos \varphi_1 - (c_{1i} q_{ma})'_{q_{ma}} \sin \varphi_1); \\ \frac{\partial f_3}{\partial \beta_i} &= \alpha_3 \Delta (c_{1i} \cos \varphi_1 + c_{2i} \sin \varphi_1) u_i(x_1) q_{ma}; \frac{\partial f_3}{\partial q_{3^*}} = \alpha_3 (\Delta u_i^2(x_1) + M_4 m_i) \omega b_F; \\ \frac{\partial f_3}{\partial \beta_{3^*}} &= \alpha_3 (\Delta (u_i^2(x_1) c_{1^*} + m_i \omega^2) - M_4 m_i c_{1^*}) q_{3^*}; \frac{\partial f_3}{\partial q_{4^*}} = \alpha_3 (b_S \omega \cos \varphi_2 + 2c_{2^*} \sin \varphi_2) m_i M_2; \\ \frac{\partial f_3}{\partial \beta_{4^*}} &= \alpha_3 (-b_S \omega \sin \varphi_2 + 2c_{2^*} \cos \varphi_2) m_i M_2 q_{4^*}; \alpha_3 = (m_i \omega \Delta)^{-1}; \\ \frac{\partial f_4}{\partial q_{ma}} &= \alpha_4 \Delta u_i(x_1) ((c_{1i} q_{ma})'_{q_{ma}} \cos \varphi_1 + (c_{2i} q_{ma})'_{q_{ma}} \sin \varphi_1); \\ \frac{\partial f_4}{\partial \beta_i} &= \alpha_4 \Delta u_i(x_1) q_{ma} (c_{1i} \sin \varphi_1 - c_{2i} \cos \varphi_1); \frac{\partial f_4}{\partial q_{3^*}} = \alpha_4 (\Delta (u_i^2(x_1) c_{1^*} + m_i \omega^2) - M_4 m_i c_{1^*}); \\ \frac{\partial f_4}{\partial \beta_{3^*}} &= \alpha_4 (M_4 m_i + \Delta u_i^2(x_1)) \omega b_F q_{3^*}; \frac{\partial f_4}{\partial q_{4^*}} = \alpha_4 (2c_{2^*} \cos \varphi_2 - b_S \omega \sin \varphi_2) m_i M_2; \\ \frac{\partial f_4}{\partial \beta_{4^*}} &= \alpha_4 (-b_S \omega \cos \varphi_2 - 2c_{2^*} \sin \varphi_2) m_i M_2 q_{4^*}; \alpha_4 = -(m_i \omega q_{3^*} \Delta)^{-1}; \end{aligned}$$

$$\begin{aligned}\frac{\partial f_5}{\partial q_{3*}} &= \alpha_5(b_F \omega \cos \varphi_2 - c_{1*} \sin \varphi_2)M_3; \frac{\partial f_5}{\partial \beta_{3*}} = \alpha_5(b_F \omega \sin \varphi_2 + c_{1*} \cos \varphi_2)q_{3*}M_3; \\ \frac{\partial f_5}{\partial q_{4*}} &= \alpha_5(-M_1 b_S \omega); \frac{\partial f_5}{\partial \beta_{4*}} = \alpha_5(\Delta \omega^2 - 2c_{2*}M_1)q_{4*}; \alpha_5 = (\omega \Delta)^{-1}; \frac{\partial f_6}{\partial q_{4*}} = \alpha_6(\Delta \omega^2 - 2c_{2*}M_1); \\ \frac{\partial f_6}{\partial q_{3*}} &= \alpha_6(b_F \omega \sin \varphi_2 + c_{1*} \cos \varphi_2)M_3; \frac{\partial f_6}{\partial \beta_{3*}} = \alpha_6(c_{1*} \sin \varphi_2 - b_F \omega \cos \varphi_2)q_{3*}M_3; \\ \frac{\partial f_6}{\partial \beta_{4*}} &= \alpha_6 M_1 b_S q_{4*} \omega; \alpha_6 = -(q_{4*} \omega \Delta)^{-1}.\end{aligned}$$

The first term on the right side of equation (9) assumes a value of zero, since the left side of equations (5) is equal to zero for the steady state.

Equations (8) represent the disturbed motions of hysteresis-type elastic dissipative characteristic rod with liquid section dynamic absorber.

Characteristic equation of system.

$$\lambda^6 + A_1 \lambda^5 + A_2 \lambda^4 + A_3 \lambda^3 + A_4 \lambda^2 + A_5 \lambda^1 + A_6 \lambda^0 = 0, \quad (9)$$

where A_k are coefficients investigated from (9).

It is known from the courses of the theory of stability [13,14] that it is sufficient for the real part of the roots of its characteristic equation to be negative for the action being stable. Based on the Routh criterion, it can be shown that the real part of the roots of the characteristic equation is negative. For this purpose, we construct the Routh scheme for the characteristic equation.

$$\begin{array}{ccccc} 1 & A_2 & A_4 & A_6 & 0 \\ A_1 & A_3 & A_5 & 0 & 0 \\ T_1 & T_2 & T_3 & 0 & 0 \\ D_1 & D_2 & 0 & 0 & 0 \\ R_{1*} & R_{2*} & 0 & 0 & 0 \\ P_1 & 0 & 0 & 0 & 0 \\ K_1 & 0 & 0 & 0 & 0 \end{array} \quad (10)$$

where $T_1 = A_1 A_2 - A_3$; $T_2 = A_1 A_4 - A_5$; $T_3 = A_1 A_6$; $D_1 = T_1 A_3 - A_1 T_2$; $D_2 = T_1 A_5 - A_1 T_3$; $R_{1*} = D_1 T_2 - D_2 T_1$; $R_{2*} = D_1 T_3$; $P_1 = R_{1*} D_2 - D_1 R_{2*}$; $K_1 = P_1 R_{2*}$.

The following system of inequalities can be formed from the Routh scheme:

$$A_1 A_2 - A_3 > 0, T_1 A_3 - A_1 T_2 > 0, D_1 T_2 - D_2 T_1 > 0, R_{1*} D_2 - D_1 R_{2*} > 0, P_1 R_{2*} > 0. \quad (11)$$

According to the first condition of the Routh criterion, all coefficients of the characteristic equation must be positive. The second condition of this criterion is the inequalities (11). If the above two conditions of the criterion are exists, the roots of the characteristic equation under consideration will be negative.

4. Conclusion

We obtained the characteristic equations for the combined stationary motions of hysteresis-type elastic dissipative characteristic rod with liquid section dynamic absorber from the disturbed motion equations. The problem of stability of motion in nonlinear cases is solved using the equations of the normal form of systems, the traditional methods of converting the differential equations of motion to the equations of the normal form require certain deviations and complex operations. To this end, it has been shown that the method of bond graph in solving problems allows to bypass this problem, that is, to create a system of equations of normal form, called the Cauchy form, directly relative to state variables. These characteristic

equations allow us to explore the stability of system that is protected from vibrations. It is possible to explore negativity the real parts of the roots of the characteristic equations formed using the Routh criterion, and the conditions obtained under the scheme of this criterion represent the stability conditions.

References

- [1] **D. Laxalde, F. Thouverez, J. Sinou.** *Dynamics of a linear oscillator connected to a small strongly nonlinear hysteretic absorber*, Journal of nonlinear mechanics. Volume 41, 2006, p.969-978.
- [2] **A. Malher, O. Doar'e, C. Touz'e.** *Influence of a hysteretic damper on the utter instability*. Journal of Fluids and Structures, Volume 68, 2017, p.356 - 369.
- [3] **A. Fidlin.** *Nonlinear Oscillations in mechanical engineering*. Springer press, The Netherlands, 2006, p.366.
- [4] **S.G. Kelly.** *Mechanical vibrations: Theory and applications*, Global Engineering press, USA, 2012, p.898.
- [5] **A.N. Michel, L. Hou, D. Liu.** *Stability of Dynamical Systems*. Birkhäuser Boston press, USA, 2008, p.515.
- [6] **M. Migdalovici, D. Baran.** *Theoretical research regarding any stability theorems with applications*, Proceedings of the 14th international congress on sound and vibration, July 9-12, 2007, Cairns, Australia, p.575-581.
- [7] **W.C. Xie.** *Moment Lyapunov exponents of a two-dimensional system under real-noise excitation*. Journal of Sound and Vibration, Vol. 239, 2001, p.139-155.
- [8] **H. Zhang, Zh. Wu, Y. Xi.** *Exponential stability of stochastic systems with hysteresis switching*, Journal of Automatica. Volume 50, 2014, p.599-606.
- [9] **O.M. Dusmatov.** *Dynamic damping of elastic systems with lumped and distributed parameters*. Dissertation Cand. phys.-mat. Sciences, Kiev Polytechnic. Ins. Kiev, 1988.
- [10] **M.M. Mirsaidov, O.M. Dusmatov, M.U. Khodjabekov.** *The problem of mathematical modeling of a vibration protected rod under kinematic excitations*, in Proceedings of VII International Scientific Conference Integration, Partnership and Innovation in Construction Science and Education, 11-14 November, 2020, Tashkent, Uzbekistan (2020), [doi:10.1088/1757-899X/1030/1/012069](https://doi.org/10.1088/1757-899X/1030/1/012069)
- [11] **G.S. Pisarenko, A.P. Yakovlev, V.V. Matveev.** *Vibration-damping properties of construction materials*. Reference book. - Kiev: Nauk. dumka, 1971, P. 327.
- [12] **S.P. Strelkov.** *Introduction to the theory of vibrations*. Publishing house Science. Moscow. 1964, P. 440.
- [13] **D.R. Merkin.** *Introduction to the theory of motion stability*. - M.: Nauka, - 1971. - p. 312.
- [14] **Ya.G. Panovko, I.I. Gubanova.** *Stability and vibrations of elastic systems*. - M.: Science. Ch. ed. phys.-mat. lit., 1987. - p. 352.

Charpy impact test to sedimentary rocks

B. A. Lógó¹, B. Vásárhelyi¹

¹ *Department of Engineering Geology and Geotechnics, Budapest University of Technology and Economics, Budapest, Hungary logobenedek@gmail.com*

ABSTRACT

In this work a relative simple experimental and theoretical procedure is presented in case of site work to determine the uniaxial strength and/or the tensile strength of a specific type of rock. Adapting the Charpy impact test for metals and/or polymers, a simplified method is presented to calculate the uniaxial strength and/or the tensile strength functions of the Permian red sandstone in function of the specific impact value, as example. For sake of simplicity a linear fitting and a polynomial approximation is suggested. The relative errors of the approximations were calculated.

KEYWORDS: Charpy hammer; impact test; rock; mechanical properties

1. Introduction

Hungary is very rich in sedimentary rocks, so this type of rock was also used as a building material in most of the buildings. Qualifying building materials, especially when it comes to natural materials is not easy, time consuming and labor intensive. A good solution for this would be the Charpy impact test, as it can be done easily and quickly. For many materials, such as metals and polymers, the standardized Charpy impact test has already been developed (e.g. for metals [1]). A further advantage of the test is that it can be performed with the test material in any condition in which it can be incorporated as a building material. From room temperature samples to frozen samples, samples with different water contents can be used to easily model the most diverse cases of everyday use. The only drawback is that the specimens must be of similar size, otherwise the results will not be comparable. This test method is addressed, inter alia, by Furuzumi et al [2,3], Borg [4], Komurlu [6], although in these articles somewhat differently and non-sedimentary rocks have been studied. In the improved version of the examination, it is already possible to monitor the formation and spread of cracks ([7,8,9,10])

2. Theoretical background

The study was originally developed by Georges Augustin Albert Charpy (1865-1945), a French scientist and university professor, for the study of metals at different temperatures [11]. Specific impact work is a measure used to characterize the toughness of structural materials, primarily metals. The harder a material is, the more energy it takes to tear or break it. The resulting measure is an empirical value, theoretically cannot be deduced from other strength properties of materials, it is suitable for ranking between individual materials.

In addition to material quality and technology, the specific impact work is also highly dependent on the test temperature and is suitable for testing the resistance of materials to brittle fracture.

High-impact materials are tough, small-impact materials are brittle. The behavior of the material can also be judged visually from the environment of the fracture: the brittle fracture is not preceded by a large plastic deformation and contraction, the surface of the fracture is fine-grained. When the tough material breaks, the material stretches and contracts significantly (in cross-section, its cross-section decreases), the surface of the fracture is rough, possibly the last torn part shows the fine grains of the brittle fracture. Most materials exhibit brittle and then tough behavior as the temperature increases. If impact tests are performed on a material under the same conditions only by changing the temperature, the results of the measurements may be plotted in a diagram similar to the figure. The temperature at the inflection point of the "S" -shaped curve is called the transition temperature.

Since this is not a familiar test in geology, it is important to know its theoretical background as well. When the specimen is struck (fractured), part of the kinetic energy of the pendulum is digested and the remaining part swings the pendulum further. Impact work is the impact energy used to impact (break) the test piece, which can be read on the scale of the equipment.

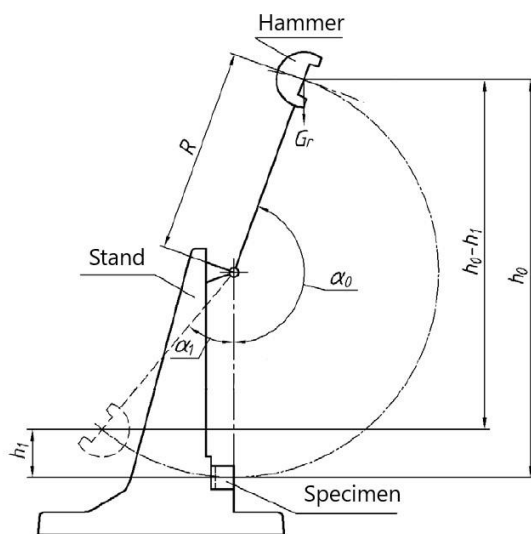


Figure 1. Theoretical arrangement of the Charpy hammer test and in the laboratory

As shown in Figure 1 above, a hammer of mass m fixed to the end of a rod of length R ($G = m \cdot g$) starts from a position of height h_0 . In this case, the gravitational (positional) potential energy:

$$E_0 = m \cdot g \cdot h_0 \quad (1)$$

After the impact, the hammer swings to a position of height h_1 , where it's gravitational (positional) potential energy:

$$E_1 = m \cdot g \cdot h_1 \quad (2)$$

The difference in gravitational (positional) potential energies gives the value of the energy expended to break the specimen, i.e. the value of the impact work (W).

$$W = E_0 - E_1 = m \cdot g \cdot (h_0 - h_1) \quad (3)$$

Height measurement is problematic during measurement; therefore the value of heights is determined using the starting (α_0) and overshoot angles (α_1).

$$W = m \cdot g \cdot R \cdot (\cos \alpha_0 - \cos \alpha_1) \quad (4)$$

Impact bending machines are already designed so that the value of the impact work can be read directly by means of a drag pointer, so that the value of the impact work can be easily calculated by substituting it into the formula.

During the experiments we used Permian red sandstone in the Balaton Uplands in Hungary. The results for each sample group are shown in Table 1. Each sample group contain at least 5 specimens. The aim of the experiment is to find a correlation between the specific impact work and the compressive strength results taken from the same sample groups. In this research two types of approximations are used to determine the mathematical connection between the specific impact work and the compressive (tensile) strength. The first approximation is based on a linear curve fitting, while the second one is a polynomial approximation (Lagrange interpolation). Briefly, the strength function approximation is presented here by of the use of this $C(0)$ continuous functions. Given a set of $n+1$ points in the X-Y plane (where x is the specific impact work, and y is the compressive or the tensile strength). Find the polynomial of degree n which passes through these points. The solution of the problem above can be obtained by the use of Lagrange interpolation polynomials,

$$P_n(x_i) = \sum_{i=1}^{n+1} y_i L_i(x); \quad (5)$$

where the i th Lagrange polynomial is

$$L_i(x) = \frac{(x - x_1)(x - x_2) \dots (x - x_{i-1})(x - x_{i+1}) \dots (x - x_{n+1})}{(x_i - x_1) \dots (x_i - x_{i-1})(x_i - x_{i+1}) \dots (x_i - x_{n+1})} \quad (6. a)$$

Introducing $\omega(x) = (x - x_1)(x - x_2) \dots (x - x_{n+1})$ the base polynomial can be calculated by

$$L_i(x) = \frac{\omega(x)}{(x - x_i)\omega'(x_i)}. \quad (6.b)$$

Here

$$L_i(x) = \begin{cases} 0; & \text{if } x = x_j; j = 1, 2, \dots, i - 1, i + 1, \dots, n + 1 \\ 1; & \text{if } x = x_i \end{cases} \quad (7)$$

In addition, a comparison is performed to find the relative error in these approximations (linear and polynomial) of the compressive (tensile) strength. This would greatly facilitate the development of an on-site inspection that is easy and quick to perform to get the unknown strength value if the specific impact work values (min. 3) are known.

3. New Red Sandstone

Two periods in the history of the earth have been characterized by globally extensive red sandstone formation. One is Devon (Old Red Sandstone) and the other is Perm (New Red Sandstone). In both cases, these formations formed in a semi-desert climate, in a riverine environment, and their material was the debris of a newly formed mountain system. In Devon it is the Caledonian mountain system, while in Perm it is the Variscian.

The red color is usually due to iron oxide coatings common in desert climates, but can also occasionally be associated with fermentation. Typically, most of the composition is quartz, but feldspar, mica, jasper, volcanic pieces may also appear. In Hungary, Devonian sandstones are not usually found, especially Permian sandstones.

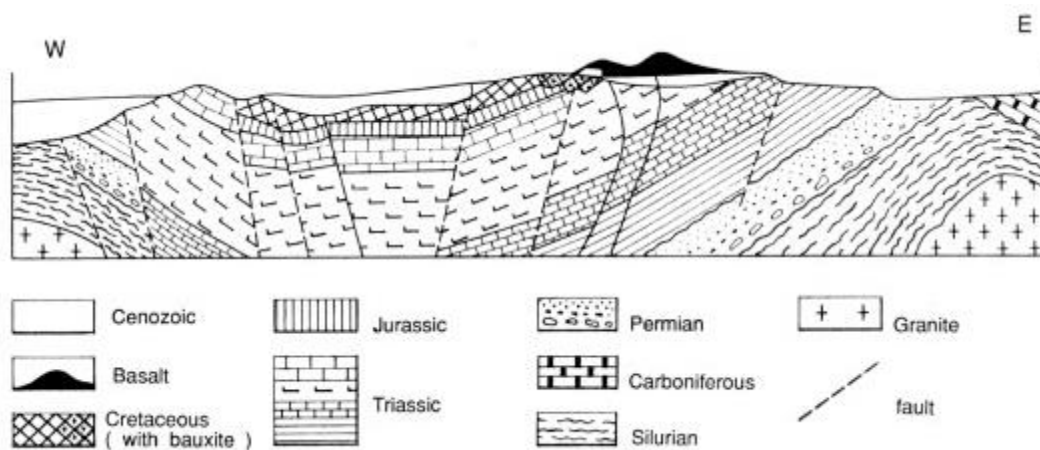


Figure 2. A conceptual geological section through the Bakony [12]

In the case of the ALCAPA microplate, the red sandstone (Balaton Uplands Sandstone formation) appears in the western part of its farthest sea from the contemporary sea, i.e. in the Balaton Uplands (figure 2).

4. Results

During the experimental program, Permian red stone was investigated. The individual samples were formed from the original block by drilling and cutting with the size and shape required for each test. The dimensions of the specimen were chosen so that they were large enough that the particles of different sizes did not affect the measurement results, but were small enough to be considered homogeneous. For sake of simplicity only three different groups of samples were formed (that is the minimum number of suggested samples). In each group the results of the impact energy test with the results of compressive strength (σ_c) and tensile strength (σ_t) were paired, respectively. By the use of these point pairs two functions (a linear and a polynomial) were calculated to determine the compressive (tensile) strength of the

investigated stone in function of the specific impact work. It is noted that more samples can lead more precise strength functions.

The experimental setup is shown in Figure 1 and a sample is shown in Figures 3 and 4 before and after the test. The results obtained (Figures 5-6) are shown in diagrams.

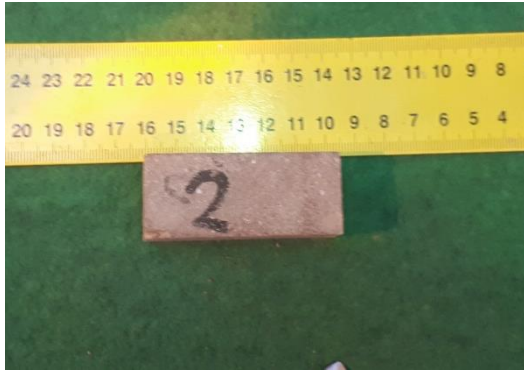


Figure 3. The „Nr.02” sample before the test



Figure 4. The „Nr.02” sample after the test

Table 1. Properties of the samples groups

Specimen group Nr	Density	Ultrasound velocity	UCS	Tensile strength (TS)	Specific impact work
	g/cm ³	km/s	MPa	MPa	J/mm ²
1	2.58	3.83	23.10	2.14	0.013
2	2.20	3.83	28.68	2.45	0.015
3	2.60	3.90	38.61	2.86	0.018

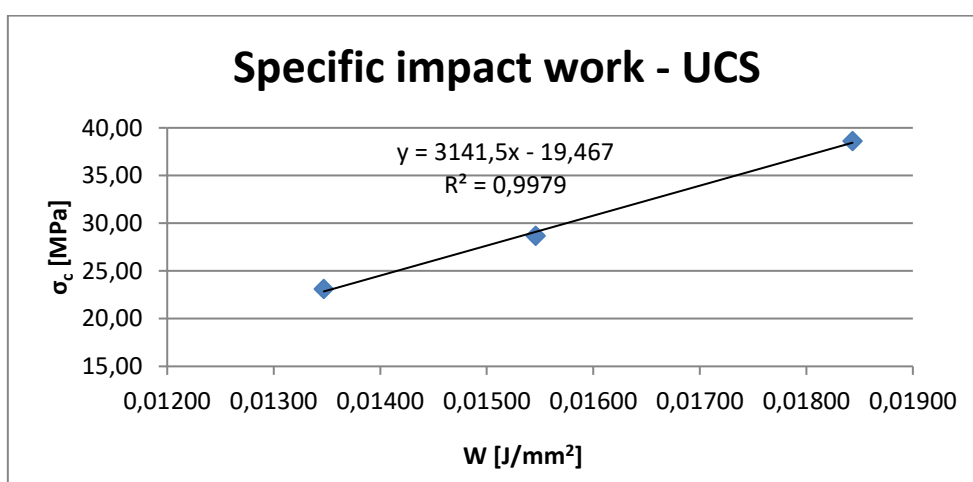


Figure 5. The connection between impact work and UCS (σ_c)

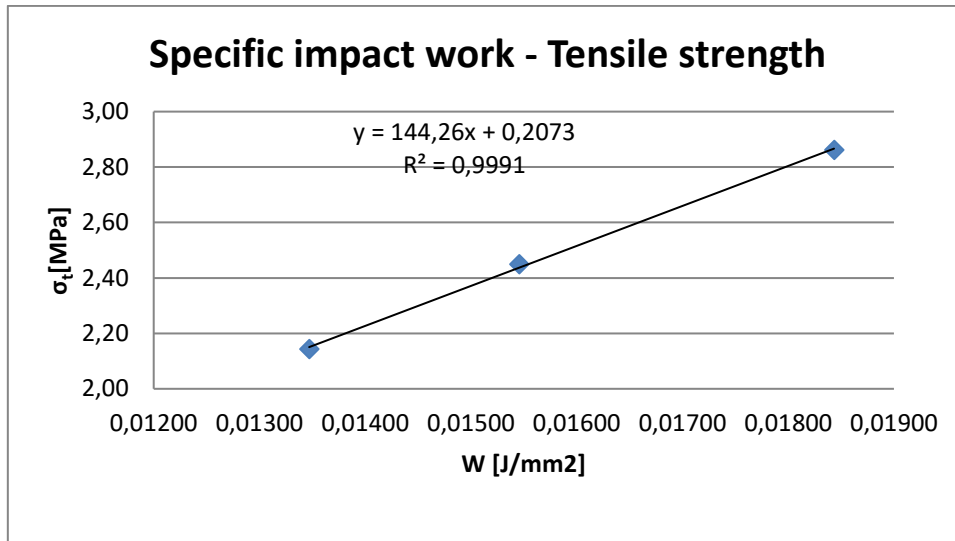


Figure 6. The connection between impact work and tensile strength (σ_t)

The linear approximation is performed by the use of Microsoft EXCEL program. The sample point pair lead for

$$\sigma_c(W) = 3141.5 \cdot W - 19.467 \cdot [MPa] \quad (8)$$

$$\sigma_t(W) = 144.26 \cdot W + 0.2073 \cdot [MPa] \quad (9)$$

Neglecting the details the base polynomials are in case of polynomial approximation $-C^{(0)}$ continuous-:

$$L_1 = \frac{W^2 - 0.0339 \cdot W + 0.000285}{9.87 \cdot 10^{-6}} \quad (10.a)$$

$$L_2 = \frac{W^2 - 0.0319 \cdot W + 0.000248}{-5.92 \cdot 10^{-6}} \quad (10.b)$$

$$L_3 = \frac{W^2 - 0.0289 \cdot W + 0.000208}{1.48 \cdot 10^{-5}} \quad (10.c)$$

$$\begin{aligned} \sigma_c(W) &= 23.1 \cdot L_1(W) + 28.68 \cdot L_2(W) + 38.61 \cdot L_3(W) = \\ &= 106986.52 \cdot W^2 - 288.07 \cdot W + 7.589 \end{aligned} \quad (11)$$

$$\begin{aligned} \sigma_t(W) &= 2.14 \cdot L_1(W) + 2.45 \cdot L_2(W) + 2.86 \cdot L_3(W) = \\ &= -3651.12 \cdot W^2 + 261.56 \cdot W - 0.7189 \end{aligned} \quad (12)$$

By the use of these functions one can determine the strength (compressive or tensile) values by the use of the specific impact values.

As an example let check the relative error if $W=0.017 \text{ J/mm}^2$ is given. By the use of linear fitting the compressive (eq.8) strength is $\sigma_c(0.017)=33.94 \text{ MPa}$, while the tensile (eq.9) strength is $\sigma_t(0.017)=2.66 \text{ MPa}$.

By the use of Lagrange approximation these values are:

$$\sigma_{cL}(0.017)=33.59 \text{ MPa and } \sigma_{tL}(0.017)=2.67 \text{ MPa.}$$

The relative errors are:

$$\text{uniaxial compressive strength } \Delta\%=(33.94-33.59)/(2*33.59)*100\%=0.52\%$$

$$\text{the tensile strength } \Delta\%=(2.67-2.66)/(2*2.66)*100\%=0.19\%$$

As a conclusion one can state that the relative error is small in these particular examples.

5. Conclusion

As shown in the diagrams, the Charpy hammer impact energy test can be used not only for steels but also for rocks. By the use of linear fitting or Lagrange type polynomials, the strength functions for uniaxial compressive strength and tensile strength can be determined. These functions provide a possibility to determine the unknown strength values for specific stones if the impact values are known. Comparing the results of each group of samples, the relationship between the impact energy analysis of samples with the same temperature and saturation state and their compressive and tensile strength can be seen. To determine the relationship more precisely, it is necessary to continue the research, both quantitatively with more samples and with samples with different temperatures and saturation states. In addition the model uncertainties and other probabilistic quantities (e.g. distributions of the measured values) can be considered during determination of the strength function functions.

6. Acknowledgements

This study was supported by the Unkp 2021, the TKP2020 Institution Excellence Subprogram, Grant No. TKP2020 BME-IKA-VÍZ of the National Research Development and Innovation Office of Hungary and the joint grant of the Hungarian Academy of Sciences and the Polish Academy of Sciences.

References

- [1] MSZ EN ISO 148-1:2017 *Metallic materials. Charpy pendulum impact test. Part 1: Test method*
- [2] Furuzumi, M.; Sugimoto, F.; Imai, T.; Kamoshida, N. and Abe, M. 2006. *The Charpy Impact Test of Rock (1st Report)-Dynamic Fracture Energy. J. Soc. Mat. Engng. for Resources of Japan. 18: 10-14.*
- [3] Furuzumi, M.; Sugimoto, F.; Imai, T.; Kamoshida, N. and Abe, M. 2006. *The Charpy Impact Test of Rock (2nd Report)-Dynamic Fracture Toughness. J. Soc. Mat. Engng. for Resources of Japan. 18: 15-20.*
- [4] Borg, E. 2018, *New Impact test method for rock drill inserts*, Uppsala ISSN: 1401-5773, UPTEC Q18 020

- [5] **Komurlu, E.** 2019, *An Experimental Study on Determination of Crack Propagation Energy of Rock Materials under Dynamic (Impact) and Static Loading Conditions* Hittite Journal of Science and Engineering, **6**(1): 01-06
- [6] **Zhang, Q.B. and Zhao, J.** 2014, *A Review of Dynamic Experimental Techniques and Mechanical Behaviour of Rock Materials*. Rock Mech. Rock Engng. **47**: 1411-1478
- [7] **Kharchenko, V.V., Kondryakov, E.A., Zhmaka, V.N., Babutskii, A.A. and Babutskii, A.I.** 2006, *The effect of temperature and loading rate on the crack initiation and propagation energy in carbon steel charpy specimens*. Strength of Materials **38**: 535-541.
- [8] **Zou, C. and Wong, L.N.Y.** 2014, *Experimental studies on cracking processes and failure in marble under dynamic loading*. Engng Geology **173**: 19-31.
- [9] **Komurlu, E.; Kesimal, A. and Demir, S.** 2016, *Determination of Indirect (Splitting) Tensile Strength of Cemented Paste Backfill Materials*. Geomechanics and Engineering **10**: 775-791.
- [10] **Durif, E., Réthoré, J., Combescure, A., Fregonese, M. and Chaudet, P.** 2012, *Controlling Stress Intensity Factors During a Fatigue Crack Propagation Using Digital Image Correlation and a Load Shedding Procedure*. Experimental Mechanics **52**: 1021–1031.
- [11] **Charpy, Augustin Georges Albert.** *Complete Dictionary of Scientific Biography*. Retrieved January 14, 2021 from Encyclopedia.com: <https://www.encyclopedia.com/science/dictionaries-thesauruses-pictures-and-press-releases/charpy-augustin-georges-albert>
- [12] **Juhász, Á.** 1987, *Memories of millions of years* (in Hungarian) publisher: Gondolat, Budapest

List of participants

Akhter Mohammed Javeed	<i>IPPT PAN, Poland</i>
Bocheński Marcin	<i>Lublin University of Technology, Poland</i>
Borkowski Adam	<i>IPPT PAN, Poland</i>
Broukous Pantelis	<i>BATI Energie sarl, Luxembourg / Imperial College London, UK</i>
Bruggi Matteo	<i>Politecnico di Milano, Italy</i>
Burczyński Tadeusz	<i>IPPT PAN, Poland</i>
Czubacki Radosław	<i>Warsaw University of Technology, Poland</i>
Dornak Wojtech	<i>VŠB-Technical University of Ostrava, Czech Republic</i>
Dubey Ved Prakash	<i>IPPT PAN, Poland</i>
Dzierżanowski Grzegorz	<i>Warsaw University of Technology, Poland</i>
Garstecki Andrzej	<i>Poznan University of Technology, Poland</i>
Ismail Hussein	<i>Budapest University of Technology and Economics, Hungary / Politecnico di Milano, Italy</i>
Jankowski Łukasz	<i>IPPT PAN, Poland</i>
Jarzębowska Elżbieta	<i>Warsaw University of Technology, Poland</i>
Jedlińska Aleksandra	<i>IPPT PAN, Poland</i>
John Antoni	<i>Silesian University of Technology, Poland</i>
Kaczmarczyk Jarosław	<i>Silesian University of Technology, Poland</i>
Khodjabekov Muradjon	<i>Samarkand State Architectural and Civil Engineering Institute, Uzbekistan</i>
Konečný Petr	<i>VŠB-Technical University of Ostrava, Czech Republic</i>
Kowalczyk Piotr	<i>IPPT PAN, Poland</i>
Lewiński Tomasz	<i>Warsaw University of Technology, Poland</i>
Logo Janos	<i>Budapest University of Technology and Economics, Hungary</i>
Manecka-Padaż Aleksandra	<i>IPPT PAN, Poland</i>
Miszczak Jarosław	<i>Institute of Theoretical and Applied Informatics PAS, Poland</i>
Moravcik Martin	<i>University of Zilina, Slovakia</i>
Mrozek Agata	<i>Poznań University of Technology, Poland</i>

Myśliński Andrzej	<i>Systems Research Institute, Warsaw, Poland</i>
Nowak Michał	<i>Poznan University of Technology, Poland</i>
Opiela Kamil	<i>IPPT PAN, Poland</i>
Ostrowski Mariusz	<i>IPPT PAN, Poland</i>
Pelevin Dmytro	<i>State Institution "Institute of Technical Problems of Magnetism of the National Academy of Sciences of Ukraine", Ukraine</i>
Platek Paweł	<i>Military University of Technology, Poland</i>
Popławski Błażej	<i>IPPT PAN, Poland</i>
Pospíšil Lukáš	<i>VŠB Technical University of Ostrava, Czech Republic</i>
Rad Majid Movahedi	<i>Széchenyi István University, Hungary</i>
Słoński Marek	<i>Cracow University of Technology, Poland</i>
Sokół Tomasz	<i>Warsaw University of Technology, Poland</i>
Świercz Andrzej	<i>IPPT PAN, Poland</i>
Tajs-Zielińska Katarzyna	<i>Cracow University of Technology, Poland</i>
Tello Lizeth	<i>Universidad del Valle, Mexico</i>
Vern Sourabh	<i>MNIT, Jaipur, India</i>
Wilk Dariusz	<i>Arte, Poland</i>
Yang Jia-Hua	<i>Guangxi University, China</i>
Zawidzka Ela	<i>IPPT PAN, Poland</i>
Zhao Dawei	<i>South Ural State University, Russia</i>



Professor Matteo Bruggi during his on-line presentation.



Participants in front of the IPPT PAN



Institute of Fundamental Technological Research
Polish Academy of Sciences
02-106 Warsaw, Poland
<http://www.ippt.pan.pl>